

#### **Copyright Undertaking**

This thesis is protected by copyright, with all rights reserved.

#### By reading and using the thesis, the reader understands and agrees to the following terms:

- 1. The reader will abide by the rules and legal ordinances governing copyright regarding the use of the thesis.
- 2. The reader will use the thesis for the purpose of research or private study only and not for distribution or further reproduction or any other purpose.
- 3. The reader agrees to indemnify and hold the University harmless from and against any loss, damage, cost, liability or expenses arising from copyright infringement or unauthorized usage.

#### **IMPORTANT**

If you have reasons to believe that any materials in this thesis are deemed not suitable to be distributed in this form, or a copyright owner having difficulty with the material being included in our database, please contact <a href="mailto:lbsys@polyu.edu.hk">lbsys@polyu.edu.hk</a> providing details. The Library will look into your claim and consider taking remedial action upon receipt of the written requests.

# FISH SWIMMING BEHIND MULTIPLE CYLINDERS

# YUEN TSZ WAI

# **MPhil**

**The Hong Kong Polytechnic University** 

2025

The Hong Kong Polytechnic University

Department of Mechanical Engineering

Fish Swimming behind Multiple Cylinders

# Yuen Tsz Wai

A thesis submitted in partial fulfilment of the requirements for the degree of Master of Philosophy

December 2024

# **CERTIFICATE OF ORIGINALITY**

I hereby declare that this thesis is my own work and that, to the best of my knowledge and belief
it reproduces no material previously published or written, nor material that has been accepted for
the award of any other degree or diploma, except where due acknowledgement has been made in
the text.
(Signed)
YUEN Tsz Wai (Name of student)

#### **Abstract**

Fish migration is a practice performed by many species of fish on a regular basis. It has been long observed that fish swim behind natural or man-made structures to exploit generated vortices to minimize locomotory costs. This phenomenon has attracted attentions from researchers and enlightened many studies. Although experiments qualitatively demonstrated the ability of fish to extract energy from environmental vortices, it is challenging to obtain quantitative results. With the fast development of computational hardware and algorithms in the last two decades, numerical simulations were widely employed to investigate fish swimming. However, in most cases, the fish models were either oversimplified, represented only by a filament or lack of self-propulsion ability. Moreover, few research has considered different structure arrangements.

To bridge these research gaps, we conduct a series of simulations to improve our physical understanding in fish swimming behind various structures. A fish-like model is developed based on an airfoil, being able to swim with a more realistic kinematics. This fish model can do self-propulsion with free swimming in both streamwise and crossflow directions. The underlying fluid-structure interactions are studied with an in-house numerical framework based on the immersed boundary lattice Boltzmann method (IB-LBM). With this framework, a fish model swimming with different motion modes behind single or multiple cylinders are examined. Four motion modes are applied, i.e. swimming without translation and rotation, swimming with only rotation, swimming with only translation and free swimming. For each motion mode, a parametric study is conducted.

For the study on the fish model undulating without translational and rotational motions behind a single cylinder, it is revealed that increasing free-stream velocity or cylinder diameter could reduce drag imposed on the fish body, depending on the cylinder-fish distance. Shortening streamwise and crossflow distances between the fish and the cylinder is found to be beneficial in drag reduction of the fish. Detailed flow structures and frequency spectra are analysed to reveal the underlying physics. This study is followed by the investigation on the fish model undulating with only rotations. It is found that rotation angle is a key contributing factor to the drag experienced by the fish model. Moreover, the fish model is overturned as the result of excessive rotation about its centroid when placed in the shed shear layer.

A parametric study is then carried out for the fish model translating only in the streamwise direction. It reveals that the fish only swims towards the cylinder with oscillatory rotations for any initial streamwise distance equal to or shorter than 3.4 times of the fish model's length. For longer distances, the fish is drifted away as the strong shed vortices cause the fish to overturn. It is also observed that the fish only swims towards the cylinder when it is near the cylinder's centreline such that it is not affected by the shear layers shed from the cylinder. For the study on free swimming, a unique scenario is observed. That is, apart from simply swimming towards or away from the cylinder, the fish initially swims towards the cylinder but is then driven away by the cylinder's wake.

Fish swimming behind two cylinders in two different arrangements is also investigated. The drifting-down and drifting-up modes are observed. A distribution of these two modes with two transition regions is presented. On the contrary, the drifting-up-then-down mode is revealed in free swimming behind two side-by-side cylinders. However, no obvious distribution motion-mode patterns are observed for different combinations of streamwise cylinder-fish distance and cylinder-cylinder crossflow distance.

The findings from this research have improved our understanding of fish swimming behind stationary objects. They contribute to bridging the research gaps of oversimplified fish model, lacking of self-propulsion ability. The results provide some useful insights into biomimetic applications such that more energy efficient underwater vehicles and robots for navigation and exploration of aquatic environment could be developed.

# Acknowledgement

Looking back at the past five years, COVID-19 pandemic presented many challenges to everyone and I am not an exception. During that period, I was on no-pay leave for my full-time job and became a "full-time student" which I never thought of. When all the restriction was removed by the government in early 2023, I was called back to resume my job duties and working non-stop since then. The journey of my MPhil study is full of challenge. Nevertheless, I am glad to have selfless support from different people whom I would like to express my gratitude.

First, I would like to express my heartfelt gratitude to my supervisor, Dr. Tang Hui for his valuable guidance, endless patience and continuous encouragement throughout my entire study. His expertise in fluid mechanics helped me identify problems in the critical way and guided me through the process of solving problems systematically. Besides, Dr. Tang encouraged us to develop our presentation and interpersonal skills as they are useful skills in our future career.

Second, I would like to express my sincere gratitude to Dr. Wang Chenglei for his patience and assistance regarding the numerical solver. His passion and determination in academic research influenced and motivated me a lot.

I would also like to take this opportunity to thank Dr. Wang Zhaokun, Dr. Zhao Fu Wang, Dr. Zeng Lingwei, Dr. Ai Chunhui, Dr. Jiang Qian, Deng Feng, Yeung Wai kin, Yu Antong and Billy Yan for their support and encouragement.

Last but not least, I must express my heartfelt thankfulness to my fiancée, Elaine Chow, my parents and my brother. They backed me up throughout my entire study. Without them, I probably could not finish my study.

# **Table of Contents**

Abstra	act		I	
Ackno	wled	gement	III	
Table	of Co	ontents	IV	
List of	f Figu	ıres	VI	
List of	f Tabl	les	XV	
Nome	nclatı	ure	XVI	
Chapt	er 1	Introduction	1	
1.1.	Ba	ckground	1	
1.2.	Lit	erature Review	3	
1.3.	Re	search Aim and Objectives		
1.4.	Org	ganization of Thesis	14	
Chapt	er 2	Problem Description and Methodology	15	
2.1.	Pro	oblem Description		
2.	1.1.	Physical Model and Kinematics		
2.	1.2.	Governing Equations	16	
2.	1.3.	Parameters	17	
2.2. Nu		merical Method	21	
2.2.1.		Lattice Boltzmann Method	22	
2.2.2.		Immersed Boundary Method	24	
2.2.3.		Computation Domain	25	
2.2.4.		Boundary Conditions	25	
2.2.5.		Numerical Validation	26	
2.2.6.		Grid and Time Step Convergence Tests	27	
2.3. Remarks		29		
Chapt	er 3	Undulation of fixed body behind Single Cylinder	30	
3.1.	Eff	Fect of Free-Stream Velocity	31	
3.2.	Eff	Fect of Streamwise Distance	43	
3.3.	Eff	Fect of Crossflow Distance	46	
3.4.	3.4. Effect of Upstream Cylinder Diameter			

3.5.	Remarks	54			
Chapte	er 4 Undulation of Rotation only body behind Single Cylinde	er55			
4.1.	Effect of Streamwise Distance				
4.2.	Effect of Crossflow Distance				
4.3.	Remarks				
Chapte	er 5 Self-Propelled Swimming behind Single Cylinder	84			
5.1.	Swimming in Streamwise Direction.	84			
5.1	1.1. Effect of Initial Streamwise Distance	85			
5.1	1.2. Effect of Initial Crossflow Distance	88			
5.2.	Free Swimming	91			
5.3.	Remarks	96			
Chapte	er 6 Swimming behind Two Cylinders	97			
6.1.	Swimming behind Two Tandem Cylinders	97			
6.2.	2. Swimming behind Two Side-by-Side Cylinders				
6.3.	Remarks	112			
Chapte	er 7 Conclusions and Future Work	113			
7.1.	Conclusions	113			
7.2.	Future Work				
Roforo	oneas	118			

# **List of Figures**

Figure	1-1	A	rockfish	swims	and	refuges	behind	rocks.	(adapted	from
https://w	ww.sc	ubadi	ving.com/u	nexpected	l-frienc	lship-verm	illion-rock	xfish)		2
Figure 1	-2 Suc	cessiv	e position o	of an eel s	swimmi	ing in wate	er at interv	al of 0.09	s. The side o	of each
square in	n the g	rid is	25.4 mm. [2	23]			•••••			4
Figure 1	-3 Fisl	h swir	nming mod	les classit	fied und	der (a) BC	F propulsi	on and (b	) MPF propi	ulsion.
[28]							•••••			5
Figure 1	-4 Rel	ation 1	between pro	opulsion r	nodes a	and swimm	ing motio	ns. [30]		5
Figure 1	-5 Cha	ange o	f body shap	e of the a	nguillií	form mode	l from tim	e t to t +	1.00. [35]	6
Figure 1	-6 Tiı	ne his	story of the	e body m	oveme	nt superin	posed on	the vorti	city contour	s with
velocity	fields	to sho	ow the intera	action of	trout wi	ith vortices	s from the	cylinder.	[49]	8
Figure 1	-7 (a)	Diag	ram of the	three-din	nension	al anguilli	form mod	el and (b)	) time variat	ion of
longitud	inal ve	elocity	$U_{\parallel}$ and late	eral veloc	eity $U_{\perp}$	in twelve	cycles as	the self-p	propelled swi	immer
accelera	tes fro	m rest	. Solid lines	s represen	it $U_{\parallel}$ and	d broken li	nes repres	ent $U_{\perp}$ wh	nile 2D cases	are in
cyan and	1 3D ca	ases a	re in black.	[55]						9
Figure 2	-1 Illu	stratic	on of the fish	h model						16
Figure 2	-2 Am	plitud	e envelope	profile of	the fis	h				16
Figure 2	-3(a) S	Schem	atic of the f	fish mode	l with a	single cy	linder, (b)	Schemati	c of the fish	model
with two	cylin	ders ir	the tanden	n arrangei	ment, (c	c) Schemat	ic of the fi	sh model	with two cyl	inders
in the sid	de-by-	side a	rrangement							19
Figure 2	-4 D20	Q9 vel	locity set							23
Figure 2	-5 Sch	emati	c of the con	nputation	al doma	ain				25
Figure 2	-6 Vali	idatio	n results for	cases: (a)	$C_D \& C$	$C_L$ of a sin	gle traveli	ng wavy fo	oil at $Re_U =$	5000,
(b) prop	ulsive	veloc	cities of a	self-prop	elled ur	ndulatory	foil at <i>Re</i>	= 500 &	1000 and (	c) gap
spacing	betwee	en two	foils G for	frequenc	y ratios	Fr = 1.0	and 1.7			27
Figure 2	2-7 Tir	ne his	stories of di	rag coeffi	icient C	$_{D}$ (left) an	d lift coef	ficient $C_L$	(right) of th	ne fish
behind the	he sing	gle cyl	inder with	three diffe	erent ty	pes of mes	h employe	ed		29
Figure 2	2-8 Tir	ne his	stories of di	rag coeffi	icient C	$_{D}$ (left) an	d lift coef	ficient $C_L$	(right) of th	ne fish
behind t	wo tan	dem c	vlinders wi	th three d	lifferent	types of r	nesh empl	oved		29

Figure 3-1 Performance parameters for free-stream velocities $U_{\infty}^* = 2.5$ , 5 and 7.5 with and
without the presence of the cylinder: (a) time-averaged drag coefficient $(\overline{C_D})$ , (b) root-mean
squared lift coefficient ( $C_{Lrms}$ ) and (c) time-averaged power coefficient ( $\overline{C_P}$ ) of the fish
Figure 3-2 Vorticity contours of fluid flow across the cylinder passing through the fish body with
different free-stream velocities: (a) $U_{\infty}^* = 2.5$ , $U_{\infty}^* = 5$ and $U_{\infty}^* = 7.5$
Figure 3-3 Instantaneous velocity field overlaid on vorticity contours (left), drag coefficient $C_D$
(centre) and lift coefficient $C_L$ (right) at the relevant time step when the fish body experiences the
smallest $C_D$ and the largest magnitude of $C_L$ among $U_\infty^*=2.5$ , 5 and 7.5. Red represents
counterclockwise vorticity while blue represents clockwise vorticity. Blue circles and red dash
lines represent the corresponding smallest $C_D$ and largest magnitude of $C_L$ respectively at the
relevant time steps
Figure 3-4 Instantaneous velocity field overlaid on vorticity contours (left), lift coefficient $C_L$
(centre), coefficient of power consumption $ C_{Pc} $ and coefficient of power extraction $ C_{Pe} $ (right)
at the relevant time step when the fish body experiences the smallest $C_D$ and the largest magnitude
of $C_L$ among $U_{\infty}^* = 2.5$ , 5 and 7.5. Red dash lines represent the corresponding largest magnitude
of $C_L$ , $ C_{Pc} $ and $ C_{Pe} $ at the relevant time steps
of $C_L$ , $ C_{Pc} $ and $ C_{Pe} $ at the relevant time steps
of $C_L$ , $ C_{Pc} $ and $ C_{Pe} $ at the relevant time steps
of $C_L$ , $ C_{Pc} $ and $ C_{Pe} $ at the relevant time steps
of $C_L$ , $ C_{Pc} $ and $ C_{Pe} $ at the relevant time steps
of $C_L$ , $ C_{Pc} $ and $ C_{Pe} $ at the relevant time steps
of $C_L$ , $ C_{Pc} $ and $ C_{Pe} $ at the relevant time steps
of $C_L$ , $ C_{Pc} $ and $ C_{Pe} $ at the relevant time steps
of $C_L$ , $ C_{Pc} $ and $ C_{Pe} $ at the relevant time steps
of $C_L$ , $ C_{Pc} $ and $ C_{Pe} $ at the relevant time steps
of $C_L$ , $ C_{Pc} $ and $ C_{Pe} $ at the relevant time steps
of $C_L$ , $ C_{Pc} $ and $ C_{Pe} $ at the relevant time steps
of $C_L$ , $ C_{Pc} $ and $ C_{Pe} $ at the relevant time steps

Figure 3-8 Pressure contours (left), force diagrams (centre left), velocity diagrams (centre right)
and power diagrams (right) along fish body boundary at the relevant time step when the fish body
experiences the largest $C_D$ and the smallest magnitude of $C_L$ among $U_\infty^*=2.5,5$ and $7.540$
Figure 3-9 Time variation of $C_D$ (left) and $C_L$ (right) of the fish undulating downstream of the
cylinder at $d_x^*=4$ for 50 tail-beat period $(T_P)$ from $t^*=50$ to 100 for cases of $U_\infty^*=2.5$ , 5 and
7.5
Figure 3-10 Fourier spectra of $\mathcal{C}_D$ (left) and $\mathcal{C}_L$ (right) on the fish undulating downstream of the
cylinder at $d_x^* = 4$ for cases of $U_\infty^* = 2.5$ , 5 and 7.5 resepctively
Figure 3-11 Performance parameters for streamwise distances $d_x^* = 1, 2, 3 \& 4$ and without the
presence of the cylinder: (a) time-averaged drag coefficient ( $\overline{C_D}$ ), (b) root-mean squared lift
coefficient ( $C_{Lrms}$ ) and (c) time-averaged power coefficient ( $\overline{C_P}$ ) of the fish
Figure 3-12 Instantaneous velocity field overlaid on vorticity contours (left), pressure contours
(centre), force diagrams along fish body boundary (right) at $t^* = 90$ for $d_x^* = 1, 2, 3 \& 4$ 46
Figure 3-13 Performance parameters for crossflow distances $d_y^* = 0, 1, 2, 3 \& 4$ and without the
presence of the cylinder: (a) time-averaged drag coefficient $(\overline{C_D})$ , (b) root-mean squared lift
coefficient ( $C_{Lrms}$ ) and (c) time-averaged power coefficient ( $\overline{C_P}$ ) of the fish
Figure 3-14 Instantaneous vorticity contours (left), pressure contours (centre), force diagrams
along fish body boundary (right) at $t^* = 90$ for $d_y^* = 0, 1, 2, 3 & 4$
Figure 3-15 Performance parameters for diameter of the cylinder $D^* = 0.5, 1, 2, 3, 4, 5, 6 & 7$ and
without the presence of the cylinder: (a) time-averaged drag coefficient ( $\overline{C_D}$ ), (b) root-mean
squared lift coefficient $(C_{Lrms})$ and (c) time-averaged power coefficient $(\overline{C_P})$ of the fish
Figure 3-16 Instantaneous vorticity contours (left), pressure contours (centre), force diagrams
along fish body boundary (right) at $t^* = 90$ for $D^* = 0.5, 1, 2, 3, 4, 5, 6 & 7$
Figure 4-1 Comparison of performance parameters between undulation with and without rotation
at different streamwise distances with the cylinder $d_x^* = 1, 2, 2.5, 2.6, 2.7, 2.8, 2.9, 3 & 4$ and
without the presence of the cylinder: (a) time-averaged drag coefficient $(\overline{C_D})$ , (b) root-mean
squared lift coefficient $(C_{Lrms})$ and (c) time-averaged power coefficient $(\overline{C_P})$ of the fish 57
Figure 4-2 Instantaneous velocity field overlaid on vorticity contours (left), drag coefficient $\mathcal{C}_D$
(centre), and lift coefficient $C_L$ (right) at the relevant time step when the fish body undulates only

at $d_x^* = 3$ and 4 respectively and experiences the largest $C_D$ . Red circles and dash lines represent
the corresponding $C_D$ and $C_L$ respectively at the relevant time steps for the largest $C_D$
Figure 4-3 Pressure contours (left), force diagrams (centre) and velocity diagrams (right) along
fish body boundary at the relevant time step when the fish body undulates only at $d_x^* = 3$ and 4
and experiences the largest $C_D$ . 59
Figure 4-4 Instantaneous velocity field overlaid on vorticity contours (left), drag coefficient $\mathcal{C}_D$
(centre), and lift coefficient $\mathcal{C}_L$ (right) at the relevant time step when the fish body undulates only
at $d_x^* = 3$ and 4 respectively and experiences the smallest $C_D$ . Red circles and dash lines represent
the corresponding $C_D$ and $C_L$ respectively at the relevant time steps for the smallest $C_D$ 60
Figure 4-5 Pressure contours (left), force diagrams (centre) and velocity diagrams (right) along
fish body boundary at the relevant time step when the fish body undulates only at $d_x^*=3$ and $4$
and experiences the smallest $C_D$
Figure 4-6 Instantaneous velocity field overlaid on vorticity contours (left), drag coefficient $\mathcal{C}_D$
(centre), and lift coefficient $\mathcal{C}_L$ (right) at the relevant time step when the fish body undulates only
at $d_x^* = 3$ and 4 respectively and experiences the largest magnitude of $C_L$ . Red dash lines and
circles represent the corresponding $\mathcal{C}_D$ and $\mathcal{C}_L$ respectively at the relevant time steps for the largest
magnitude of $C_L$ .
Figure 4-7 Pressure contours (left), force diagrams (centre) and velocity diagrams (right) along
fish body boundary at the relevant time step when the fish body undulates only at $d_x^*=3$ and $4$
and experiences the largest magnitude of $C_L$ . 62
Figure 4-8 Comparison of vorticity contours with instantaneous velocity field overlaid for fish
undulation with rotation at different streamwise distances with the cylinder $d_x^* =$
1, 2, 2.5, 2.6, 2.7, 2.8, 2.9, 3 & 4 at the same time step
Figure 4-9 Instantaneous velocity field overlaid on vorticity contours (left), drag coefficient $\mathcal{C}_D$
(centre left), lift coefficient $C_L$ (centre right) and angle of rotation about centroid $\theta$ (right) at the
relevant time step when the fish body undulates and rotates at $d_x^* = 2.8$ and 2.9 respectively and
experiences the largest $C_D$ . Positive angle of rotation represents anticlockwise rotation while
negative angle represents clockwise rotation. Red circles and dash lines represent the
corresponding $C_D$ , $C_L$ and $\theta$ respectively at the relevant time steps for the largest $C_D$

Figure 4-10 Pressure contours (left), force diagrams (centre) and velocity diagrams (right) along
fish body boundary at the relevant time step when the fish body undulates and rotates at $d_x^* = 2.8$
and 2.9 and experiences the largest $C_D$ . 64
Figure 4-11 Instantaneous velocity field overlaid on vorticity contours (left), drag coefficient $\mathcal{C}_D$
(centre left), lift coefficient $C_L$ (centre right) and angle of rotation about centroid $\theta$ (right) at the
relevant time step when the fish body undulates and rotates at $d_x^* = 2.8$ and 2.9 respectively and
experiences the smallest $C_D$ . Red circles and dash lines represent the corresponding $C_D$ , $C_L$ and $\theta$
respectively at the relevant time steps for the smallest $C_D$
Figure 4-12 Pressure contours (left), force diagrams (centre) and velocity diagrams (right) along
fish body boundary at the relevant time step when the fish body undulates and rotates at $d_x^* = 2.8$
and 2.9 and experiences the smallest $C_D$
Figure 4-13 Instantaneous velocity field overlaid on vorticity contours (left), drag coefficient $C_D$
(centre left), lift coefficient $C_L$ (centre right) and angle of rotation about centroid $\theta$ (right) at the
relevant time step when the fish body undulates and rotates at $d_x^* = 2.8$ and 2.9 respectively and
experiences the largest magnitude of $C_L$ . Red circles and dash lines represent the corresponding
$C_D$ , $C_L$ and $\theta$ at the relevant time steps for the largest magnitude of $C_L$
Figure 4-14 Pressure contours (left), force diagrams (centre) and velocity diagrams (right) along
fish body boundary at the relevant time step when the fish body undulates and rotates at $d_x^* = 2.8$
and 2.9 and experiences the largest magnitude of $C_L$ . 67
$Figure\ 4-15\ Comparison\ of\ performance\ parameters\ between\ undulation\ only\ and\ undulation\ with the performance\ parameters\ between\ undulation\ only\ and\ undulation\ with the performance\ parameters\ between\ undulation\ only\ and\ undulation\ with the performance\ parameters\ between\ undulation\ only\ and\ undulation\ with the performance\ parameters\ between\ undulation\ only\ and\ undulation\ with the performance\ parameters\ between\ undulation\ only\ and\ undulation\ with the performance\ parameters\ between\ undulation\ only\ and\ undulation\ with the performance\ parameters\ between\ undulation\ only\ and\ undulation\ with the performance\ parameters\ between\ undulation\ only\ and\ undulation\ with\ performance\ parameters\ between\ undulation\ only\ and\ undulation\ with\ performance\ parameters\ between\ undulation\ only\ and\ undulation\ with\ performance\ parameters\ performance\ parameters\ performance\ parameters\ performance\ parameters\ performance\ parameters\ performance\ parameters\ performance\ performance\ parameters\ performance\ pe$
rotation at crossflow distance with the cylinder $d_y^*=0$ , 0.1, 0.2, 0.3, 0.4, 0.5, 1, 2 & 3 and without
the presence of the cylinder: (a) time-averaged drag coefficient $(\overline{C_D})$ , (b) root-mean squared lift
coefficient ( $C_{Lrms}$ ) and (c) time-averaged power coefficient ( $\overline{C_P}$ ) of the fish
Figure 4-16 Instantaneous velocity field overlaid on vorticity contours (left), velocity diagrams
along fish body boundary (centre) and angle of rotation about centroid $\theta$ (right) at time steps $t^* =$
90.85, 91.35, 92.2 & 92.75 when the fish body undulates and rotates at $d_y^*=0$ . Red dash lines
represent the corresponding $\theta$ at the relevant time steps
Figure 4-17 Pressure contours (left), force diagrams along fish body boundary (centre) and angle
of rotation about centroid $\theta$ (right) at time steps $t^* = 90.85, 91.35, 92.3 \& 92.75$ when the fish

body undulates and rotates at $d_y^* = 0$ . Red dash lines represent the corresponding $\theta$ at the relevant
time steps
Figure 4-18 Instantaneous velocity field overlaid on vorticity contours (left), velocity diagrams
along fish body boundary (centre) and angle of rotation about centroid $\theta$ (right) at time steps $t^*$ =
91.85, 92.35, 92.85 & 93.55 when the fish body undulates and rotates at $d_y^* = 0.5$ . Red dash lines
represent the corresponding $\theta$ at the relevant time steps
Figure 4-19 Pressure contours (left), force diagrams along fish body boundary (centre) and angle
of rotation about centroid $\theta$ (right) at time steps $t^* = 91.85, 92.35, 92.85 \& 93.55$ when the fish
body undulates and rotates at $d_y^* = 0.5$ . Red dash lines represent the corresponding $\theta$ at the
relevant time steps
Figure 4-20 Instantaneous velocity field overlaid on vorticity contours (left), velocity diagrams
along fish body boundary (centre) and angle of rotation about centroid $\theta$ (right) at time steps $t^*$
2, 3.5, 4, 4.5 & 5.2 when the fish body undulates and rotates at $d_y^* = 0.1$ . Red dash lines represent
the corresponding $\theta$ at the relevant time steps
Figure 4-21 Pressure contours (left), force diagrams along fish body boundary (centre) and angle
of rotation about centroid $\theta$ (right) at time steps $t^* = 2, 3.5, 4, 4.5 \& 5.2$ when the fish body
undulates and rotates at $d_y^* = 0.1$ . Red dash lines represent the corresponding $\theta$ at the relevant
time steps
Figure 4-22 Instantaneous velocity field overlaid on vorticity contours (left), velocity diagrams
along fish body boundary (centre) and angle of rotation about centroid $\theta$ (right) at time steps $t^* =$
2, 3.9, 5 & 7.1 when the fish body undulates and rotates at $d_y^* = 0.2$ . Red dash lines represent the
corresponding $\theta$ at the relevant time steps
Figure 4-23 Pressure contours (left), force diagrams along fish body boundary (centre) and angle
of rotation about centroid $\theta$ (right) at time steps $t^* = 2, 3.9, 5 \& 7.1$ when the fish body undulates
and rotates at $d_y^* = 0.2$ . Red dash lines represent the corresponding $\theta$ at the relevant time steps
78
Figure 4-24 Instantaneous velocity field overlaid on vorticity contours (left), velocity diagrams
along fish body boundary (centre) and angle of rotation about centroid $\theta$ (right) at time steps $t^* =$
2, 3, 4.05, 5 & 5.5 when the fish body undulates and rotates at $d_y^* = 0.3$ . Red dash lines represent
the corresponding $\theta$ at the relevant time steps

Figure 4-25 Pressure contours (left), force diagrams along fish body boundary (centre) and angle
of rotation about centroid $\theta$ (right) at time steps $t^* = 2, 3, 4.05, 5 \& 5.5$ when the fish body
undulates and rotates at $d_y^* = 0.3$ . Red dash lines represent the corresponding $\theta$ at the relevant
time steps
Figure 4-26 Instantaneous velocity field overlaid on vorticity contours (left), velocity diagrams
along fish body boundary (centre) and angle of rotation about centroid $\theta$ (right) at time steps $t^* =$
1.5, 2.55, 3.95, 5 & 5.4 when the fish body undulates and rotates at $d_y^* = 0.4$ . Red dash lines
represent the corresponding $\theta$ at the relevant time steps
Figure 4-27 Pressure contours (left), force diagrams along fish body boundary (centre) and angle
of rotation about centroid $\theta$ (right) at time steps $t^* = 1.5, 2.55, 3.95, 5 & 5.4$ when the fish body
undulates and rotates at $d_y^* = 0.4$ . Red dash lines represent the corresponding $\theta$ at the relevant
time steps
Figure 5-1 (a) Streamwise trajectories and (b) angles of rotation about centroid $\theta$ of the fish in
cases with different initial streamwise positions $d_x^* = 2.8$ to 4. The case without the presence of
the cylinder is also included as a reference
Figure 5-2 Comparison of instantaneous velocity field overlaid on vorticity contours when the fish
body undulates, rotates and translates in streamwise direction from the initial position of $d_x^* = 3.4$
(left) and 3.5 (right) for time step of $t^* = 50, 50.5, 51, 51.5, 51.7 \& 52.$
Figure 5-3 Comparison of instantaneous velocity field overlaid on vorticity contours when the fish
body undulates, rotates and translates in streamwise direction from the initial position of $d_x^* = 3.6$
(left) for time step of $t^*=50$ , 50.5, 51, 51.5, 51.7 & 52 and $d_x^*=3.7$ (right) for time step of $t^*=50$
50, 50.5, 51 & 51.5
Figure 5-4 (a) Streamwise trajectories and (b) angles of rotation about centroid $\theta$ of the fish in
cases with different initial streamwise positions among $d_x^* = 3.4 \& 3.5$ and varying crossflow
positions between $d_y^* = 0, 0.1, 0.2$ and 0.5. The case without the presence of the cylinder is also
included as a reference
Figure 5-5 Comparison of instantaneous velocity field overlaid on vorticity contours when the fish
body undulates, rotates and translates in streamwise direction from the initial position of $d_x^* =$
3.4, $d_y^* = 0$ (left), $d_x^* = 3.4$ , $d_y^* = 0.1$ (centre) and $d_x^* = 3.4$ , $d_y^* = 0.2$ (right) for time step of
$t^* = 50, 50.5, 51, 51.5 \& 52$

Figure 5-6 (a) Streamwise trajectories, (b) crossflow trajectories and (c) angles of rotation about
centroid $\theta$ of the fish in cases with different initial streamwise positions $d_x^* =$
$3, 3.1, 3.2, 3.3, 3.4, 3.5, 3.6, 3.7, 3.8, 3.9 \ \& \ 4.$ The case without the presence of the cylinder is also
included as a reference
$Figure \ 5-7 \ Comparison \ of \ instantaneous \ velocity \ field \ overlaid \ on \ vorticity \ contours \ when \ the \ fish \ contours \ when \ the \ contours \ contours \ when \ contours \ contours \ when \ contours \$
body swims freely from the initial position of $d_x^*=3.4$ , $d_y^*=0$ (left) and $d_x^*=3.5$ , $d_y^*=0$ (right)
for time step of $t^* = 50, 51, 52, 53, 54, 55 & 56$ .
Figure 5-8 Comparison of instantaneous velocity field overlaid on vorticity contours when the fish
body swims freely from the initial position of $d_x^* = 3.6$ , $d_y^* = 0$ for time step of $t^* =$
50, 51, 52, 53, 54, 55 & 56 (left) and $d_x^* = 3.7$ , $d_y^* = 0$ for $t^* = 50$ , 51 & 52 (right)
Figure 6-1 Phase diagram for the two motion modes in the $d_x^* - D_x^*$ plane. Symbols $\circ$ , + represent
drifting upstream (DU) and drifting downstream (DD) modes respectively. The red dashed line
separates the region of DU and DD modes. The blue dashed line defines the transition regions
between the boundary of DU and DD modes
Figure 6-2 Comparison of (a) streamwise trajectories, (b) crossflow trajectories and (c) angles of
rotation about centroid $\theta$ of the fish between initial streamwise positions $d_x^* = 2.9 \& 3$ with the
same streamwise distance between two tandem cylinders $D_x^* = 1.3$ 100
$Figure\ 6-3\ Comparison\ of\ instantaneous\ velocity\ field\ overlaid\ on\ vorticity\ contours\ when\ the\ fish\ contours\ when\ the\ co$
body swims freely from the initial streamwise position of $d_x^* = 2.9$ for time step of $t^* = 50$ to $56$
(left) and $d_x^* = 3$ for $t^* = 50$ to 54 (right) with the same streamwise distance between two tandem
cylinders $D_x^* = 1.3$
Figure 6-4 Comparison of (a) streamwise trajectories, (b) crossflow trajectories and (c) angles of
rotation about centroid $\theta$ of the fish between initial streamwise positions $d_x^*=3.4~\&~3.5$ with the
same streamwise distance between two tandem cylinders $D_x^* = 1.1$ . This is one of the transition
regions (blue dashed line) defined in Figure 6-1.
$Figure\ 6-5\ Comparison\ of\ instantaneous\ velocity\ field\ overlaid\ on\ vorticity\ contours\ when\ the\ fish\ contours\ when\ the\ co$
body swims freely from the initial streamwise position of $d_x^* = 3.4$ for time step of $t^* = 50$ to $54$
(left) and $d_x^* = 3.5$ for $t^* = 50$ to 56 (right) with the same streamwise distance between two
tandem cylinders $D_x^* = 1.1$ . This is one of the transition regions (blue dashed line) defined in
Figure 6-1

Figure 6-6 Comparison of (a) streamwise trajectories, (b) crossflow trajectories and (c) angles of
rotation about centroid $\theta$ of the fish between initial streamwise positions $d_x^*=2.7$ & 2.8 with the
same streamwise distance between two tandem cylinders $D_x^* = 1.4$ . This is one of the transition
regions (blue dashed line) defined in Figure 6-1.
Figure 6-7 Comparison of instantaneous velocity field overlaid on vorticity contours when the fish
body swims freely from the initial streamwise position of $d_x^* = 2.7$ for time step of $t^* = 50$ to $56$
(left) and $d_x^* = 2.8$ for $t^* = 50$ to 58 (right) with the same streamwise distance between two
tandem cylinders $D_x^* = 1.4$ . This is one of the transition regions (blue dashed line) defined in
Figure 6-1
Figure 6-8 Phase diagram for the three motion modes in the $d_x^* - D_y^*$ plane. Symbols $\circ$ , + & ×
represent drifting upstream (DU), drifting downstream (DD) and drifting up then down (DUD)
modes respectively
Figure 6-9 Comparison of instantaneous velocity field overlaid on vorticity contours when the fish
body swims freely from the initial streamwise position of $d_x^* = 3.5$ for time step of $t^* = 50$ to $60$
with crossflow distance between two side-by-side cylinders $D_y^* = 1.1$ (left), for $t^* = 50$ to 57
with $D_v^* = 1.2$ (centre) and for $t^* = 50$ to 56 with $D_v^* = 1.3$ (right) respectively

# **List of Tables**

Table 1.1 Summary of studies utilising numerical simulation on fish-like models	10
Table 1.2 Summary of numerical studies on the interaction between swimmer and	stationary
object(s)	12
Table 2.1 Definitions of controlled parameters in the study	17
Table 2.2 Definitions and values of relevant parameters for the resolution test	28
Table 2.3 Types of test case for the resolution test	28
Table 3.1 Definitions and chosen values of relevant parameters in Chapter 3	31
Table 4.1 Definitions and chosen values of relevant parameters in Chapter 4	55
Table 5.1 Definitions and chosen values of relevant parameters in Chapter 5.1	85
Table 5.2 Definitions and chosen values of relevant parameters in Chapter 5.2	91
Table 6.1 Definitions and chosen values of relevant parameters in Chapter 6.1	98
Table 6.2 Definitions and chosen values of relevant parameters in Chapter 6.2	108

# Nomenclature

Symbol	Represent		
$A_{max}$	Maximum tail-beat amplitude		
D	Cylinder diameter		
$D^*$	Normalized cylinder diameter		
$d_x$	Streamwise distance between fish and cylinder		
$d_x^*$	Normalized streamwise distance between fish and cylinder		
$d_{y}$	Crossflow distance between fish and cylinder		
$d_{\mathcal{Y}}^*$	Normalized crossflow distance between fish and cylinder		
$D_x$	Streamwise distance between cylinders		
$D_{x}^{*}$	Normalized streamwise distance between cylinders		
$D_{y}$	Crossflow distance between cylinders		
$D_{\mathcal{Y}}^*$	Normalized crossflow distance between cylinders		
$f_b$	Beating frequency		
$f_{un}$	Tail-beat / undulating frequency		
$f_{vor}$	Vortex shedding frequency		
L	Fish body length		
$Re_{fish}$	Reynolds number based on fish undulation		
$Re_{\infty}$	Reynolds number based on free-stream velocity		
St	Strouhal number		
t	Time		
$t^*$	Normalized time		
$T_P$	Tail-beat period		
$U_{\infty}$	Free-stream velocity		
$U_\infty^*$	Normalized free-stream velocity		
$U_{ref}$	Reference velocity		
$V_{max}$	Maximum undulatory velocity		

## **Chapter 1** Introduction

## 1.1. Background

Migratory movement of fish has long been recognized along with our human history. The phenomenon has attracted attention from different parties, such as biologists, naturalists and ecologists. Details recorded about fish migration could be traced to the early 19<sup>th</sup> century [1]. In the life cycle, fish would travel considerably long distances between habitats to perform different actions, from feeding, refuging to avoid disadvantageous environment to reproduction of offsprings [2]. As defined by McDowall [3], anadromous fish is a class of diadromous fish which migrate from sea to freshwater for spawning in their lifespans. A typical known species of anadromous fish is salmon. Along their migration, several habitats are commonly found to be high-energy environment, such as rivers, streams and coastal areas. These environments pose challenges to fish as the water flow velocities are usually high. As fish normally travel long distances in the migration with slow-swimming speed, this may prevent them from achieving their maximum distances without rests [4]. Therefore, in order to swim upstream against strong downstream flow, places for rest or refuging are definitely needed.

Numerous field studies have been conducted by aquatic biologists in lakes, streams, ponds and oceans [5]. It was commonly observed that fish often hold stationary behind physical objects, such as rocks, coral reefs, tree trunks and water plants. These places serve as good places for fish refuging. Diana [10] reported that currents created among boulders, logs or roots provide slow flow regions for fish to hold station, thus reduce their energy expenditure. Besides, it was reported by Gerstner [9] that tidally swept environment, such as substratum ripple, would also be utilized by Atlantic cod for refuging. McLaughlin and Noakes [11] conducted field studies and experiments to examine the influence on fish swimming behaviour by the introduction of the physical structure which generates current-velocity refuge. Heggenes [11] suggested that some fish have evolved to possess the ability to respond and adapt the change of habitat. As mentioned by Liao et al. [13], fish may take advantage from shedding vortices from stationary objects and extract energy from them. This could help reduce energy expenditure for the long journeys.



Figure 1-1 A rockfish swims and refuges behind rocks. (adapted from https://www.scubadiving.com/unexpected-friendship-vermillion-rockfish)

From all the studies aforementioned, it is attested the importance of understanding how fish interact with the habitats, particularly stationary objects, in different aspects. Fishery scientists could use the knowledge to assess the impact of hydrodynamic influence by these stationary objects in certain aquatic environment on fish migration. This could help commercial decision on fish farm design, management of aquatic habitats and construction of fish passage. Civil engineers could utilize the understanding to design and construct infrastructure, like dams, canals, culverts, such that the migratory movement of fish would not be hindered. Biomechanists could apply the findings in designing hydrodynamic vehicles and robots for navigation and exploration of aquatic environment.

Acknowledging the biological, ecological and economical importance and demand on understanding the interaction between fish and stationary objects in the natural habitat, research have been conducted throughout decades. In the past, research was mainly carried out through means of experiment. Despite the applied benefits on other mentioned industries and fields, relatively few laboratory studies were made due to the complexity and difficulties of experiments. It was reported by Liao et al. [14] that difficulty existed in generation and interpretation of repeatable hydrodynamic perturbations in the past. With rapid technological advancement in the past few decades, the development of charge-coupled devices (CCD), cameras with higher speed and digital image processing techniques have revolutionized flow visualization. Application of

these advanced apparatus and equipment enables more accurate capture of three-dimensional flow structure around swimming fish with higher resolution. In other words, accuracy and comprehensiveness of experimental results are enhanced.

At the same time, the flourishing development of computer science in the past decade has improved computational speed and capacity significantly. Therefore, numerical simulation, such as Computational Fluid Dynamics (CFD), is largely utilized for solving problems related to fluid flow. Research on fish-like model swimming is also largely benefited by this computational development. Since then, numerical solvers were developed and applied in numerous studies of fish swimming in the recent decade. The research direction is widely spread with topics covering fish schooling [15], fish swimming behind a rigid body [16] to energy extraction from environmental vortices [17]. Each study contributes to knowledge of fish swimming, albeit possesses its limitation. For example, Wang et al. [18] studied the self-propelled plate in the wake behind two cylinders in tandem arrangement. It sheds light on interaction between the cylinders and swimmer, but the self- propelled flexible plate could not resemble much detail of fish-like model. Thekkethil et al. [18] conducted the hydrodynamics study for different types of fish-like undulating foil. However, the study focused on the single undulating foil, not the interaction with another foil or object. In light of these research gaps, it would be an opportunity to conduct the study on self-propelled fish-like hydrofoil swimming behind multiple cylinders.

#### 1.2. Literature Review

Fish swimming has been extensively studied in many decades. Studies at the early stage mainly focused on classification methodology according to fish swimming mechanism and locomotion [21]. Breder [21] proposed as early as in 1926 the well-structured classification and nomenclature scheme for types of fish swimming. He classified the fish body movement in three forms, namely anguilliform movement, ostraciiform movement and carangiform movement. The body movement was simply described by wordings with sketches. A simplified model was proposed by Lighthill in 1960 as a swimming slender fish. He illustrated the suggested cyclic movement of the fish body through successive drawings on the fish centreline [22]. However, the hydromechanical model was still not described in detail. It was not until 1969 that Lighthill presented a pioneering work in which the anguilliform and carangiform propulsion were described in detail [23]. He measured the

propulsion and illustrated it qualitatively in dimensional grids as shown in Figure 1-2. One year later, fish swimming modes associated with body and caudal fin (BCF) and median and paired fin (MPF) propulsion were further investigated and concluded by Lindsey [28]. He further grouped types of fish swimming further into different modes under BCF and MPF propulsion based on Breder's [21] original classification (see Figure 1-3). The study has created a common standard of classification which is still utilized by researchers nowadays to identify the motion mode of the fish to be examined. Sfakiotakis et al. [32] provided a comprehensive overview of fish swimming modes, particularly on the locomotion and propulsion mechanisms, with the aim to provide tools and motivate more research on biomimetic fish-like robots. They summarized classification scheme along with description on kinematics presented in past decades [21]. Moreover, they introduced analytical approaches to study different swimming modes in a more systematic way. The study mentioned that BCF propulsion is employed by estimated 85% of fish families for propulsive purposes as BCF movement could generate larger thrust and achieve higher acceleration. Under BCF propulsion, movement are further divided into two swimming modes as shown in Figure 1-4, namely undulatory motion and oscillatory motion [30]. Among these two modes, undulatory BCF mode is our focus as the propulsive wave transverses the fish body at a higher speed than the swimming speed, especially angulliform mode in which the whole fish body participates in the undulation.

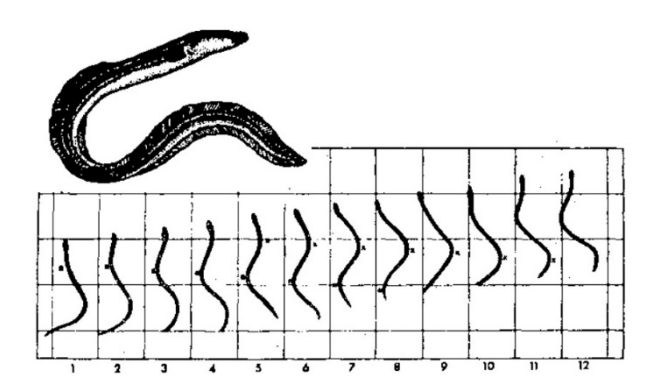


Figure 1-2 Successive position of an eel swimming in water at interval of 0.09s. The side of each square in the grid is 25.4 mm. [23]

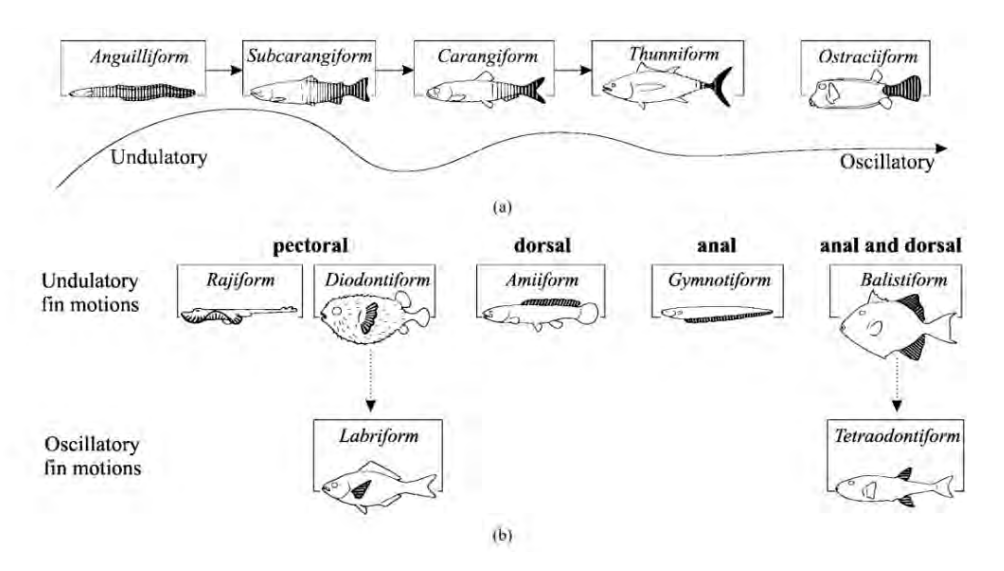


Figure 1-3 Fish swimming modes classified under (a) BCF propulsion and (b) MPF propulsion. [28]

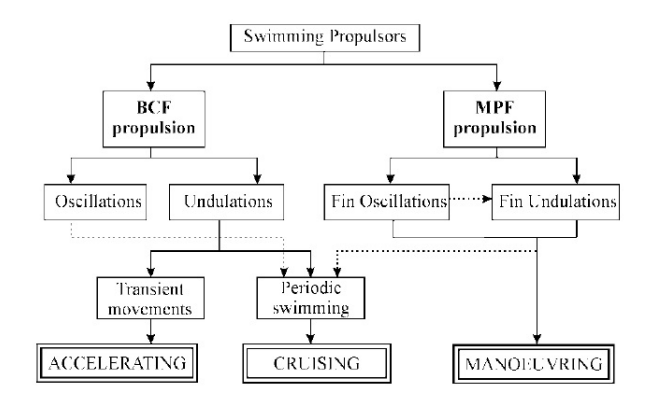


Figure 1-4 Relation between propulsion modes and swimming motions. [30]

With more understanding of the kinematics of fish, researchers extended the study to the interaction between fish and fluid through both experiment and simulation. Simplified swimmer models were commonly used in computational simulation in early studies. Liu et al. [33] analysed tadpole propulsion using numerical simulation on undulatory locomotion and first confirmed that results of three-dimension and two-dimensional simulation matched with each other. Although the model applied in the computation could not be directly compared with fish, the study still provided insight on the influence of kinematics on the interaction between swimmer and fluid. Carling et al. [35] historically combined the dynamics of swimmer motion and fluid flow to actualize self-propelled swimming. However, the model of the anguilliform swimmer has a square-cornered nose and tail which is not an ideal model (see Figure 1-5). On the experimental side, Müller et al. [36]

observed flow fields and wake structures of free-swimming eels through experiment. Tytell and Lauder [37] performed high resolution particle image velocimetry (PIV) on swimming eels and suggested different wake structures compared with those of Carling et al. and Müller et al. Despite much research being conducted to reveal more knowledge about fish swimming, research area was still confined to interaction with the surrounding flow field. Several research areas involving interaction with induced flow field of neighbouring swimmers and objects in the aquatic environment remained partially understood. Two areas attract attention from researchers of different fields, fish refuging and fish schooling [5]. From evolution throughout thousands of years, fish and other aquatic animals have learnt to take advantage of mother nature by interacting with the surrounding flow field. Interaction does not only happen between fish and fluid flow, but also among fishes and with physical objects [18]. Fish schooling and fish refuging are the behaviour observed from fish which correspond to the interaction mentioned.

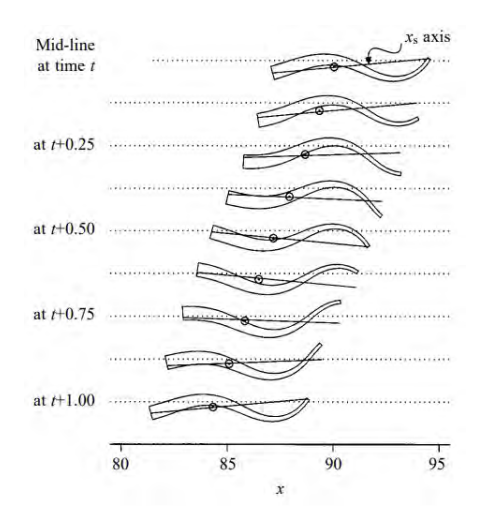


Figure 1-5 Change of body shape of the anguilliform model from time t to t + 1.00. [35]

Fish schooling refers to the movement of multiple fish swimming together in a well organised and synchronised pattern. It has been widely studied in decades to reveal the benefits from interaction between fish in different arrangements and relevant details in terms of hydrodynamics. Several research explained that the following fish could be beneficial through capturing energy from vortices generated from the leading fish to minimise the locomotion cost. Weihs [38] was one of the earliest to suggest thrust gain by the following fish from induced flow field generated from leading fish in the diamond pattern. Being inspired by Weihs, various research was conducted on

fish schooling through experiment and computational simulation. Dong and Lu [39] numerically investigated fluid flow over travelling wavy foils in side-by-side arrangement and analysed the effect of lateral interference among foils in various performance parameters. Boschitsch et al. [40] showed by experiment that propulsive performance of downstream hydrofoil is influenced by the existence of upstream foil for all conditions. Daghooghi and Borazjani [41] studied mackerel swimming with rectangular pattern and provided significant evidence to support the hypothesis of channelling effect. Through channelling effect, fish gain efficiency because of the decrease of thrust required due to proximity of fish. However, it is commonly observed that the distance between fish in the schooling is not fixed. All the work mentioned could not fully satisfied the observation. Nevertheless, they provided insight to fish schooling and supported the future research work.

In addition to fish schooling, fish could be benefited from the interaction with induced flow field from stationary objects as mentioned. Fish swimming in flowing water, like streams and rivers, are observed in many field studies to swim along turbulence generated downstream of stationary objects [42]. It is believed that fish extract energy through interaction with vortices shed from stationary objects. In light of this theoretical benefit, numerous laboratory studies were carried out to confirm and describe hydrodynamics behind the interaction in details [46]. Liao et al. [48] pointed out experimentally that trout adopts a specific mode of locomotion to exploit vortices in order to reduce muscle activity. In another study, Liao et al. [49] suggested a pattern of movement, Karman gait, is adopted by trout to refuge behind the cylinder. The study discovered that trout exhibits a larger body amplitude with a lower tail-beat frequency than normal steady swimming. This experiment proposed that Karman gait is adopted to reduce locomotor cost by changing fish body kinematics to capture energy from wake formed behind the cylinder.

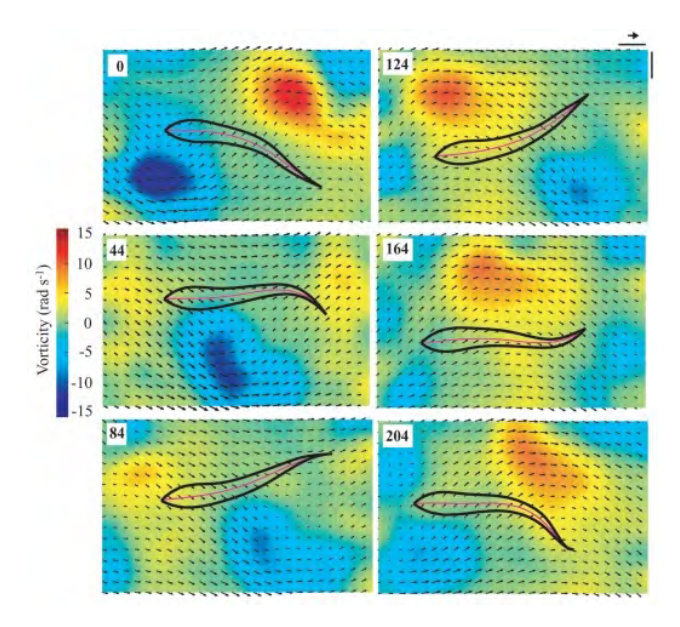


Figure 1-6 Time history of the body movement superimposed on the vorticity contours with velocity fields to show the interaction of trout with vortices from the cylinder. [49]

Inspired by the work of Liao's group, many studies were conducted with the focus on the effect of von Karman vortex street produced by stationary objects on swimming performance of plates, hydrofoils and live fishes. An interesting study was carried out by Beal et al. [50] showing a dead fish being propelled passively through resonance of flexible body with oncoming vortices from the wake of a bluff cylinder. Further studies [51] found that Karman gait would be greatly affected by flow speed, fish size and undulating frequency. However, as mentioned by Tytell [53], experiment is limited by the difficulty imposed on controlling over fish swimming. Also, another difficulty was illustrated by Dabiri [54] in obtaining forces on the fish and measuring swimming efficiency.

Benefiting by flourishing development of computer science in the past two decades, numerical simulation becomes a popular method, other than the traditional experiment, for studying fluid-structure interaction. Carling et al. [35] conducted two-dimensional simulation study of eel swimming as early as in 1998 despite the discrepancy with experimental results on the wake structure. This disagreement was later clarified by Kern and Koumoutsakos [55] through three-dimensional numerical simulation (see Figure 1-7). They transformed the equation of anguilliform motion of presented by Carling et al. as shown in equation (1.1) to have direct comparison with results of Carling et al. The research explained the insufficiency of two-dimensional to reveal the

flow field in detail. With comprehensive designs and strict validation against experimental results, numerical simulation could actually complement experiment by presenting more details and providing quantitative data which would be difficult to obtain from experiments. Wolfgang et al. [56] conducted a simulation on swimming giant danio and compared with experimental result. The comparison showed well-matched results on the velocity and vorticity fields.

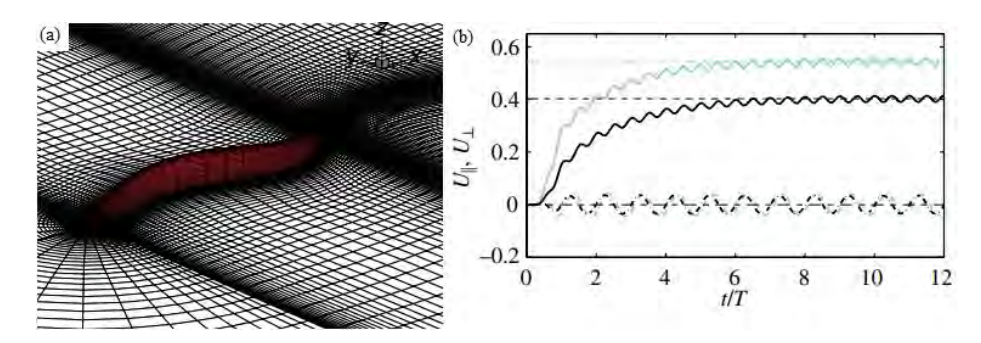


Figure 1-7 (a) Diagram of the three-dimensional anguilliform model and (b) time variation of longitudinal velocity  $U_{\parallel}$  and lateral velocity  $U_{\perp}$  in twelve cycles as the self-propelled swimmer accelerates from rest. Solid lines represent  $U_{\parallel}$  and broken lines represent  $U_{\perp}$  while 2D cases are in cyan and 3D cases are in black. [55]

$$y_s(s,t) = 0.125 \frac{s + 0.03125}{1.03125} \sin\left[2\pi \left(s - \frac{t}{T}\right)\right]$$
(1.1)

where  $y_s$  describes lateral displacement of the mid-line in a local coordinate system, s is the position along the body, t is the dimensionless time and T is undulation cycle.

From that time on, many simulations were carried out to study hydrodynamics of fish swimming. Liu et al. [33] conducted computational fluid dynamics studies on tadpole swimming. Borazjani and Sotiropoulos [57] compared the hydrodynamics of anguilliform and carangiform swimming in the transitional and inertial flow regimes through analysis on swimming performance in terms of drag force on fish and power required for undulation. It was revealed that carangiform swimmers achieve higher speeds and swimming efficiencies at high Reynolds numbers in the expense of higher energy cost than anguilliform swimmers. The two simulations share a common conclusion that three-dimensional wake structure depends mainly on Strouhal number. Thekkethil et al. [19] examined the hydrodynamic behaviour for various types of undulating motion using a generic kinematic model. The flexibility and wavelength of undulation of a rigid NACA0012 hydrofoil

were altered to simulate various types of muscle-induced flexible motion or manoeuvrability. However, the swimmer models in these studies were underdeveloped without possession of the ability of self-propulsion. They only undulate according to the prescribed motion equations at the fixed position.

Self-propulsion study is necessary because fish movement is basically transient with swimming velocity and flow field surrounding varied due to body undulation. It can guarantee that dynamical behaviours of fish are determined by hydrodynamic forces. In light of the importance of autonomous swimming, numerous studies have been performed, as listed in Table 1.1. Among these research work, Carling et al. [35] and Kern and Koumoutsakos [55] presented famous studies on simulation of self-propelled anguilliform swimming. Wei et al. [59] evaluated and optimized swimming performance of self-propelled fish-like model. Their simulation results found that propulsion achieving high efficiency requires a high Strouhal number and a low Reynolds number. Recently, a parametric study on the effect of body thickness on hydrodynamic performance was conducted by Xiong et al. [60]. They compared performance factors, such as swimming velocity, pressure, thrust generated and energy consumption among six swimmer models and concluded that thicker body generates higher thrust. In these studies, fish swimming is not prescribed but a result from the motion of fish body, flow field around the fish and interaction between fish and wake. All these investigations shed light on interaction with fluid flow and later stationary objects.

Table 1.1 Summary of studies utilising numerical simulation on fish-like models

Author	Fish model	Self-Propulsion	Dimensions
Liu et al. [33]	Tadpole	No	2D
Carling et al. [35]	Anguilliform	Yes	2D
Kern and Koumoutsakos [55]	Anguilliform	Yes	2D, 3D
Borazjani and Sotiropoulos [57]	Carangiform, mackerel-like	No	3D
Borazjani and Sotiropoulos [58]	Anguilliform, lamprey-like	No	3D
Thekkethil et al. [19]	Fish-like undulating & No		2D
	pitching body		
Wei et al. [59]	Sub-carangiform	Yes	2D
Xiong et al. [60]	Carangiform	Yes	2D

The necessity of investigation on the interaction between fish and stationary objects emerges as the response to the biological and economical importance mentioned in Chapter 1.1. With more understanding on hydrodynamics of fish swimming through numerical simulations and evidence from experiments [50], studies using numerical simulation on swimmer behind stationary objects were also commenced. It is noticed that some studies on the interaction between the cylinder and flexible plate or fish-like model were carried out. Eldredge and Pisani [61] studied a passive fishlike system consisted of two-dimensional linked rigid ellipse bodies in the wake of a circular cylinder. Shao et al. [62] used a modified immersed boundary method (IBM) to investigate the hydrodynamic performance of a fish-like undulating foil in the wake of a cylinder numerically. Tian et al. [63] have conducted the study in the interaction between a flexible filament and a rigid body located downstream by applying numerical simulation. In spite of the fruitful results obtained, they did not use any self-propelled fish model. An interesting computational study was conducted by Yuan and Hu [52] using a more realistic swimmer, tadpole, in the wake of a D-section cylinder. Nevertheless, the tadpole undulates only without the ability to self-propel. Studies involving selfpropelled swimmer could still be found. Park et al. [64] conducted the study on self-propelled flexible fin in the wake of a circular cylinder numerically but the modelling of swimmer is simple to represent real fish swimming. Studies by Li et al. [65], Tong et al. [66] and Wu et al. [16] are examples well developed fish-like models with more complex motions. Tang et al. [79] utilised an undulatory NACA0012 airfoil as the fish-like model to investigate the entrainment of a fish in vortices generated in wake of a semi-cylinder. The study provided valuable insights into the influence of vortices shed from the cylinder on the fish's swimming performance. This could contribute as the basic knowledge when we investigate the fish swimming behind a single cylinder. Being inspired by the forementioned work, Wang et al. [80] has recently conducted the study on the effects of longitudinal distance away from a semi-cylinder and size of the cylinder on the hydrodynamic performance of the undulating fish. The vortex patterns of the vortex-fish interaction were well classified into three types to analyse the mechanisms by which wake vortices disturbed fish behaviour and the spatial extent of these disturbances. However, the ability of selfpropulsion is absence in the mentioned studies. Therefore, it is necessary to develop a selfpropelled swimming model with complex motion.

On the other hand, studies are noticed being conducted to reveal vortex shedding around multiple cylinders in different arrangements [67]. Stewart et al. [69] also gave a better understanding of fish refuging though investigation on the interaction between fish and wake downstream of two tandem cylinders by experiment. Computational fluid dynamics simulation was also conducted in their study, although only two tandem cylinders were used without the involvement of any self-propelled fish model. Wang et al. [18] numerically studied the locomotion modes of a self-propelled plate behind wakes of two tandem cylinders. However, the self-propelled plate is a simple model which may not be able to resemble fish swimming motion in detail. Some studies focus on the interaction between multiple self-propelled swimmers swimming either side-by-side [39], in tandem with each other [70] or even towards each other [71]. Nevertheless, they are more related to fish schooling than fish refuging.

The recent research by Sparks et al. [81] utilized a combined numerical and experimental approach to reveal the locomotion and swimming kinematics of a rainbow trout behind a 3×5 array of cylinders. CFD simulations were conducted to identify the optimal cylinder arrangements generating periodic Kármán vortex wake downstream of the cylinder array. It aligns with our research focus on multiple cylinders. However, the study on the swimming kinematics behind cylinder arrays was carried out with live rainbow trout in the experimental setup.

Table 1.2 Summary of numerical studies on the interaction between swimmer and stationary object(s)

Author	Swimmer	<b>Self-Propulsion</b>	Stationary Object(s)
Tian et al. [63]	Flexible filament	No	Single cylinder
Eldredge and Pisani [61]	Rigid ellipse body	No	Single cylinder
Shao et al. [62]	Wavy foil	No	Single D-section cylinder
Park et al. [64]	Flexible fin	Yes	Single cylinder
Li et al. [65]	Kármán gaiting model	No	Single D-section cylinder
Wang et al. [18]	Plate	Yes	Two tandem cylinders
Tong et al. [66]	Kármán gaiting model	No	Single cylinder
Wu et al. [16]	Kármán gaiting model	No	Single cylinder
Tang et al. [79]	Wavy foil	No	Single D-section cylinder
Wang et al. [80]	Wavy foil	No	Single D-section cylinder

In summary, numerous studies have been performed on different aspects related to fish swimming. The research areas of fish swimming are broad, including studies on swimming motion, swimming performance, fish schooling and fish refuging. Our research focus is investigating fish refuging by means of numerical simulation of the fish swimming downstream of two cylinders. Despite several studies being conducted on a swimmer behind two tandem cylinders, the self-propelled fish-like model with well-defined swimming motion behind different cylinder arrangements is rarely study. Therefore, it is necessary to conduct study to overcome the deficiencies and close the research gaps.

## 1.3. Research Aim and Objectives

Despite numerous research have been conducted about fish swimming, few studies focus on the interaction between the swimming fish and multiple cylinders in different arrangements. This research aims to improve the understanding of self-propelled fish swimming behind multiple cylinders. While both experiment and numerical simulation are possible means for solving the fluid-structure interaction problem, experiment would be challenging as it is difficult to control the swimming path of a live fish and acquire its interaction with cylinders with limited equipment and resources. Therefore, numerical simulation would be employed for this research. Through the study, we aim to address the following research questions:

- 1) What are key parameters affecting the interaction between swimming fish and a stationary cylinder? How do the parameters affect swimming performance?
- 2) How is the interaction between swimming fish and a stationary cylinder?
- 3) How do cylinder arrangements affect fish swimming?

The objectives to be addressed in this research are as follows:

- a) To conduct parametric studies on undulation without translational and rotational motion behind a single cylinder to reveal the effect of different parameters on fish swimming.
- b) To conduct parametric studies on self-propelled swimming behind a single cylinder to reveal the effect of different parameters on fish swimming.
- c) To conduct studies on free swimming behind two different cylinder arrangements.

## 1.4. Organization of Thesis

The thesis is composed of seven chapters. The remaining chapter are organized as follows:

Chapter 2 will describe the problem in the present study and introduce the methodology employed. The physical model of the swimmer alongside its kinematics, governing equations are presented. The numerical method employed in the research would be introduced together with the validation.

In Chapter 3, fish undulation without translational and rotational motion behind a single cylinder is studied. The effect of parameters, such as free-stream velocity, streamwise and crossflow distances from the cylinder and diameter of the cylinder are examined.

Chapter 4 will explore fish undulation with only rotational motion behind a single cylinder. Effects of streamwise and crossflow distances on swimming performance are studied.

In Chapter 5, we will go further by achieving self-propulsion behind a single cylinder. Effects of streamwise and crossflow distances on swimming performance are investigated.

Chapter 6 will examine free swimming behind two cylinders. Two arrangements of cylinders will be investigated and the distribution of motion modes among different cylinder-cylinder distances and cylinder-fish distance are assessed.

Chapter 7 will conclude all the studies performed in this research. Directions will also be given for future work.

## **Chapter 2 Problem Description and Methodology**

This chapter covers the problem description and the methodology of this research. Both the swimmer and the environment are the two most fundamental elements in this fluid-structure interaction (FSI) problem. Therefore, the physical model of the swimmer alongside its kinematics is presented first, followed by the introduction of governing equations and essential parameters. Then, the numerical method employed in this research would be covered. The computation domain used in the numerical simulation is described together with the relevant boundary conditions. Finally, the validation on the numerical method is included to conclude this chapter.

## 2.1. Problem Description

#### 2.1.1. Physical Model and Kinematics

In order to investigate the physics of fish swimming, a two-dimensional (2D) airfoil is defined as the fish body model. The airfoil employed is NACA0012, a symmetric foil model whose maximum thickness is 12% of its chord length. A body and caudal fin (BCF) swimming mode is adopted in the research. The midline lateral displacement in local coordinate system is described by Kern and Koumoutsakos [55] as below:

$$y(x,t) = A_{max} \frac{x/L + 0.03125}{1.03125} \sin\left[2\pi \left(\frac{x}{L} - \frac{t}{T_p}\right)\right] \qquad (0 \le x \le 1)$$
 (2.1)

where x is the projection of midline along the fish model on the x-axis, y is the lateral displacement of the midline, L is the projected fish length on the x-axis, as shown in Figure 2-1  $A_{max}$  is the maximum tail-beat amplitude and  $T_P$  is the tail-beat period of the fish.  $A_{max} = 0.125L$  at the tail of the fish according to the amplitude envelope in Figure 2-2.

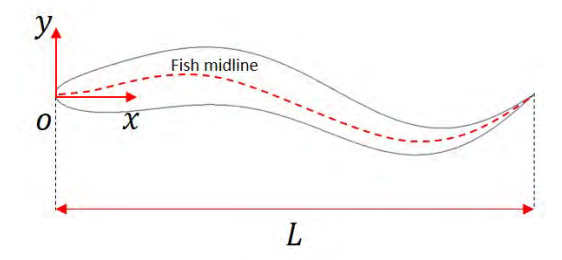


Figure 2-1 Illustration of the fish model

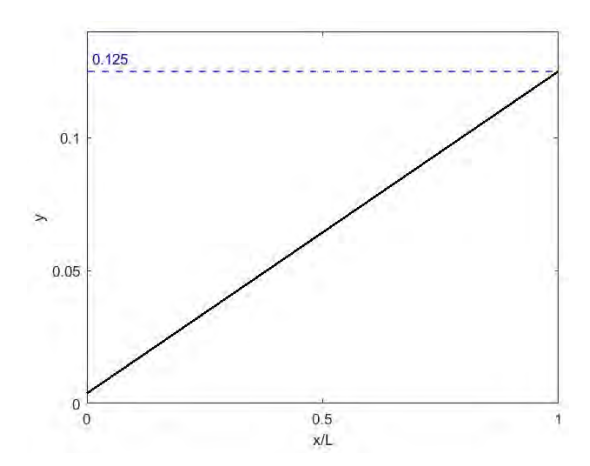


Figure 2-2 Amplitude envelope profile of the fish.

### 2.1.2. Governing Equations

The governing equations are nondimenionalized with respect to reference quantities. In the present work, fish body length L and reference velocity, defined as  $U_{ref} = L/T_P$ , are chosen to be the reference quantities.  $T_P$  is defined as the tail-beat period of the fish with  $T_P = 1/f_{un}$ , in which  $f_{un}$  is the tail-beat or undulating frequency of the fish.

The fish model is immersed in a viscous incompressible fluid. Therefore, the fluid part is governed by the continuity and two-dimensional incompressible Navier-Stokes equations. The nondimensional equations are as follows:

$$\nabla \cdot \boldsymbol{v} = 0, \tag{2.2}$$

$$\frac{\partial \mathbf{v}}{\partial t} + \mathbf{v} \cdot \nabla \mathbf{v} = -\frac{1}{\rho} \nabla p + \nu \nabla^2 \mathbf{v} + f_b, \tag{2.3}$$

where v is velocity, p is pressure,  $\rho$  is density of the fluid,  $\nu$  is the fluid kinematic viscosity and  $f_b$  is external force exerted on the fluid flow.

#### 2.1.3. Parameters

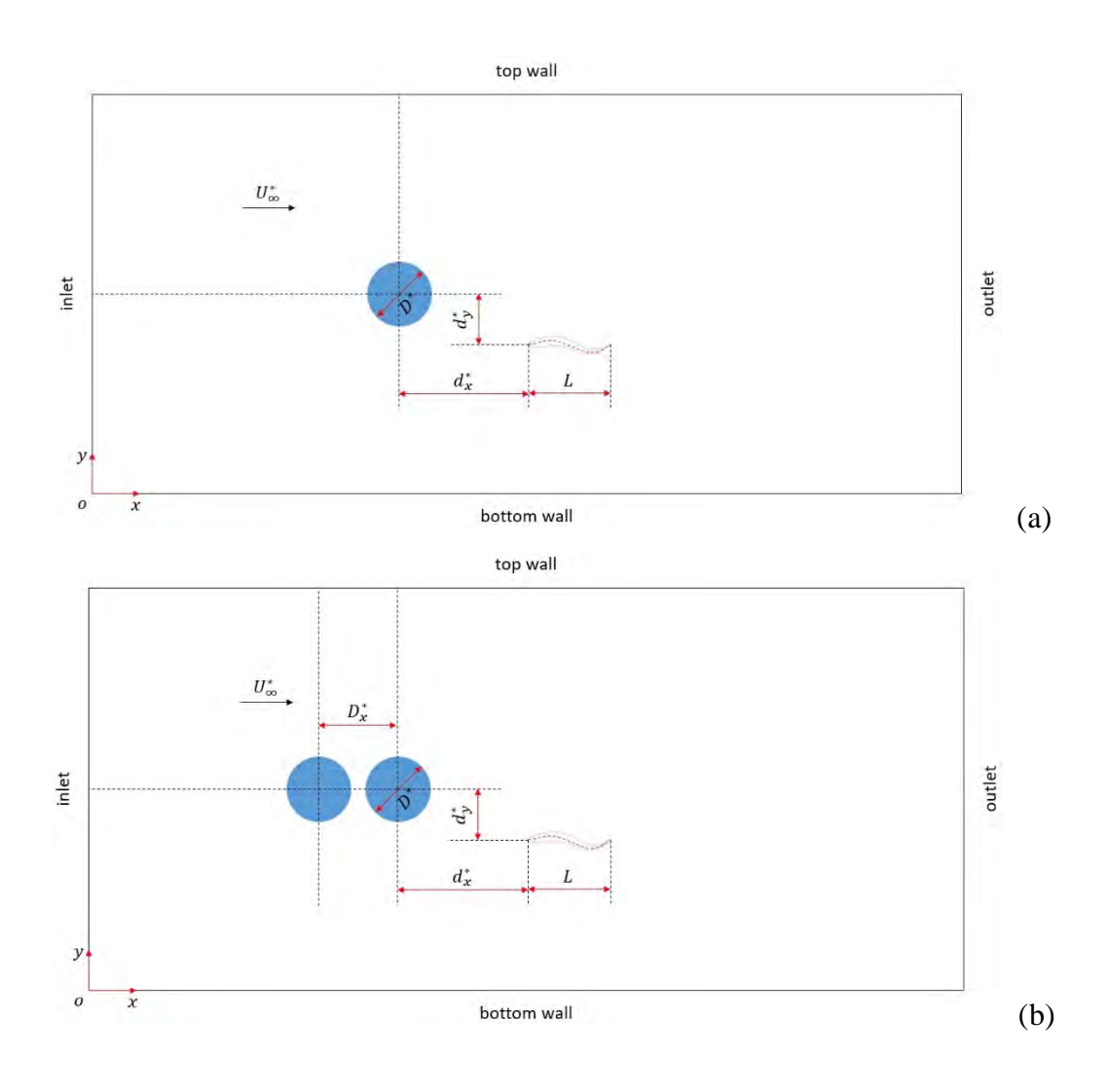
For ease of reference, definitions of all controlling parameters are given in Table 2.1. The interactions of the fish model with the cylinder(s) are mainly affected by dimensionless parameters, including Reynolds number (Re), free-stream velocity  $(U_{\infty}^*)$ , diameter of the cylinder  $(D^*)$ , longitudinal distance between the fish model and the cylinder(s)  $(d_x^*)$ , lateral distance between the fish model and the cylinder(s)  $(d_y^*)$ , longitudinal distance between two cylinders in the tandem arrangement  $(D_x^*)$  and lateral distance between two cylinders in the side-by-side arrangement  $(D_y^*)$ .

Table 2.1 Definitions of controlled parameters in the study

Parameter	Definition
Cylinder diameter	$D^* = D/L$
Streamwise distance between fish & cylinder(s)	$d_{x}^{*}=d_{x}/L$
Crossflow distance between fish & cylinder(s)	$d_{\mathcal{Y}}^* = d_{\mathcal{Y}}/L$
Streamwise distance between cylinders	$D_x^* = D_x/L$
Crossflow distance between cylinders	$D_{\mathcal{Y}}^* = D_{\mathcal{Y}}/L$
Reynolds number	$Re_{fish} = V_{max}L/\nu$
(fish undulatory velocity)	
Reynolds number	$Re_{\infty} = U_{\infty}L/\nu$
(free-stream flow)	
Time	$t^* = t/T_P = tU_{ref}/L$
Free-stream velocity	$U_{\infty}^* = U_{\infty}/U_{ref}$

In this research, scenarios with single and multiple cylinders with different arrangements are studied. According to different arrangement of cylinders, the fish model is placed differently. For the scenario of a single cylinder, the "nose" of the fish model is located at a streamwise distance  $(d_x^*)$  and a crossflow distance  $(d_y^*)$  from the centre of the cylinder, as shown in Figure 2-3(a). For two cylinders in the tandem arrangement, the "nose" of the fish model is located at a streamwise

distance  $(d_x^*)$  and a crossflow distance  $(d_y^*)$  from the centre of the downstream cylinder as shown in Figure 3(b). The two tandem cylinders are separated from each other by the streamwise distance  $(D_x^*)$ . For two cylinders in the side-by-side arrangement, the "nose" of the fish model is located at a streamwise distance  $(d_x^*)$  and a crossflow distance  $(d_y^*)$  from the straight line joining the centres of two cylinders, as shown in Figure 3(c). the two side-by-side cylinders are separated from each other by crossflow distance  $(D_y^*)$ .



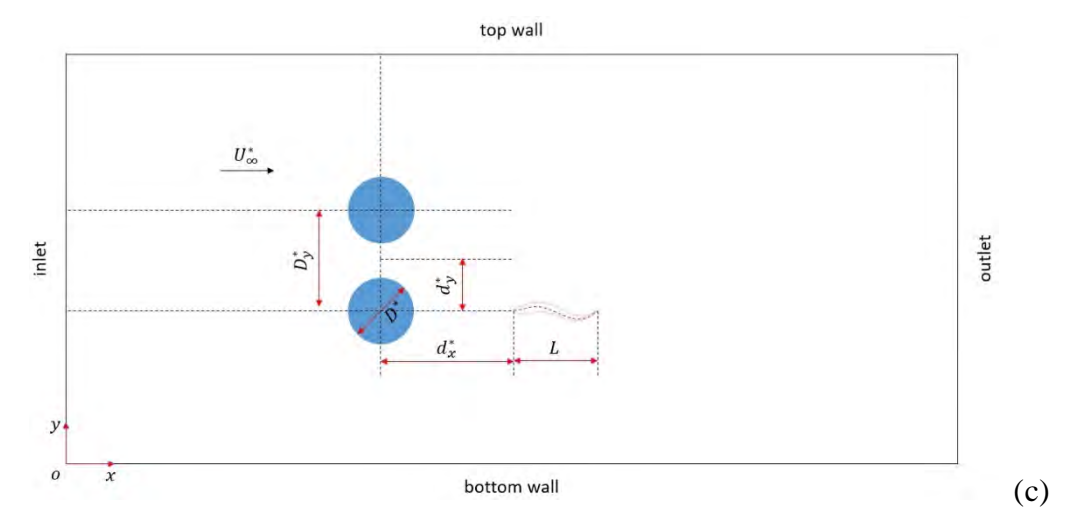


Figure 2-3(a) Schematic of the fish model with a single cylinder, (b) Schematic of the fish model with two cylinders in the tandem arrangement, (c) Schematic of the fish model with two cylinders in the side-by-side arrangement.

In addition, definitions of the performance parameters are given as below in details, including Reynolds number (Re), Strouhal number (St), longitudinal force ( $F_x$ ), lateral force ( $F_y$ ), power (P), drag coefficient ( $C_D$ ), lift coefficient ( $C_D$ ) and power coefficient ( $C_D$ ).

Reynolds number (Re) is a dimensionless number measuring the ratio of the inertial force to viscous force. In this study, two Re are defined with respect to two different velocities.  $Re_{fish}$  is based on the fish maximum undulatory velocity  $V_{max}$  while  $Re_{\infty}$  is based on the free-stream velocity  $U_{\infty}$ .

$$Re_{fish} = \frac{V_{max}L}{v} \tag{2.4}$$

$$Re_{\infty} = \frac{U_{\infty}L}{v} \tag{2.5}$$

where  $V_{max} = 2\pi A_{max} f$  is the maximum undulatory velocity and  $U_{\infty}$  is the free-stream velocity.

Two *Re* could be applied on the fish and converted to one another through the relationship as follows:

$$Re_{fish} = \frac{V_{max}L}{v}$$

$$= \frac{2\pi A_{max}fL}{v}$$

$$= \frac{\pi}{4\lambda}Re_{\infty}$$
(2.6)

where  $\lambda = U_{\infty}/U_{ref}$  is the ratio between reference velocity and free-stream velocity.  $Re_{\infty}$  could be applied to the cylinder with expression of diameter of the cylinder in terms of fish body length L.

St is a dimensionless number describing the phenomenon of oscillating flow. In our study, it is defined as follows:

$$St = \frac{f_{vor}D}{U_{\infty}}$$

$$= \frac{f_{vor}(\alpha L)}{\lambda U_{ref}}$$

$$= \frac{\alpha f_{vor}}{\lambda} \cdot \frac{L}{U_{ref}}$$

$$= \frac{\alpha f_{vor}T_{P}}{\lambda}$$

$$= \frac{\alpha}{\lambda} \cdot \frac{f_{vor}}{f}$$
(2.7)

where  $\alpha = D/L$  is the ratio of the diameter of the cylinder to the fish body length,  $f_{vor}$  is the vortex shedding frequency from the cylinder.

Longitudinal force and lateral force on the fish are forces acting along fish body boundary in the streamwise and crossflow directions respectively. Power on the fish is the energy expenditure or extraction on the fish body from the fluid per unit time. They are defined as follows:

$$F_{x} = \int_{L} F_{f,x} ds, \qquad F_{x} = \int_{L} F_{f,y} ds, \qquad P = \int_{L} \mathbf{F}_{f} \cdot \mathbf{v} ds$$
 (2.8)

where  $\mathbf{F}_f = (F_{f,x}, F_{f,y})$  is the fluid force per unit arc length acting on the fish,  $\mathbf{v}$  is the local fluid velocity at the position of the fish body boundary and ds is the unit arc length of the fish body.

Drag coefficient is a dimensionless quantity to quantify drag experienced by the fish body in the fluid while lift coefficient is a dimensionless number related to lateral force generated on the fish body in the fluid environment. Power coefficient is a dimensionless number to describe power consumption or extraction on the fish body. They are defined respectively as follows:

$$C_D = \frac{F_{\chi}}{0.5\rho U_{\infty}^2 L}, \quad C_L = \frac{F_{y}}{0.5\rho U_{\infty}^2 L}, \quad C_P = \frac{P}{0.5\rho U_{\infty}^3 L}$$
 (2.9)

Same definition for coefficients could be applied to the cylinder with the diameter of the cylinder expressed in terms of fish body length L.

## 2.2. Numerical Method

In general, there are two categories of numeral methods for fluid simulation. The first category is conventional numerical methods on the basis of discretizing equations of fluid mechanics. Examples are finite element method (FEM), finite volume method (FVM) and finite difference method (FDM). The second category is established on the foundation of microscopic or mesoscopic particles. Famous examples are molecular dynamics (MD), lattice gas model and multi-particle collision dynamics.

The fluid-structure interaction problem in this study is solved numerically by the lattice Boltzmann method coupled with the immersed boundary method (IB-LBM). The LBM employed was developed from lattice gas model aforementioned and hence under the second category of numerical methods.

#### 2.2.1. Lattice Boltzmann Method

The LBM has several advantages over other numerical methods. The first advantage is its simplicity and efficiency. The LBM allows artificial compressibility in solving the incompressible Navier-Stokes equation. It does not involve the Poisson equation which could be difficult to solve because of the non-locality [72]. The second advantage of the LBM is its suitability for complex geometry [73]. Swimmer models involve moving boundaries in which conservation of mass applied could be simulated well with the use of the LBM. The third advantage is the availability of a wide range of multiphase and multicomponent methods for the LBM [72]. Together with the second advantage in complex geometries, the LBM could be implemented well for simulation of multiphase and multicomponent flows in complex geometries.

In the aspect of fluid flow of this study, the two-dimensional incompressible Navier-Stokes equations are solved by the incompressible D2Q9 MRT LBE model [74], i.e., two-dimensional incompressible multiple relaxation time lattice Boltzmann equation model with nine discrete velocities. D2Q9 velocity set is shown in Figure 4. The model is given as below [75][74]:

$$f_{i}(\mathbf{x} + \mathbf{c}_{i}\Delta t, t + \Delta t) - f_{i}(\mathbf{x}, t)$$

$$= -\mathbf{M}^{-1}\mathbf{S}\mathbf{M} [f_{i}(\mathbf{x}, t) - f_{i}^{eq}(\mathbf{x}, t)] - \mathbf{M}^{-1}(I - \mathbf{S}/2)\mathbf{M}g_{i}(\mathbf{x}, t)\Delta t$$
(2.10)

where  $f_i$  is the distribution function with subscript i referring to one of a small discrete set of velocities  $\{c_i\}$ , x is the Eulerian coordinate,  $c_i$  is the lattice velocity,  $\Delta t$  is time step, M is the transformation matrix, S is the non-negative diagonal relaxation matrix consisting of different relaxation rates, I is the identity matrix and  $f_i^{eq}$  is local equilibrium distribution function.

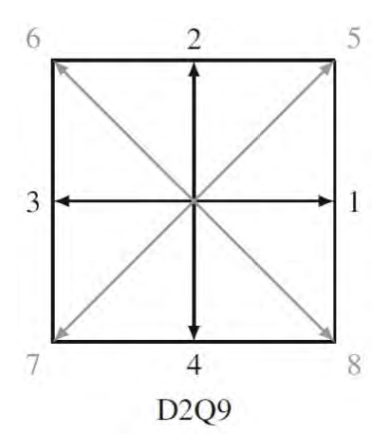


Figure 2-4 D2Q9 velocity set.

 $f_i^{eq}$  can be written as:

$$f_i^{eq} = w_i \left[ \rho_f + \rho_{f0} \left( \frac{\boldsymbol{c}_i \cdot \boldsymbol{v}}{c_s^2} + \frac{(\boldsymbol{c}_i \cdot \boldsymbol{v})^2}{2c_s^4} - \frac{\boldsymbol{v}^2}{2c_s^2} \right) \right]$$
 (2.11)

where  $w_i$  is the weighting factor,  $\rho_f$  is the fluid density,  $\rho_{f0}$  is the average fluid density,  $\boldsymbol{v}$  is fluid velocity and  $c_s$  is fluid's sound speed.

The fluid velocity v and fluid density  $\rho_f$  could be expressed in terms of distribution function  $f_i$  and lattice velocity  $c_i$  as follows:

$$\rho_{f0} \mathbf{v} = \sum_{i} c_i f_i \tag{2.12}$$

$$\rho_f = \sum_i f_i \tag{2.13}$$

In equation (2.4),  $g_i$  is discrete force distribution function which can be expressed as [75]:

$$g_i = w_i \left( \frac{\boldsymbol{c}_i - \boldsymbol{v}}{c_s^2} + \frac{\boldsymbol{c}_i \cdot \boldsymbol{v}}{c_s^4} \boldsymbol{c}_i \right) f_b \tag{2.14}$$

where  $f_b$  is the external force in equation (2.3).

#### 2.2.2. Immersed Boundary Method

To establish the linkage between the fluid flow and the dynamics of the swimmer, the immersed boundary method (IBM), first proposed by Peskin [76], is employed. It has the advantage of directly known boundary in which shape of the boundary and relevant intersection points do not have to be reconstructed. The IBM could cope with the deformable and movable boundary, i.e. fish body, ensure no-slip boundary condition is imposed and compute the fluid force acted on the boundary of structure. It can be incorporated with any Navier-Stokes solver which supports external forcing, like the LBM.

The basis of the IBM is an Eulerian and Lagrangian system mathematically. The Eulerian grid is represented by a fixed and stationary grid on the flow field in which the Navier-Stokes equations are being solved. It is defined by the LBM lattice nodes. The Lagrangian points are arbitrarily distributed on the boundary of the structure, i.e. fish body in our research. They are not bound to the Eulerian grid and able to move freely in space.

The discretized IBM formulas suggested by Kang [75] are adopted in this study and expressed as follows:

$$\mathbf{v}_b = \sum \mathbf{v} \delta(\mathbf{x} - \mathbf{X}) \Delta x^2 \tag{2.15}$$

$$\mathbf{F}_{f} = -2\rho_{f} \frac{\frac{\partial \mathbf{X}}{\partial t} - \mathbf{v}_{b}}{\Delta t} \tag{2.16}$$

$$\mathbf{f}_b = -\sum \mathbf{F}_f \delta(\mathbf{x} - \mathbf{X}) \Delta s \tag{2.17}$$

where  $v_b$  is the unforced velocity of swimmer structure interpolated from velocity v of surrounding flow through the discrete delta function  $\delta$ ,  $F_f$  is fluid force acting on the swimmer related to the difference between actual velocity  $\partial X/\partial t$  of the swimmer and its unforced velocity

 $v_b$ ,  $f_b$  is external force calculated from the fluid force  $F_f$  through delta function  $\delta$ , X is swimmer position,  $\Delta x$  and  $\Delta s$  are mesh spacing for computational fluid and solid domains respectively.

### 2.2.3. Computation Domain

A rectangular computational domain is chosen for the study, as shown in Figure 2-5. The dimensions are  $[0L, 48L] \times [0L, 16L]$  in x and y directions respectively. The origin is chosen as the left bottom corner of the computational domain. The fish-like swimming foil is placed downstream of the cylinder(s). To save computational resources and time, the computation domain is divided into areas with different mesh resolutions. Blocks with finer mesh are employed in the vicinity of the swimming foil and the cylinder(s) while blocks with coarser mesh are applied far from the centre.

#### 2.2.4. Boundary Conditions

The periodic boundary condition is imposed at the top and bottom boundaries. The characteristic non-reflecting boundary condition is implemented at the inlet, whereas the Neumann boundary condition is set at the outlet as shown in Figure 2-5. The initial fluid velocity field is  $\mathbf{v} = (U, 0)$  in the entire computational domain with random initialization.

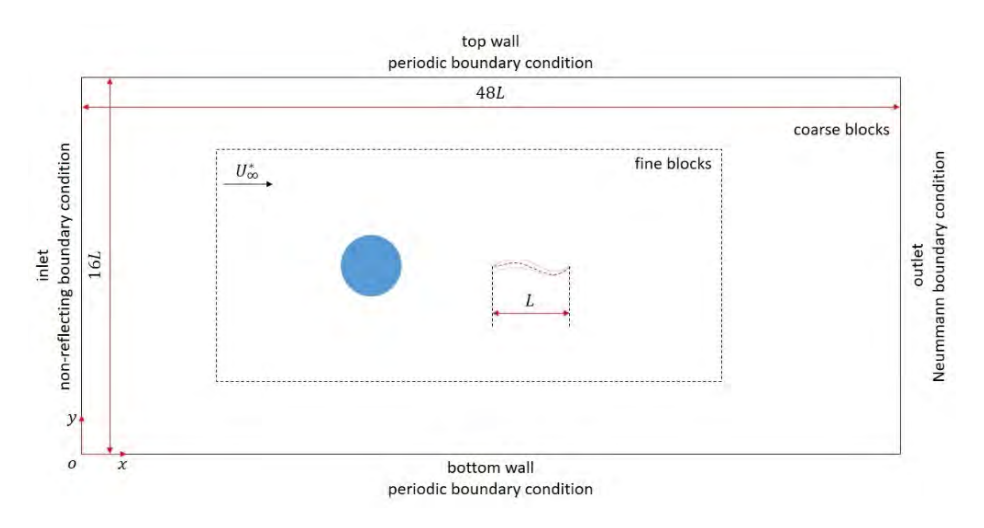
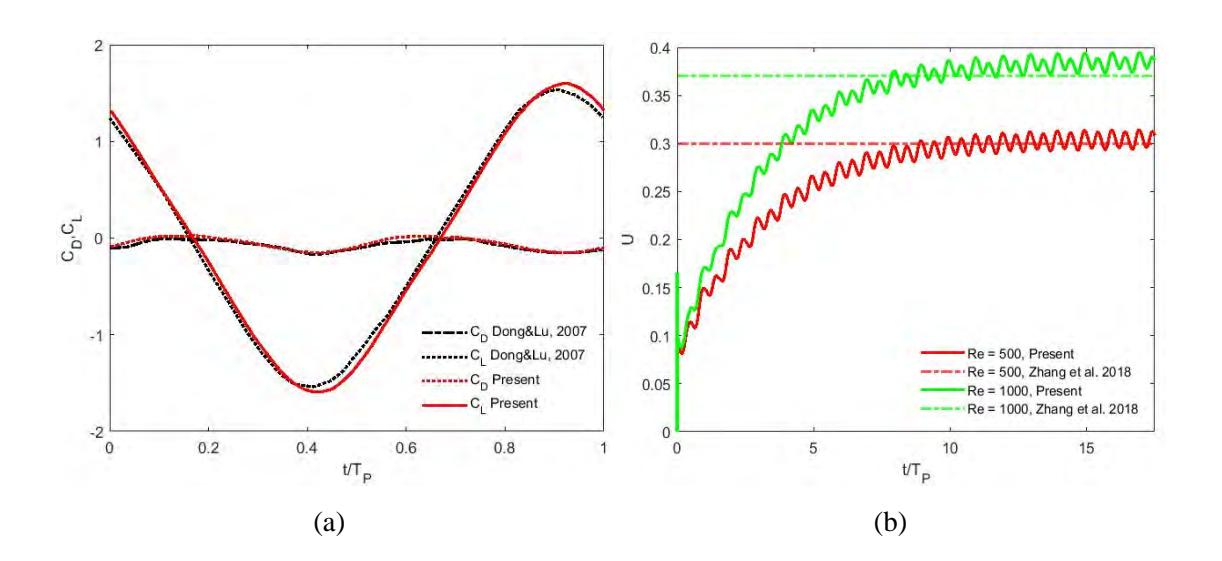


Figure 2-5 Schematic of the computational domain.

#### 2.2.5. Numerical Validation

An in-house numerical solver, with reference to the aforementioned numerical method, has been developed for the study. To verify the accuracy of the solver, three simulation cases are performed. In the first case, the fluid flow over a single traveling wavy foil at  $Re_U = 5000$  has been simulated. Figure 2-6(a) shows the time-dependent lift and drag coefficient of the wavy foil. It is clear that both lift and drag coefficients agree well with those presented by Dong and Lu [39]. In the second case, a single self-propelled undulatory foil has been simulated. From Figure 2-6(b), it shows that the propulsive velocities in cases Re = 500 and 1000 follow with those results by Zhang et al. [77] reasonably. For the third case, the collective motions of two undulatory self-propelled foils in tandem at Re = 2000 have been simulated. The gap spacings between the foils G for frequency ratios between two foils, Fr = 1.0 and 1.7, are compared with the results obtained by Yu et al. [78] and shown in Figure 2-6(c).



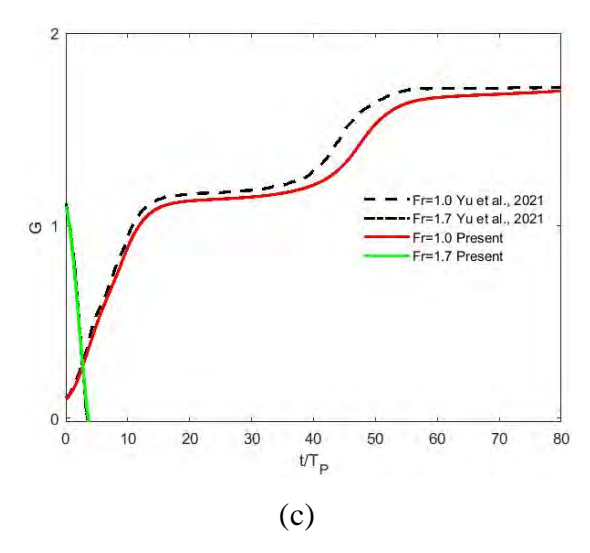


Figure 2-6 Validation results for cases: (a)  $C_D \& C_L$  of a single traveling wavy foil at  $Re_U = 5000$ , (b) propulsive velocities of a self-propelled undulatory foil at Re = 500 & 1000 and (c) gap spacing between two foils G for frequency ratios Fr = 1.0 and 1.7.

#### 2.2.6. Grid and Time Step Convergence Tests

Grid and time step sensitivity studies are conducted to guarantee the accuracy and independence of results generated. Since both configurations with single and multiple cylinders would be studied, two resolution tests are conducted. For the test on a single cylinder, the configuration is set according to Figure 2-3(a). For the test on multiple cylinders, the configuration as shown in Figure 2-3(b) is applied. The fish in both tests undulates as prescribed by equation (2.1) with the "nose" fixed at the chosen position (i.e.  $d_x^* \& d_y^*$ ). The parameters of both resolution tests are summarized in Table 2.2. Drag and lift coefficients of the fish are two performance parameters employed as the indicators of the grid and time step sensitivity studies. Three test cases are conducted for each configuration for the resolution tests as listed in Table 2.3.

Table 2.2 Definitions and values of relevant parameters for the resolution test

Parameter	Definition	Value
Cylinder diameter	$D^* = D/L$	1
Streamwise distance	$d_x^* = d_x/L$	4
Crossflow distance	$d_y^* = d_y/L$	0
Reynolds number	$Re_{fish} = V_{max}L/\nu$	40
(fish undulatory velocity)		
Reynolds number	$Re_{\infty} = U_{\infty}L/\nu$	127.3
(free-stream flow)		
Free-stream velocity	$U_{\infty}^{*}=U_{\infty}/U_{ref}$	2.5
(For multiple cylinders only)		
Streamwise distance between cylinders	$D_x^* = D_x/L$	1.2

Table 2.3 Types of test case for the resolution test

Type	Grid size	Time step size
Coarse	L/64	1/1600
Medium	L/128	1/6400
Fine	L/256	1/25600

It could be observed in Figure 2-7 and 2-8 that three curves in graphs of drag and lift coefficients resemble each other. A small but negligible deviation is observed between coarse and fine meshes. Therefore, medium mesh is adopted as a compromise to save computational time and resources.

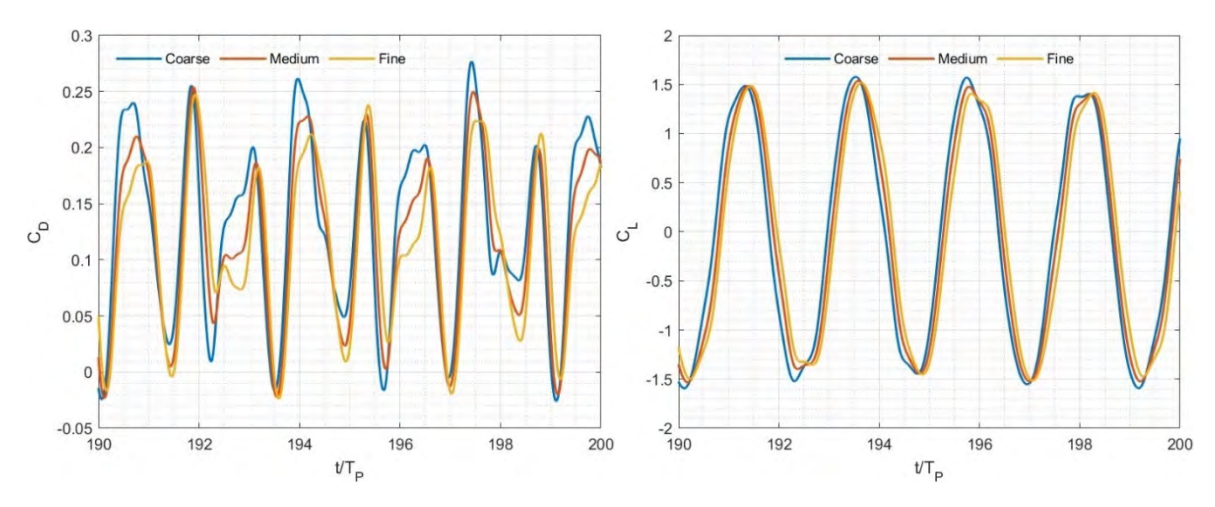


Figure 2-7 Time histories of drag coefficient  $C_D$  (left) and lift coefficient  $C_L$  (right) of the fish behind the single cylinder with three different types of mesh employed.

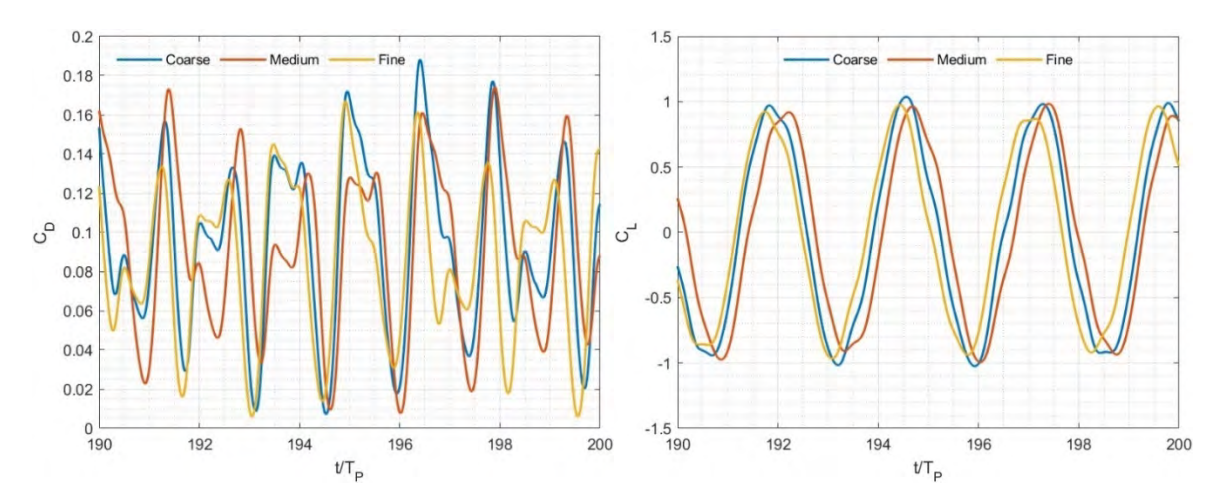


Figure 2-8 Time histories of drag coefficient  $C_D$  (left) and lift coefficient  $C_L$  (right) of the fish behind two tandem cylinders with three different types of mesh employed.

## 2.3. Remarks

This chapter presents the framework employed to solve the FSI problem in the present study. For the structure part, NACA0012 airfoil is adopted as the fish body model with its kinematics prescribed as the function of midline lateral displacement. Continuity equation and two-dimensional incompressible Navier-Stokes (NS) equation are two governing equations for the fluid part. D2Q9 MRT LBE model is employed to solve the NS equation. Finally, IBM is introduced for the interaction between fluid and structure parts. Computation domain is briefly described with the numerical solver validated. Grid and test step convergence tests are also conducted.

# Chapter 3 Undulation of fixed body behind Single Cylinder

To our best of our knowledge, there is not any detailed study on the self-propelled swimmer behind multiple cylinders. Most studies focus on either a stationary hydrofoil or an undulating fish model behind a single cylinder. This motivates the research study to explore the physics and performance of the self-propelled swimmer behind multiple cylinders. To begin with, it is essential to have a fundamental understanding of the interaction between the swimmer and the single cylinder.

To understand the interaction between the swimmer and the single cylinder progressively, the most basic mode of motion is studied in the first instance. In this chapter, the fish is undulating at a fixed position behind a single cylinder without any translational and rotational motion. Effects of different controlling parameters on the swimming performance are examined.

As depicted in Figure 2-3(a), the "nose" of the fish model is fixed at a chosen position (i.e.  $d_x^* \& d_y^*$ ) with the body undulating as prescribed by equation (2.1). The fish model is not allowed to rotate nor translate. For ease of discussion, all relevant parameters with adopted values are listed in Table 3.1.  $Re_{fish}$  is chosen to be 40 to keep  $Re_{\infty}$  converted as described in equation (2.6) less than 500, owing to complexity imposed on the in-house numerical solver. To explore the effect of different parameters, a baseline value is assigned to each parameter, i.e.,  $D^* = 1$ ,  $d_x^* = 4$ ,  $d_y^* = 0$  and  $U_{\infty}^* = 5$ .

Table 3.1 Definitions and chosen values of relevant parameters in Chapter 3

Parameter	Definition	Values <sup>a,b</sup>
Cylinder diameter	$D^* = D/L$	1, 2, 3, 4, 5, 6, 7
Streamwise distance	$d_x^* = d_x/L$	1, 2, 3, <b>4</b>
Crossflow distance	$d_y^* = d_y/L$	<b>0</b> , 1, 2, 3, 4
Reynolds number	$Re_{fish} = V_{max}L/\nu$	40
(fish undulatory velocity)		
Reynolds number	$Re_{\infty} = U_{\infty}L/\nu$	-
(free-stream flow)		
Strouhal number	$St = f_{vor} D/U_{\infty}$	-
Time	$t^* = t/T_P = tU_{ref}/L$	-
Free-stream velocity	$U_{\infty}^* = U_{\infty}/U_{ref}$	2.5, <b>5</b> , 7.5

<sup>&</sup>lt;sup>a</sup> The symbol '-' indicates that the parameters change according to different cases or are updated during the simulation.

# 3.1. Effect of Free-Stream Velocity

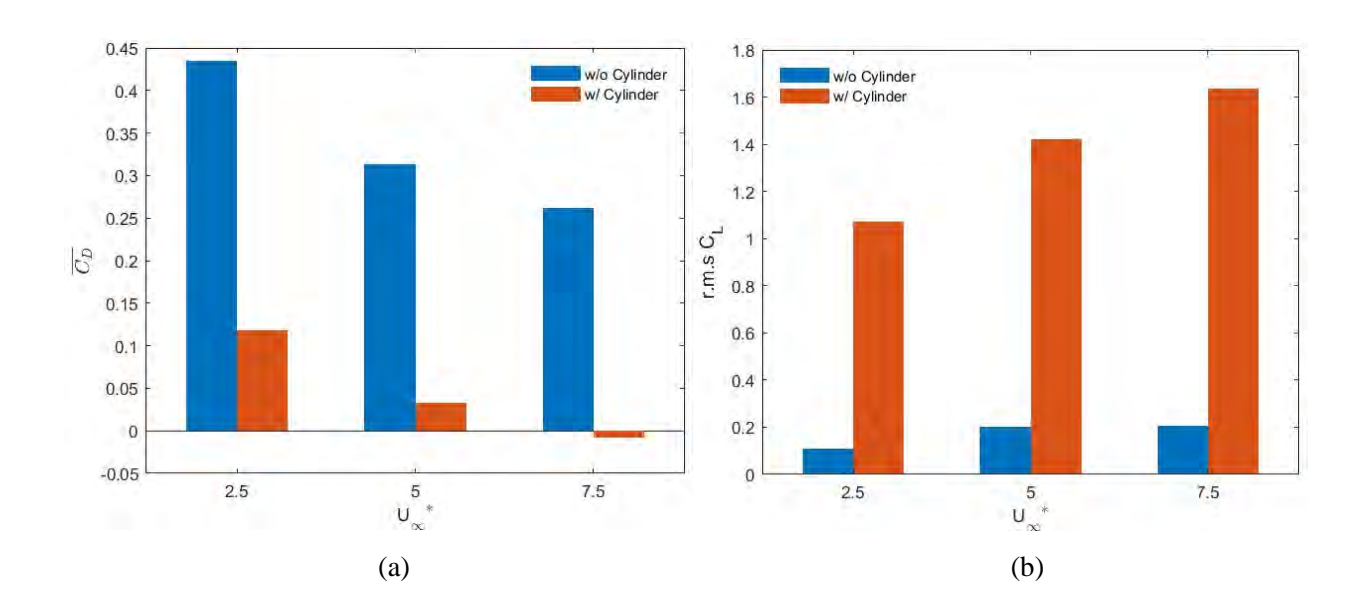
To explore the effect of free-stream velocity  $(U_{\infty}^*)$ , other parameters are set to their baseline values, i.e.  $D^* = 1$ ,  $d_x^* = 4$  and  $d_y^* = 0$ . Three velocities,  $U_{\infty}^* = 2.5$ , 5 and 7.5, are examined in the study. Figure 3-1 shows the time-averaged drag coefficient  $(\overline{C_D})$ , root-mean squared lift coefficient  $(C_{L\,rms})$  and time-averaged power coefficient  $(\overline{C_P})$  of the fish with respect to different  $U_{\infty}^*$ . The comparison of such coefficients with or without the presence of the cylinder is also presented for easy reference.

As shown in Figure 3-1(a),  $\overline{C_D}$  decreases when  $U_{\infty}^*$  increases no matter whether the cylinder is present or not. With the cylinder placed upstream of the fish,  $\overline{C_D}$  decreases significantly for each case of  $U_{\infty}^*$  (i.e. drops from 0.43 to 0.12 for  $U_{\infty}^*=2.5$ ).  $\overline{C_D}$  even achieves a small negative value (i.e. -0.01) for the case of  $U_{\infty}^*=7.5$ . That indicates a small amount of thrust generated when the cylinder is present. The drag reduction or small thrust generation is believed to be contributed by the recirculation flow behind the cylinder.

<sup>&</sup>lt;sup>b</sup> The bold values are used as baseline parameters.

However, the results for  $C_{L\,rms}$  are totally different from those for  $\overline{C_D}$ . In Figure 3-1(b),  $C_{L\,rms}$  increases with  $U_{\infty}^*$  for both scenarios with and without cylinder. For cases of  $U_{\infty}^* = 2.5$ , 5 and 7.5 without the presence of the cylinder,  $C_{L\,rms}$  is around 0.1 to 0.2. It increases dramatically when the cylinder is placed upstream of the fish. We could observe that vortices shed from the cylinder interact largely with the fish as shown in Figure 3-2. As the fish model is fixed at the "nose" and the body is allowed for undulation only, vortices induce a large lateral force on it, thus creating a large  $C_{L\,rms}$ .

The results for  $\overline{C_P}$  are categorized in four groups, based on power consumption or extraction and with or without the presence of the cylinder. Overall, values of  $\overline{C_P}$  drop with the increase of  $U_{\infty}^*$ . As depicted in Figure 3-1(c), the values of power consumption by the fish undulating downstream of the cylinder are much larger than those without the cylinder for all cases of  $U_{\infty}^*$ . The largest power consumption by the fish occurs for  $U_{\infty}^* = 2.5$ . The same occurs for the power extraction by the fish. For  $U_{\infty}^* = 5$  and 7.5, power consumption and extraction have similar values with the presence of the cylinder. The large values of power consumption and extraction are believed to be caused by the large lateral force created in the vortex interaction.



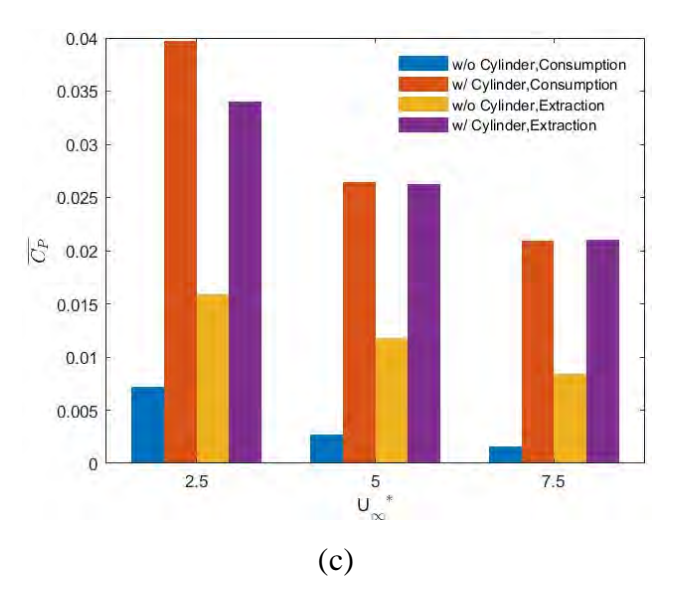


Figure 3-1 Performance parameters for free-stream velocities  $U_{\infty}^* = 2.5$ , 5 and 7.5 with and without the presence of the cylinder: (a) time-averaged drag coefficient ( $\overline{C_D}$ ), (b) root-mean squared lift coefficient ( $\overline{C_L}_{rms}$ ) and (c) time-averaged power coefficient ( $\overline{C_P}$ ) of the fish.

As the performance of fish swimming is closely related to the behaviour of fish undulation and its interaction with vortex shed from the cylinder, the flow structure around the fish and the cylinder is explored. Figure 3-2 displays the vorticity contours of vortical flow from the cylinder passing through the fish body for  $U_{\infty}^* = 2.5$ , 5 and 7.5. We can see that vortex sheds from the cylinder, passes through the undulating fish downstream and finally forms a vortex street downstream of the fish. The vortex street dissipates quickly behind the undulating fish for  $U_{\infty}^* = 2.5$  shown in Figure 3-2(a) due to relatively larger viscous effect at lower  $Re_{\infty}$ . When  $U_{\infty}^*$  increases,  $Re_{\infty}$  increases, viscous effect becomes less dominant. The faster fluid flow enhances the interaction between vortex shed from the cylinder and the undulating fish body. Therefore, relatively unstable flow structure could be observed downstream of the fish for  $U_{\infty}^* = 5$  and 7.5 [see Figure 3-2(b) and (c)].

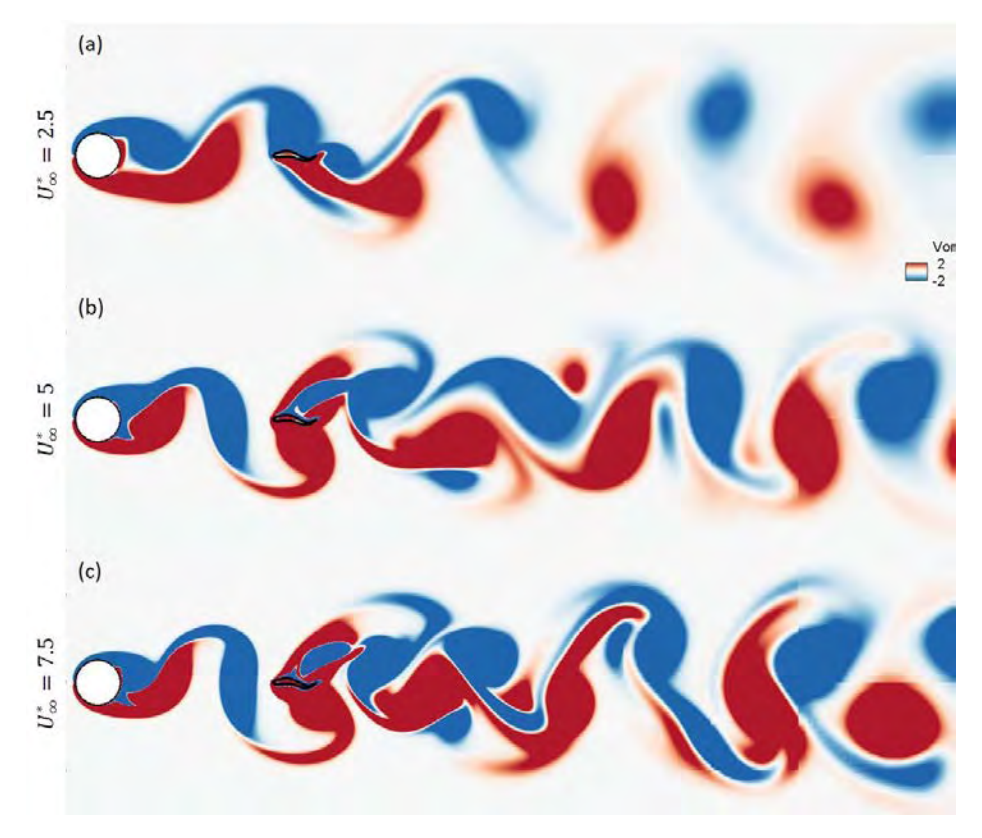


Figure 3-2 Vorticity contours of fluid flow across the cylinder passing through the fish body with different free-stream velocities: (a)  $U_{\infty}^* = 2.5$ ,  $U_{\infty}^* = 5$  and  $U_{\infty}^* = 7.5$ .

Vorticity, pressure contours and force diagrams at certain remarkable instants are presented alongside graphs of performance parameters to reveal the physics and phenomena behind. The study on flow structure reveals several common features for moments of the smallest and the largest drag force and lateral force on the fish body respectively under different  $U_{\infty}^*$ . Figure 3-3 shows the instantaneous velocity field overlaid on vorticity contours, drag  $(C_D)$  and lift  $(C_L)$  coefficients for  $U_{\infty}^* = 2.5$ , 5 and 7.5 when the fish body experiences the smallest drag force (i.e. the lowest  $C_D$ ) as shown in Figure 3-3(b1-b3). At the same time, the largest lateral force is experienced by the fish body [see Figure 3-3(c1-c3)] for the largest magnitude of  $C_L$ . In Figure 3-3(a1-a3), the fish body is similar to "S" shape, in which the anterior and posterior parts of the body are curved in the opposite direction. It is observed that a pair of vortices occurs at the posterior part of the fish for all three cases of  $U_{\infty}^*$ . The vortex couple exerts the force on the posterior part of the fish. The forces exerted on the fish body could be resolved into two components, longitudinally forward thrust and laterally lift force. The power coefficients of consumption and

extraction ( $|C_{Pc}| \& |C_{Pe}|$ ) alongside  $C_L$  and instantaneous velocity field for the same instants as Figure 3-3 are shown in Figure 3-4. As depicted in Figure 3-4 (b1-b3) and (c1-c3), it is discovered that  $|C_{Pc}| \& |C_{Pe}|$  are directly related to  $C_L$ , especially significant for  $U_{\infty}^* = 5 \& 7.5$ . When the magnitude of lateral force exerted on the fish body is the largest (i.e. the largest magnitude of  $C_L$ ), power coefficients also achieve their peak values.

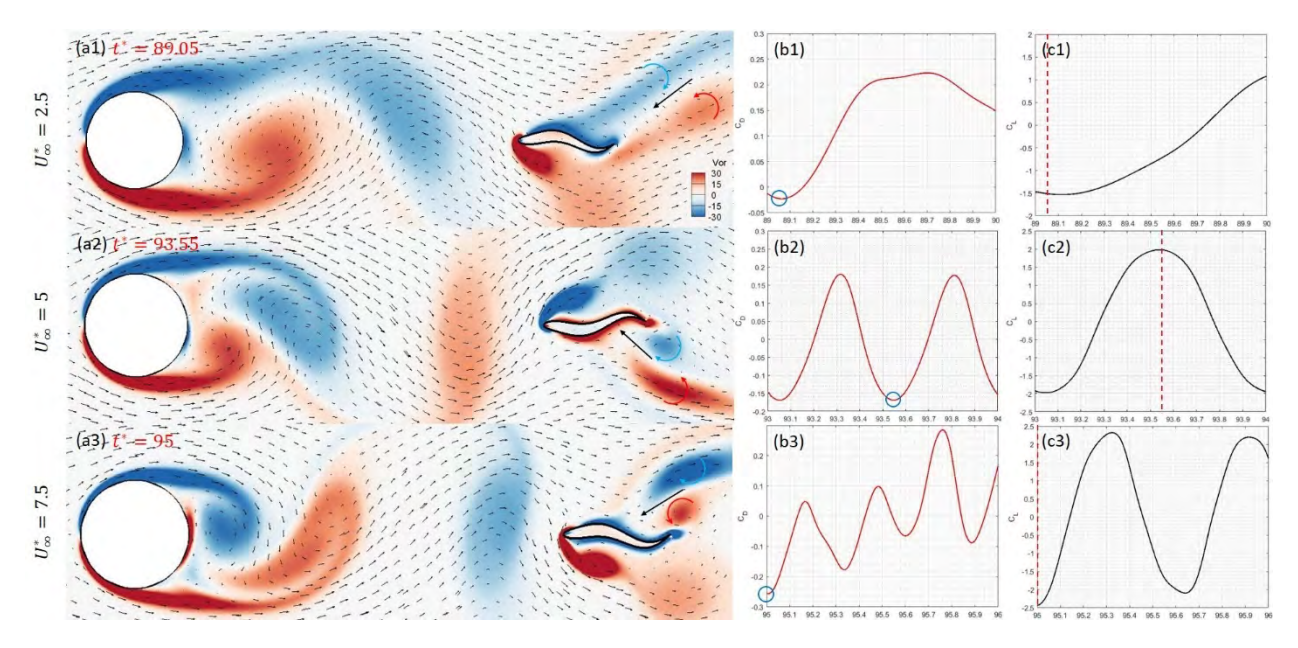


Figure 3-3 Instantaneous velocity field overlaid on vorticity contours (left), drag coefficient  $C_D$  (centre) and lift coefficient  $C_L$  (right) at the relevant time step when the fish body experiences the smallest  $C_D$  and the largest magnitude of  $C_L$  among  $U_{\infty}^* = 2.5$ , 5 and 7.5. Red represents counterclockwise vorticity while blue represents clockwise vorticity. Blue circles and red dash lines represent the corresponding smallest  $C_D$  and largest magnitude of  $C_L$  respectively at the relevant time steps.

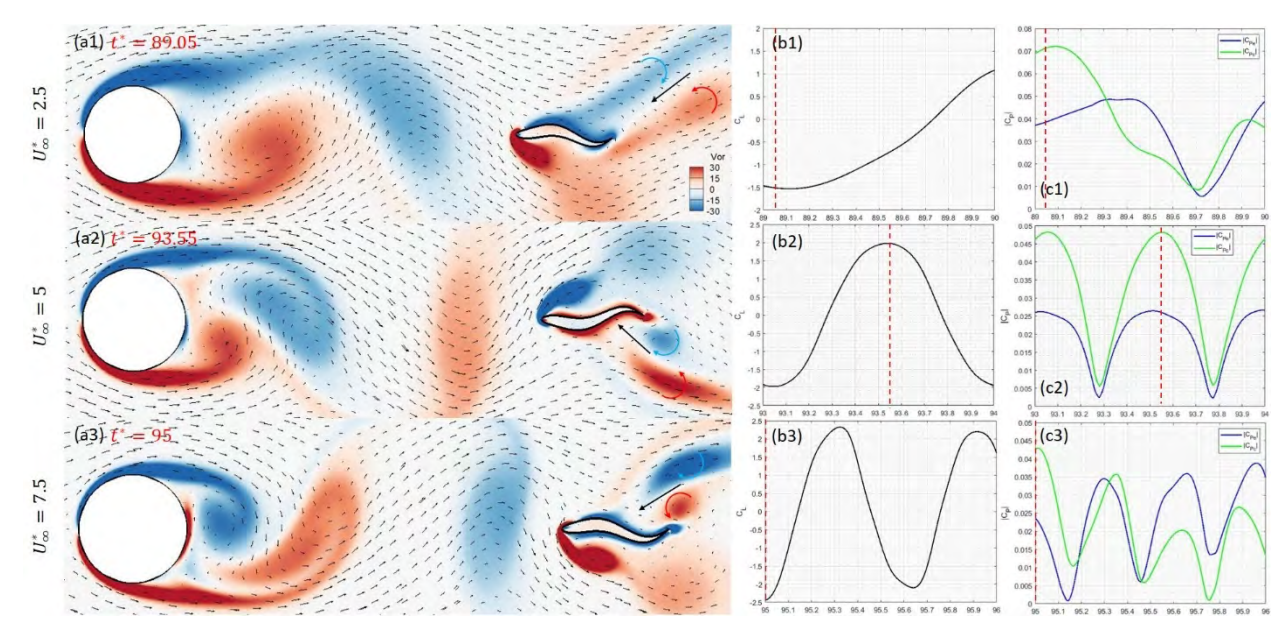


Figure 3-4 Instantaneous velocity field overlaid on vorticity contours (left), lift coefficient  $C_L$  (centre), coefficient of power consumption  $|C_{Pc}|$  and coefficient of power extraction  $|C_{Pe}|$  (right) at the relevant time step when the fish body experiences the smallest  $C_D$  and the largest magnitude of  $C_L$  among  $U_{\infty}^* = 2.5$ , 5 and 7.5. Red dash lines represent the corresponding largest magnitude of  $C_L$ ,  $|C_{Pc}|$  and  $|C_{Pe}|$  at the relevant time steps.

Distributions of force, velocity and power along fish body surface together with pressure contours are shown in Figure 3-5 for discussion on the physics behind the common features of the smallest drag and the largest lateral force among different cases of  $U_{\infty}^*$ . As shown in Figure 3-5(a1-a3), significant pressure difference exists across the fish body. This pressure difference creates a large force on the fish body which is revealed by long force vectors in Figure 3-5(b1-b3). As most of the force vectors are normal to the fish body, the largest lateral force is experienced by the fish body which corresponds to the largest magnitude of  $C_L$  in Figure 3-3(c1-c3). The undulation of the fish body is described in Figure 3-5(c1-c3) while power along the fish body boundary is depicted in Figure 3-5(d1-d3). Power along the body boundary is the product of force exerted on the boundary and velocity of the boundary. When the velocity vector is in the opposite direction to the force vector, power is consumed by the fish, and vice versa. It is observed that significant power consumption happens at the mid-body as the fish consumes energy to undulate in the opposite direction to the lateral force exerted on it. The fish could only extract a small amount of power

from the fluid at the anterior part and the tail of the fish body. This corresponds to peak values of power coefficients shown in Figure 3-4(c1-c3) with  $|C_{Pc}|$  larger than  $|C_{Pe}|$ .

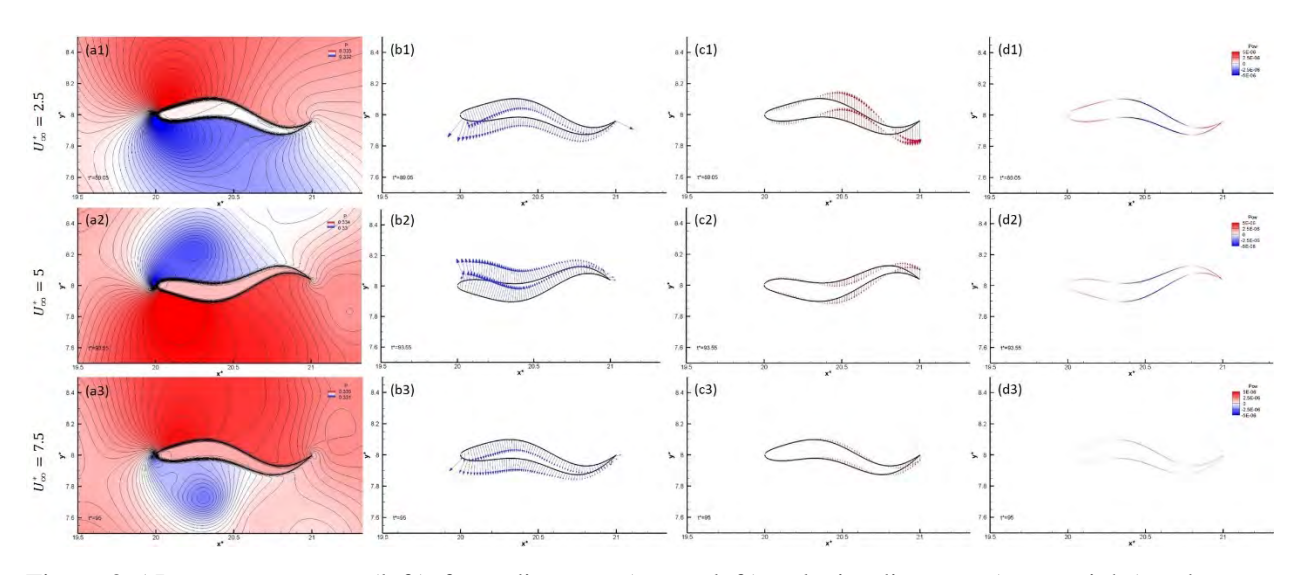


Figure 3-5 Pressure contours (left), force diagrams (centre left), velocity diagrams (centre right) and power diagrams (right) along fish body boundary at the relevant time step when the fish body experiences the smallest  $C_D$  and the largest magnitude of  $C_L$  among  $U_{\infty}^* = 2.5$ , 5 and 7.5.

The common features for moments of the largest drag force and the smallest lateral force on the fish body under different  $U_{\infty}^*$  are presented as follows. Figure 3-6 displays the instantaneous velocity field overlaid on vorticity contours,  $C_D$  and  $C_L$  for  $U_{\infty}^* = 2.5$ , 5 and 7.5 when the fish body experiences the largest drag force (i.e. the highest  $C_D$ ) as shown in Figure 3-6 (b1-b3). At the same time, the smallest lateral force is experienced by the fish body [see Figure 3-6(c1-c3)] for  $C_L \cong 0$ . Except for  $U_{\infty}^* = 2.5$  [i.e. fish in the red square of Figure 3-6(a1)], the fish body is similar to "C" shape for  $U_{\infty}^* = 5$  and 7.5, in which the anterior and posterior parts of the body are curved in the same direction as shown in Figure 3-6(a2) and (a3). It is observed that a pair of vortices occurs at the posterior part of the fish for all three cases of  $U_{\infty}^*$ . The vortex couple exerts the force on the posterior part of the fish. On the opposite side of the vortex couple, a strong fluid flow impacts the fish body. The force exerted by this strong flow outweighs the force exerted by the vortex couple.  $|C_{Pc}|$  and  $|C_{Pe}|$  alongside  $C_L$  and instantaneous velocity field for the same instants as Figure 3-6 are shown in Figure 3-7. Same as the scenario of the smallest drag force with the largest lateral force,  $|C_{Pc}|$  &  $|C_{Pe}|$  are directly related to  $C_L$  as depicted in Figure 3-7 (b1-b3) and

(c1-c3), especially significant for  $U_{\infty}^* = 5 \& 7.5$ . Minimum lateral force exerted on the fish body (i.e.  $C_L \cong 0$ ) correspond to minimum values of power coefficients.

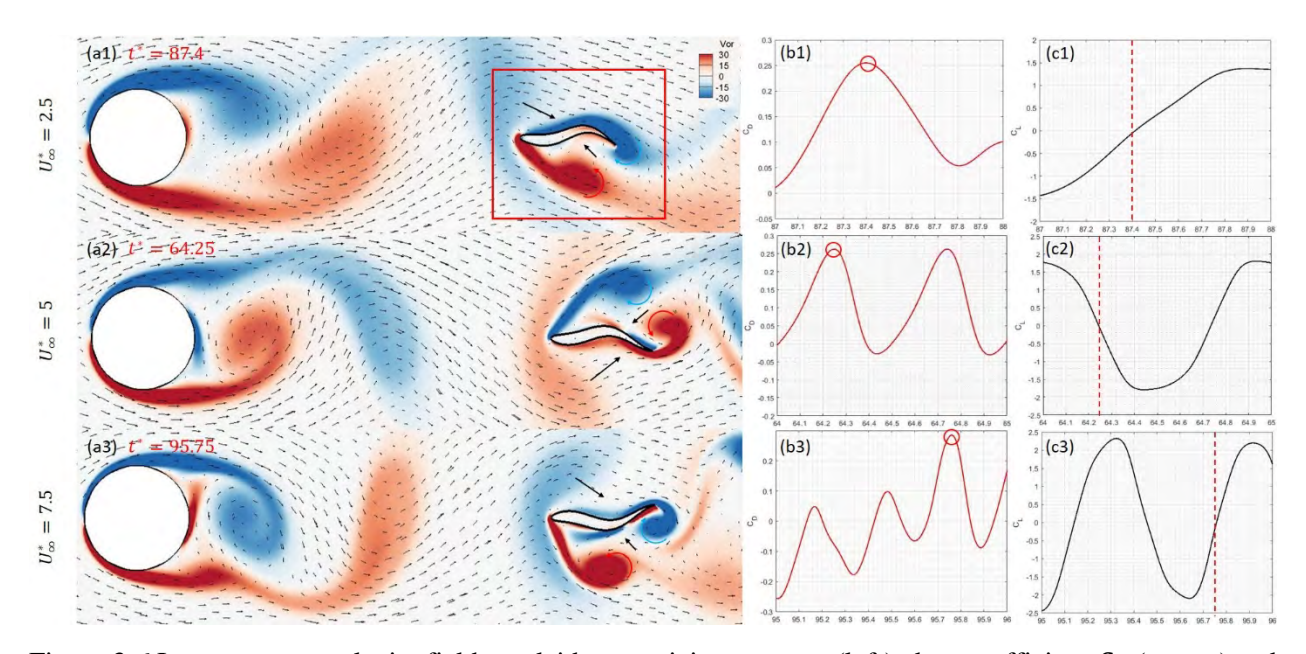


Figure 3-6 Instantaneous velocity field overlaid on vorticity contours (left), drag coefficient  $C_D$  (centre) and lift coefficient  $C_L$  (right) at the relevant time step when the fish body experiences the largest  $C_D$  and the smallest magnitude of  $C_L$  among  $U_{\infty}^* = 2.5$ , 5 and 7.5. Red square identifies the different shape of fish body of  $U_{\infty}^* = 2.5$  from  $U_{\infty}^* = 5$  & 7.5. Red circles and red dash lines represent the corresponding largest  $C_D$  and smallest magnitude of  $C_L$  at relevant time steps.

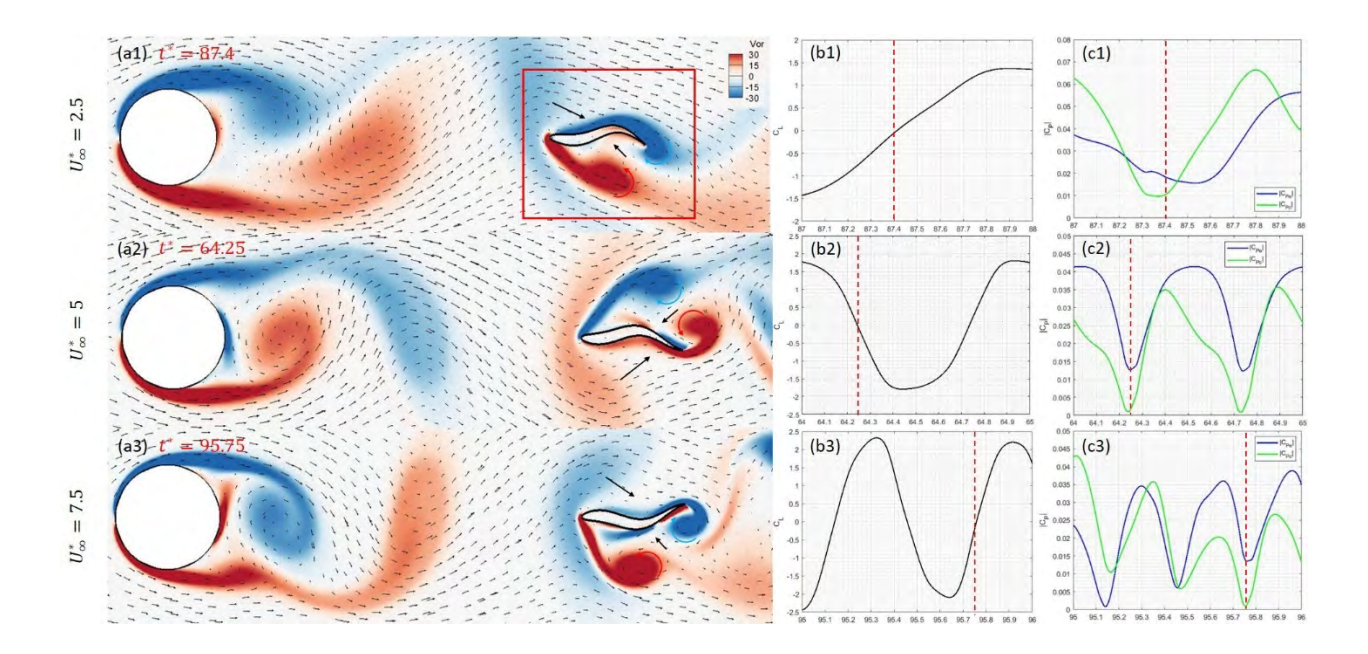


Figure 3-7 Instantaneous velocity field overlaid on vorticity contours (left), lift coefficient  $C_L$  (centre), coefficient of power consumption  $|C_{Pc}|$  and coefficient of power extraction  $|C_{Pe}|$  (right) at the relevant time step when the fish body experiences the largest  $C_D$  and the smallest magnitude of  $C_L$  among  $U_{\infty}^* = 2.5$ , 5 and 7.5. Red square identifies the different shape of fish body of  $U_{\infty}^* = 2.5$  from  $U_{\infty}^* = 5 \& 7.5$ . Red dash lines represent the corresponding smallest magnitude of  $C_L$ ,  $|C_{Pc}|$  and  $|C_{Pe}|$  at relevant time steps.

To reveal the physics behind the common features of the largest drag and the smallest lateral force among different cases of  $U_{\infty}^*$ , diagrams of force, velocity and power along fish body boundary together with graphs of pressure contours are shown in Figure 3-8. As depicted in Figure 3-8(a1-a3), there is not any significant pressure difference across the fish body. Therefore, the force exerted on the fish body is minimal as indicated by short force vectors along the body in Figure 3-8(b1-b3). Moreover, when we look at the force diagrams in detail, it is discovered that most force vectors tilt towards downstream direction at the posterior part of the fish body for all three cases of  $U_{\infty}^*$ . This indicates that drag is produced near the fish tail which corresponds to the largest  $C_D$  in Figure 3-6(b1-b3). At the same time, only few short force vectors are observed normal to the fish body [see Figure3-8(b1-b3)], indicating that the lateral force exerted on the fish is minimal [i.e.  $C_L \cong 0$  as shown in Figure 3-7(b1-b3)]. Power diagrams in Figure 3-8(d1-d3) show that power along the fish boundary is minimal. This corresponds to minimum values of power coefficients in Figure 3-7(c1-c3) as a direct relationship with  $C_L$  in Figure 3-7(b1-b3).

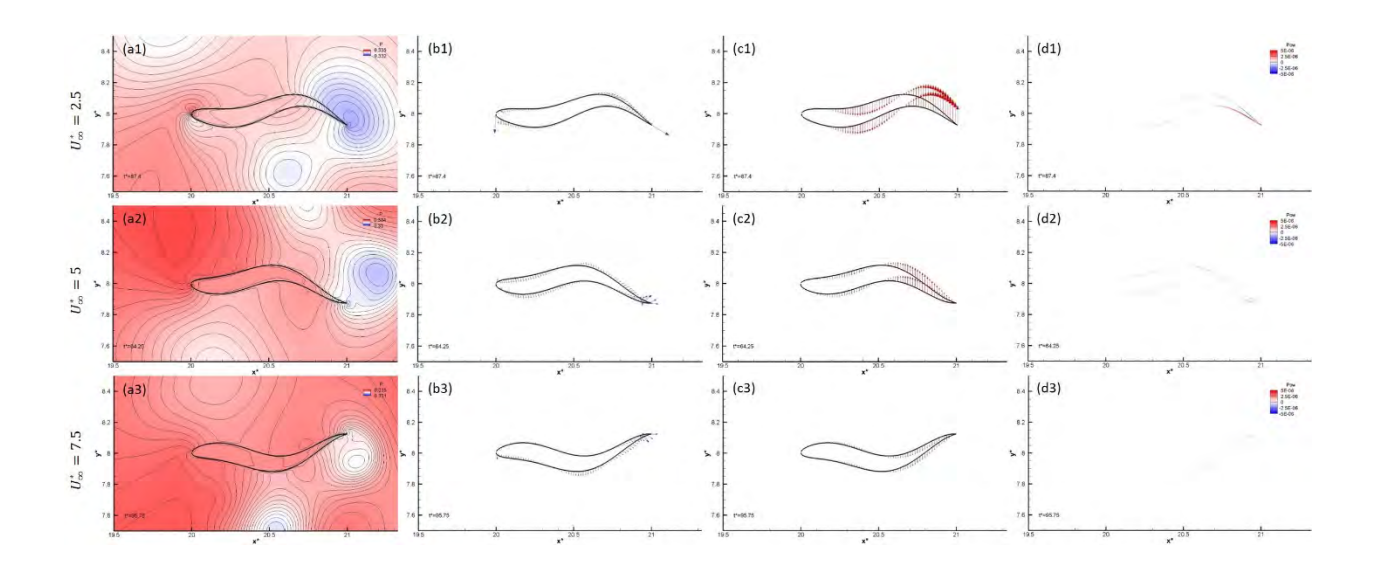


Figure 3-8 Pressure contours (left), force diagrams (centre left), velocity diagrams (centre right) and power diagrams (right) along fish body boundary at the relevant time step when the fish body experiences the largest  $C_D$  and the smallest magnitude of  $C_L$  among  $U_{\infty}^* = 2.5$ , 5 and 7.5.

In the study of effect of free-stream velocity, it is observed that performance parameters  $C_D$  and  $C_L$  fluctuate quasi-periodically. Figure 3-9 shows the time variation of  $C_D$  and  $C_L$  for 50 tail-beat period  $T_P$  from  $t^* = 50$  to 100. It is obvious that the frequency of fluctuation increases with  $U_\infty^*$ . Time dependence of  $C_L$  shows quasi-periodic fluctuation for all cases of  $U_\infty^*$  while that of  $C_D$  only displays quasi-periodic fluctuation for  $U_\infty^* = 2.5$  and 7.5 [see Figure 3-9(b1) and (b3)]. The case of  $U_\infty^* = 5$  is different from others as shown in Figure 3-9(a2) and (b2) in which a low frequency seems to govern the fluctuation of  $C_D$  and  $C_L$ . In addition, we observe that the frequency of  $C_D$  fluctuation is twice of that of  $C_L$  fluctuation. To further investigate the fluctuation of these two performance parameters, Fourier spectrum analysis is employed.

Figure 3-10 presents the Fourier spectra of  $C_D$  and  $C_L$  for all three cases of  $U_\infty^*$ . The spectra on the left illustrate Fourier spectra of  $C_D$  while those on the right illustrate Fourier spectra of  $C_L$ . It can be clearly seen that spectra for  $U_\infty^* = 5$  [see Figure 3-10(a2) and (b2)] are less complex than for  $U_\infty^* = 2.5$  [see Figure 3-10(a1) and (b1)] and 7.5[see Figure 3-10(a3) and (b3)]. Spectra mainly consist of three fundamental frequencies, undulating frequency  $(f_{un})$ , vortex shedding frequency  $(f_{vor})$  and a beating frequency  $(f_b)$ .  $f_b$  is actually the difference between  $f_{un}$  and  $f_{vor}$  as the fish undulation interacts with vortex shed from the cylinders. In the  $C_L$  spectra,  $f_{vor}$  appear as the maximum peaks for all cases of  $U_\infty^*$  which means vortex shed from the cylinder plays an important role in the lateral force of the fish.  $f_{un}$  also present in the spectral with lower peaks than  $f_{vor}$ , however. This reveals an interesting fact that forces on the fish are more influenced by vortex shed from the upstream cylinder rather than the undulation itself. For the case of  $U_\infty^* = 5$ ,  $f_{un}$  seems to be absent from the spectra. The reason is that  $f_{un}$  and  $f_{vor}$  are approaching the same value so it is nearly impossible to distinguish between them. Therefore, it is also difficult to identify  $f_b$  for  $U_\infty^* = 5$ .

The first harmonic of vortex shedding frequency,  $2f_{vor}$ , appear as the dominant peaks in the  $C_D$  spectra, which dominate the drag of the fish. The first harmonic of undulating frequency,  $2f_{un}$ ,

could also be found in the  $C_D$  spectra for  $U_\infty^*=2.5$  and 7.5 with lower peaks than  $2f_{vor}$ . The second harmonic of vortex shedding frequency,  $3f_{vor}$ , are present in the  $C_L$  spectra which are produced by the nonlinear interaction between vortex shedding frequency  $f_{vor}$  and its first harmonic  $2f_{vor}$ . Similarly, the second harmonic of undulating frequency,  $3f_{un}$ , appear in the  $C_L$  spectra for  $U_\infty^*=2.5$  and 7.5. Subsequent harmonics of vortex shedding and undulating frequencies are present alternatively in the spectra with odd number harmonic in the  $C_L$  spectra and even number in the  $C_D$  spectra.

Besides the harmonics of vortex shedding and undulating frequencies, it is observed from the  $C_D$  and  $C_L$  spectral distribution that vortex shedding frequencies interact with the beating frequency to produce a series of combined frequencies for  $U_{\infty}^* = 2.5$  and 7.5 (i.e.  $f_{vor} \pm f_b$ ,  $f_{vor} \pm 2f_b$ ,  $2f_{vor} \pm f_b$ , etc.). The case of  $U_{\infty}^* = 7.5$  shows the most complex spectral distribution as we can see more combined frequencies and harmonic components. This is due to the increase of instability with the increase of  $U_{\infty}^*$  and hence  $Re_{\infty}$ . The more combined frequencies exist, the more tendency of performance parameters (i.e.  $C_D$  and  $C_L$ ) to quasi-periodic. The higher are the amplitudes of combined frequencies, the stronger of the nonlinear interaction between strong vortex shedding from the cylinder and the fish undulation, corresponding to the flow structure in Figure 3-2(c).

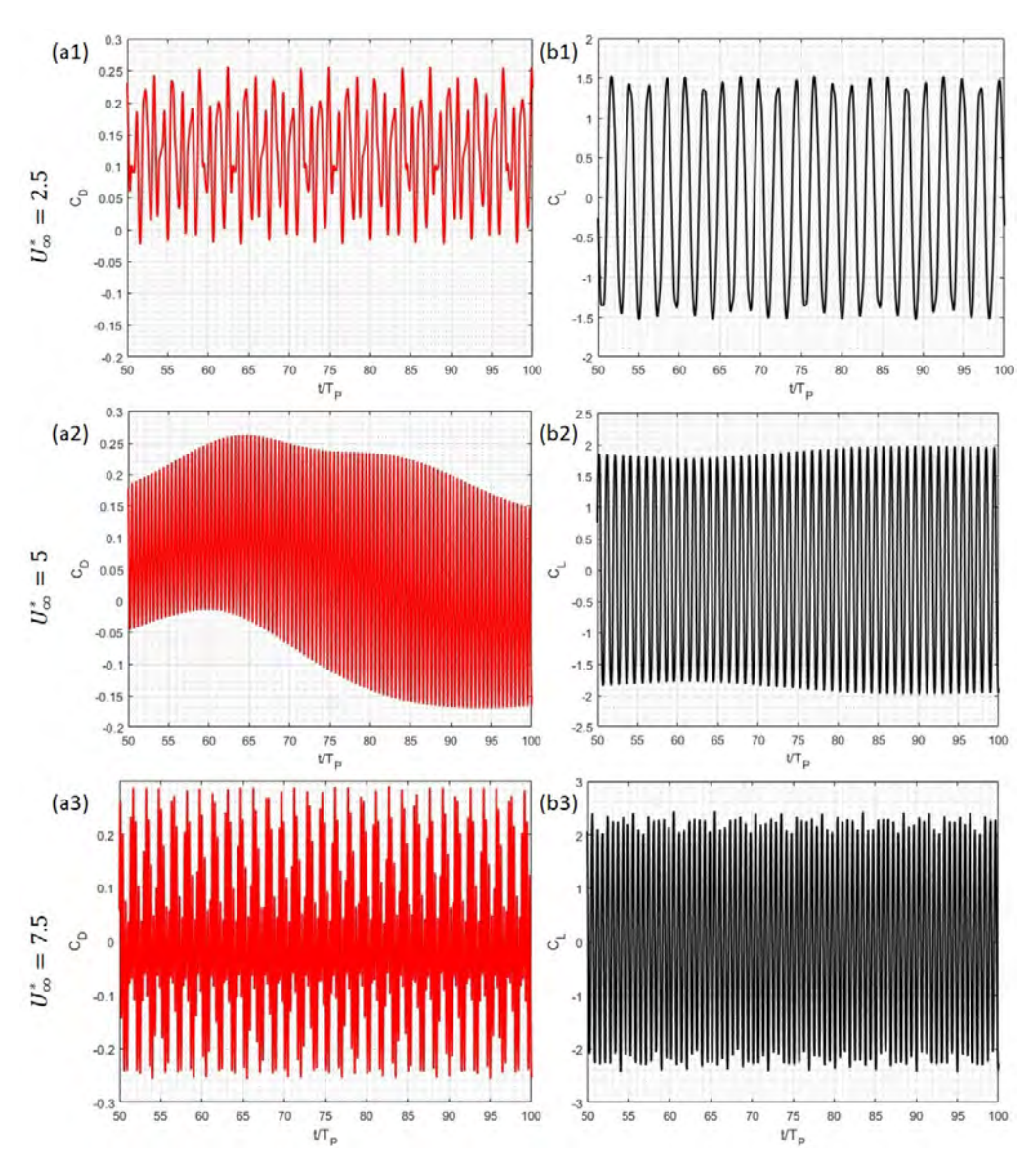


Figure 3-9 Time variation of  $C_D$  (left) and  $C_L$  (right) of the fish undulating downstream of the cylinder at  $d_x^* = 4$  for 50 tail-beat period  $(T_P)$  from  $t^* = 50$  to 100 for cases of  $U_\infty^* = 2.5, 5$  and 7.5.

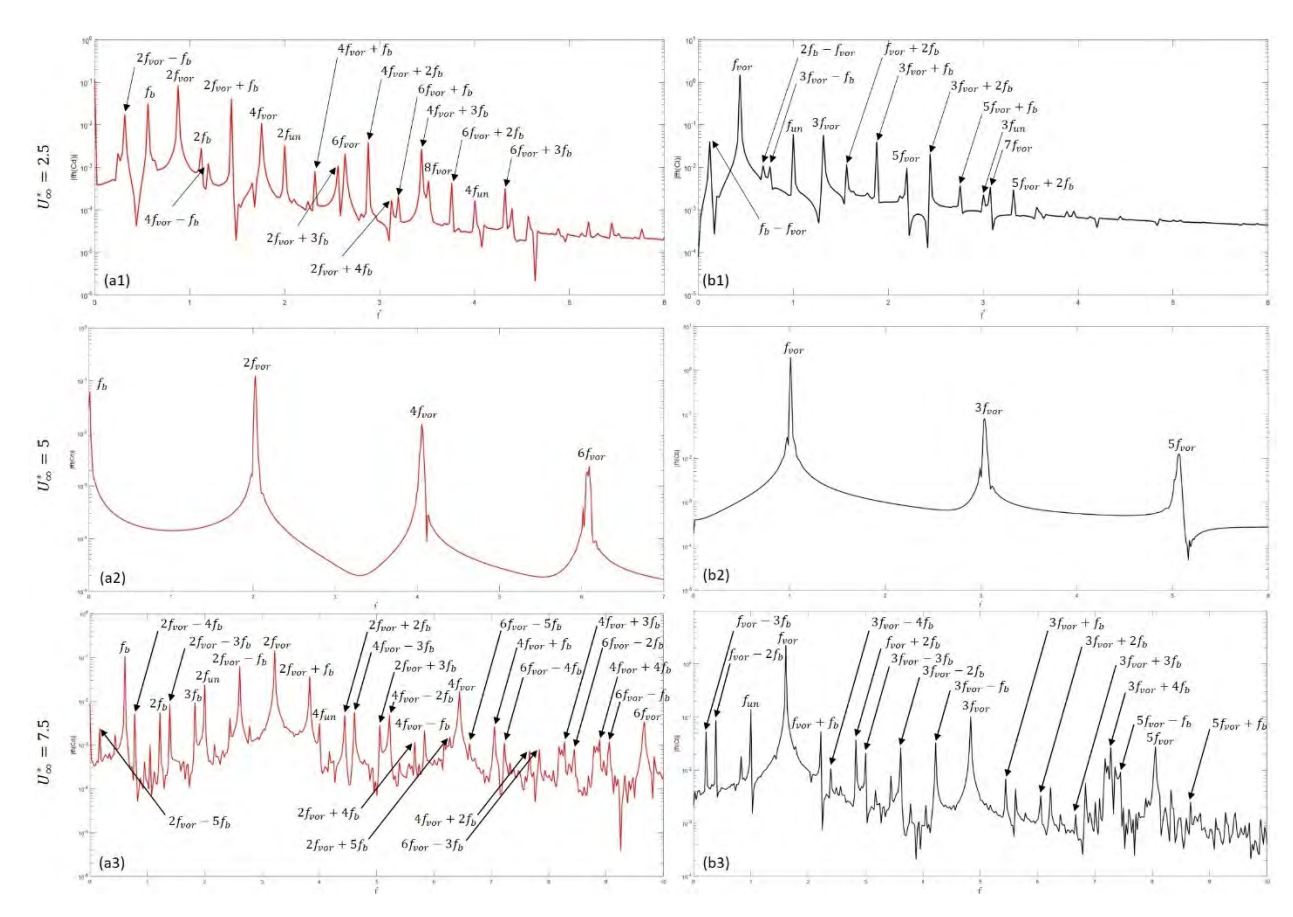


Figure 3-10 Fourier spectra of  $C_D$  (left) and  $C_L$  (right) on the fish undulating downstream of the cylinder at  $d_x^* = 4$  for cases of  $U_\infty^* = 2.5$ , 5 and 7.5 resepctively.

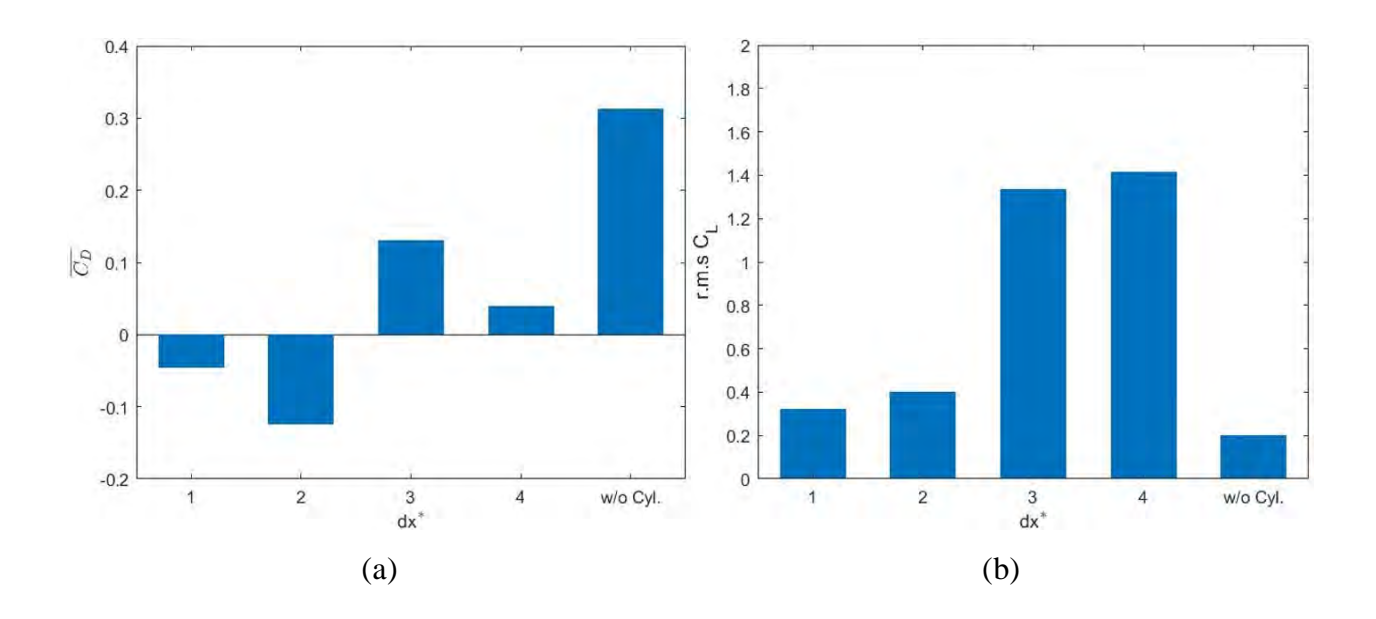
# 3.2. Effect of Streamwise Distance

In the study of effect of streamwise distance  $(d_x^*)$ , other parameters are set to their baseline values, i.e.  $D^* = 1$ ,  $d_y^* = 0$  and  $U_\infty^* = 5$ . Four streamwise distances,  $d_x^* = 1$ , 2, 3 and 4, are examined in the study. Figure 3-11 display  $\overline{C_D}$ ,  $C_{L\,rms}$  and  $\overline{C_P}$  of the fish with respect to different  $d_x^*$ . The case without the presence of the cylinder is also presented for comparison.

As we can see from Figure 3-11(a), the presence of the cylinder can minimize the drag experienced by the fish. The fish experiences thrust, as indicated by negative values of  $\overline{C_D}$ , when it is positioned at  $d_x^* = 1 \& 2$  and drag at  $d_x^* = 3 \& 4$ .  $\overline{C_D}$  shows a decreasing trend towards a more negative value (i.e. increasing thrust) initially from  $d_x^* = 1$  to 2. It then increases dramatically to the highest positive value among all distances at  $d_x^* = 3$  before decreases again to a lower positive value (i.e. drag) at  $d_x^* = 4$ .

The results for  $C_{L\,rms}$  are different from those for  $\overline{C_D}$ . As depicted in Figure 3-11(b),  $C_{L\,rms}$  increases monotonically with  $d_x^*$  overall while a dramatical increase from  $d_x^* = 2$  to 3 is observed. Therefore, we can divide result of  $C_{L\,rms}$  into two groups with large  $C_{L\,rms}$  at  $d_x^* = 1$  & 2 and small  $C_{L\,rms}$  at  $d_x^* = 3$  & 4. For the scenario without the presence of the cylinder,  $C_{L\,rms}$  is comparatively lower than all cases with the cylinder because of the large lateral force induced on the undulating fish with "nose" fixed by vortices shed from the cylinder.

The results for  $\overline{C_P}$  are also categorized into two groups as per previous study, based on power consumption and power extraction. The results in general follow those for  $C_{L\,rms}$  with the watershed between  $d_x^* = 2$  and 3. As depicted in Figure 3-11(c), for  $d_x^* = 1$  & 2, the coefficients of power consumption are slightly larger than those of power extraction. In contrast, the coefficients of power consumption are slightly smaller than the coefficients of power extraction for  $d_x^* = 3$  & 4. It is discovered that the coefficient of power extraction is much larger than that of power consumption (i.e. around 1.5 times) while both coefficients of power are similar to each other for other  $d_x^*$ . This phenomenon also occurs in the scenario without the presence of the cylinder.



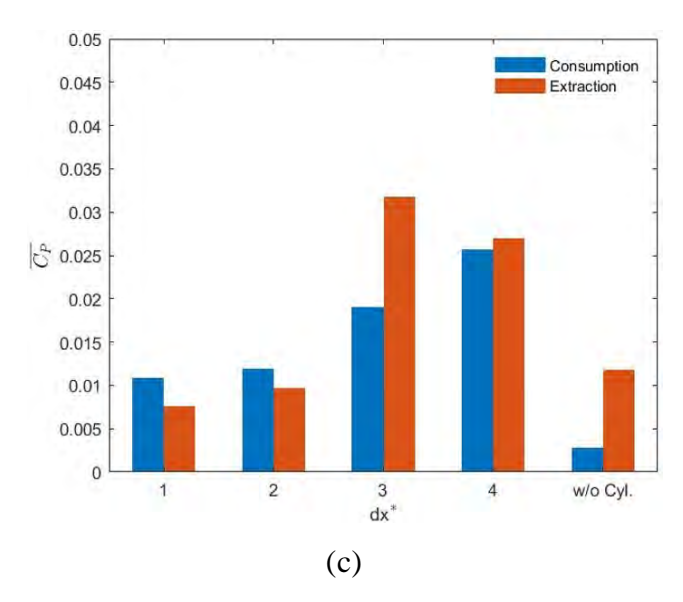


Figure 3-11 Performance parameters for streamwise distances  $d_x^* = 1, 2, 3 \& 4$  and without the presence of the cylinder: (a) time-averaged drag coefficient ( $\overline{C_D}$ ), (b) root-mean squared lift coefficient ( $C_{Lrms}$ ) and (c) time-averaged power coefficient ( $\overline{C_P}$ ) of the fish.

The flow structure between the fish and the cylinder for different  $d_x^*$  is presented in Figure 3-12. For the cases of  $d_x^* = 1 \& 2$ , there is not any significant vortex between the cylinder and the fish [see Figure 3-12(a1) and (a2)] while strong vortex shedding from the cylinder down towards the fish is observed for cases of  $d_x^* = 3 \& 4$  [see Figure 3-12(a3) and (a4)]. As  $d_x^* < 3$ , the fish is in the suction zone which the fluid flows in the opposite direction to that far-field. This is shown by insignificant [see Figure 3-12(a1)] and reverse velocity vectors [see Figure 3-12(a2)] for  $d_x^* = 1 \& 2$  resepctively. It corresponds to the thrust obtained by the fish at  $d_x^* = 1 \& 2$  in Figure 3-11(a). The pressure contours [see Figure 3-12(b1) and (b2)] and force diagrams [see Figure 3-12(c1) and (c2)] for  $d_x^* = 1 \& 2$  do not show significant pressure difference across and forces exerted on this fish body. This also explains small values of  $C_{L\,rms}$  and thus  $\overline{C_P}$  for  $d_x^* = 1 \& 2$ .

In contrast, for  $d_x^* \ge 3$ , it is clearly observed that a strong interaction happens between the cylinder and the undulating fish as depicted by strong vortical flow in Figure 3-12(a3) and (a4). Velocity vectors in between the cylinder and the fish are strong and point towards the "nose and the anterior part of the fish. This strong vortical flow creates a large pressure difference across the fish body as indicated by Figure 3-12(b3) and (b4). Due to the significant pressure difference, large lateral forces could be found for  $d_x^* = 3 \& 4$  [see Figure 3-12(c3) and (c4)]. Looking at velocity field

around the fish at  $d_x^* = 3$  & 4 in detail, the vortex shed form the cylinder exerts force to the lower posterior part of the fish at  $d_x^* = 3$  [see Figure 3-12(a3)] while a pair of vortices is shed from the posterior part of the fish at  $d_x^* = 4$  [see Figure 3-12(a4)]. The force exerted by the shed vortex is the drag imposed on the fish body at  $d_x^* = 3$  as shown by force vectors tilted towards downstream in Figure 3-12(c3), corresponding to the positive value of  $C_D$  for  $d_x^* = 3$ . On the other hand, the pair of vortices exerted forces on the upper posterior part of the fish in the direction opposite to the fluid flow [see Figure 3-12(c4)] for  $d_x^* = 4$ . That explains the lower value of  $C_D$  for  $d_x^* = 4$  comparing with  $C_D$  for  $d_x^* = 3$ .

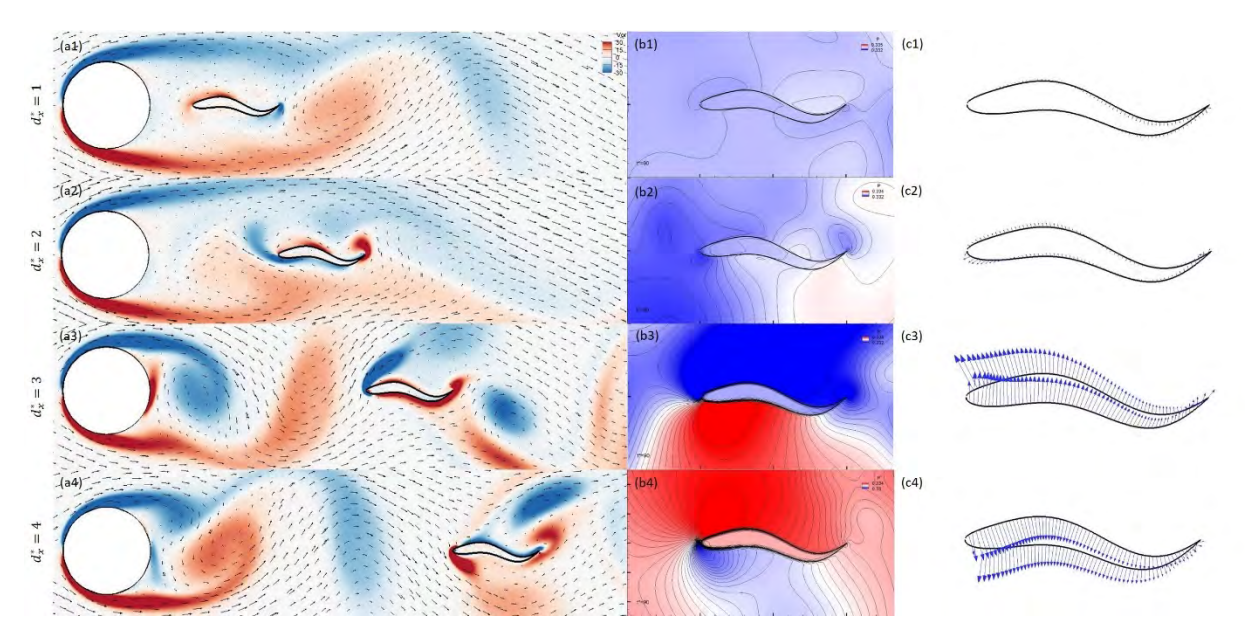


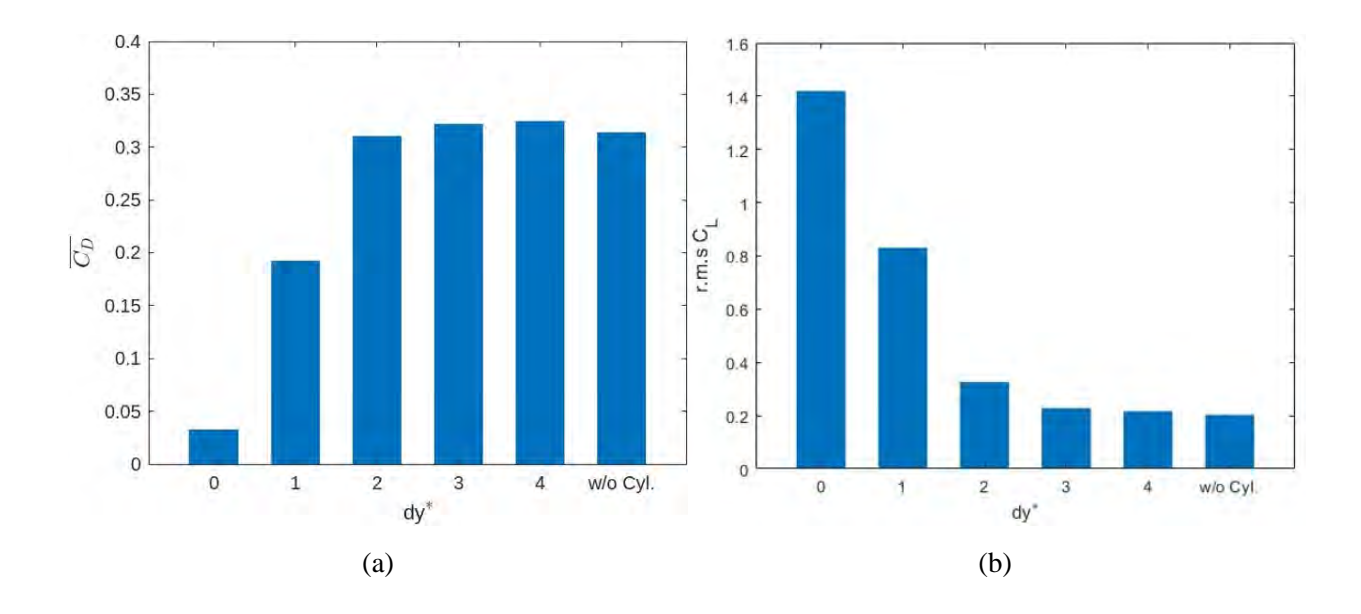
Figure 3-12 Instantaneous velocity field overlaid on vorticity contours (left), pressure contours (centre), force diagrams along fish body boundary (right) at  $t^* = 90$  for  $d_x^* = 1,2,3 \& 4$ .

### 3.3. Effect of Crossflow Distance

The crossflow distance  $(d_y^*)$  also affects the performance of the fish undulation. To explore its effect, other parameters are set to their baseline values, i.e.  $D^* = 1$ ,  $d_x^* = 4$  and  $U_\infty^* = 5$ . Five crossflow distances,  $d_y^* = 0, 1, 2, 3$  and 4, are examined in the study. Figure 3-13 shows  $\overline{C_D}$ ,  $C_{L\,rms}$  and  $\overline{C_P}$  of the fish with respect to different  $d_y^*$ . The scenario without the presence of the cylinder is also included for the comparison.

As illustrated in Figure 3-13(a), when the fish is positioned at  $d_y^* = 0 \& 1$ ,  $\overline{C_D}$  decreases in comparison with the scenario which the cylinder is absent. The drop in  $\overline{C_D}$  for  $d_y^* = 0$  is especially significant. When  $d_y^* \ge 2$ , values of  $\overline{C_D}$  are similar to that without the presence of the cylinder. However, the results for  $C_{L\,rms}$  are opposite to those for  $\overline{C_D}$ . Figure 3-13(b) records the largest  $C_{L\,rms}$  for  $d_y^* = 0$ , nearly 7 times larger than the scenario without the cylinder.  $C_{L\,rms}$  shows a decreasing trend with the increase of  $d_y^*$  from 0 to 2 while the values for  $d_y^* = 3 \& 4$  are almost equal to that without the cylinder.

The results for  $\overline{C_P}$  are categorized as per previous studies into power consumption and power extraction. The general trend follows that of  $C_{L\,rms}$ . Except for  $d_y^*=0$ , coefficient of power extraction is always larger than coefficient of power consumption, including the case without the presence of the cylinder. The cases of  $d_y^*=2$ , 3 & 4 and without the cylinder share similar values of power consumption and extraction respectively.



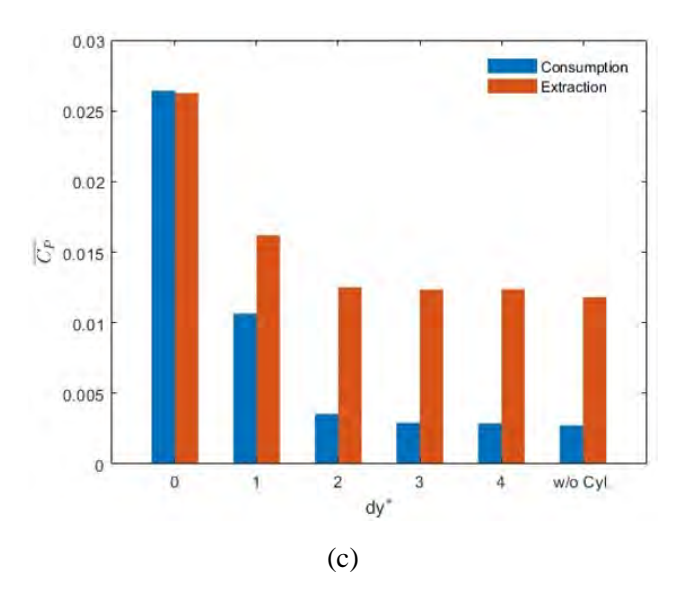


Figure 3-13 Performance parameters for crossflow distances  $d_y^* = 0, 1, 2, 3 \& 4$  and without the presence of the cylinder: (a) time-averaged drag coefficient  $(\overline{C_D})$ , (b) root-mean squared lift coefficient  $(C_{L rms})$  and (c) time-averaged power coefficient  $(\overline{C_P})$  of the fish.

To reveal the physics behind the observation above, Figure 3-14 is presented to show the vorticity contours, pressure contours and force diagrams along the fish body for  $d_y^* = 0$ , 1, 2, 3 & 4. For  $d_y^* = 0$ , the fish undulates at the position aligned longitudinally with the centre of the cylinder as shown in Figure 3-14(a1). As described in the previous section, the fish interacts with strong vortices shed from the cylinder. This strong vortical flow creates a large pressure difference across and thus a large lateral force on the fish body as indicated by Figure 3-14(b1) and (c1) respectively. A pair of vortices is shed from the posterior part of the fish which exerts a force on the upper posterior part of the fish in the direction opposite to the fluid flow [see Figure 3-14(c1)]. Therefore, thrust is produced and  $\overline{C_D}$  for  $d_y^* = 0$  is lower than other cases as shown in Figure 3-13(a).

For  $d_y^* = 1$ , the fish is placed laterally at the edge of the vortex passage. It is observed that interaction exists between the fish and the cylinder to a lesser extent [see Figure 3-14(a2)]. The vortical flow from the cylinder, together with the fish undulation, create a significant pressure difference across the fish body as depicted in Figure 3-14(b2). Therefore, lateral force is produced and a certain value of  $C_{L\,rms}$  is recorded as in Figure 3-13(b). At the posterior part of the fish, the pressure difference produces force vectors titling towards downstream [see Figure 3-14(c2)]. This constitutes major part of drag on the fish (i.e.  $\overline{C_D}$ ) as recorded in Figure 3-13(a).

For  $d_y^* \ge 2$ , the fish is placed laterally far away from the vortex passage as shown in Figure 3-14(a3-a5) that it undulates independently without any interaction with the cylinder. As a result, cases of  $d_y^* = 2,3 \& 4$  could be treated as the undulation of the fish solely, and therefore performance parameters closely resemble those of the scenario without the presence of the cylinder.

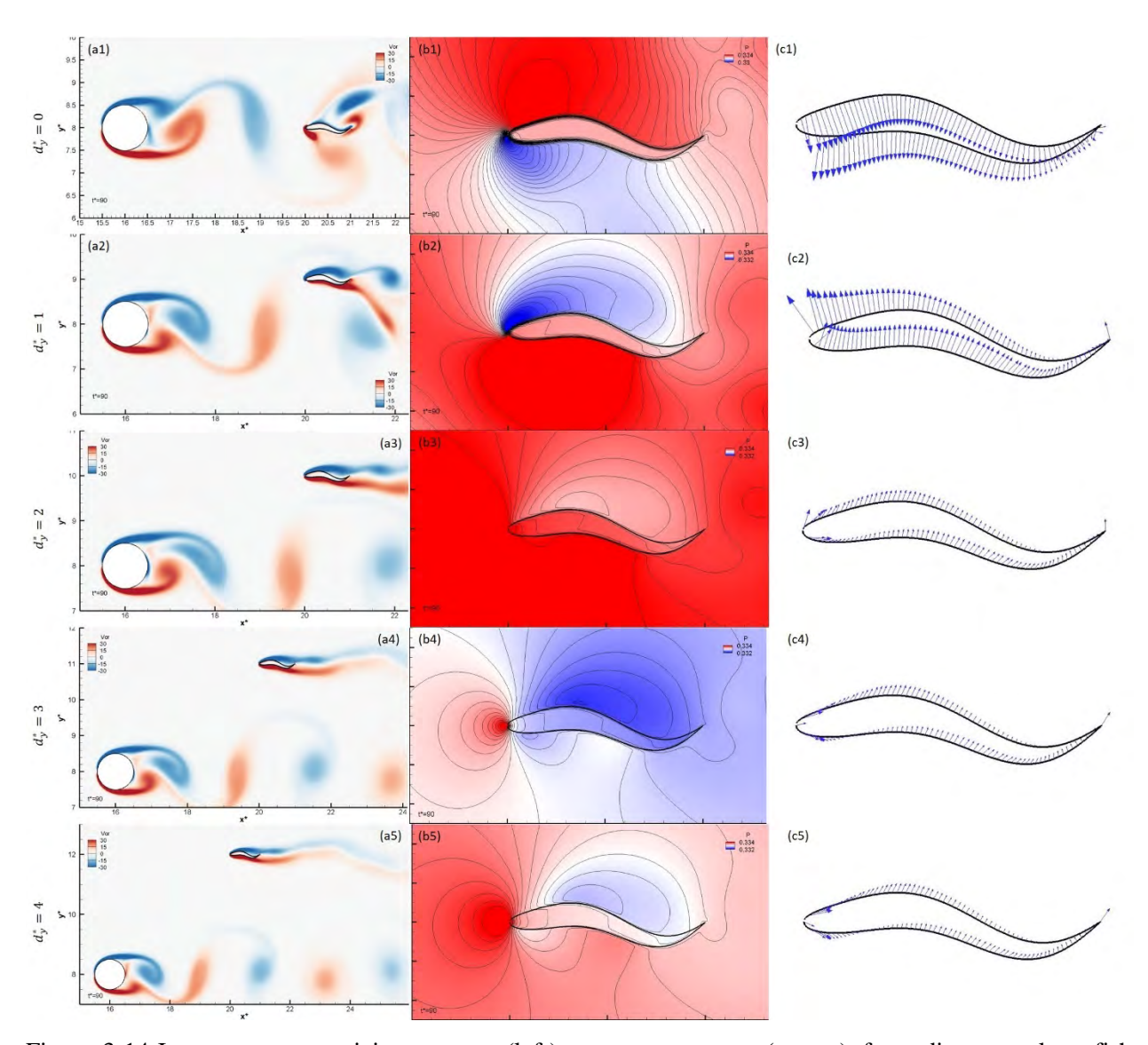


Figure 3-14 Instantaneous vorticity contours (left), pressure contours (centre), force diagrams along fish body boundary (right) at  $t^* = 90$  for  $d_y^* = 0, 1, 2, 3 \& 4$ .

# 3.4. Effect of Upstream Cylinder Diameter

The cylinder diameter ( $D^*$ ) is another parameter which could affect the swimming performance of the fish. To explore its effect, other parameters are set to their baseline values, i.e.  $d_x^* = 4$ ,  $d_y^* = 0$  and  $U_{\infty}^* = 5$ . Eight diameters,  $D^* = 0.5$ , 1, 2, 3, 4, 5, 6 and 7, are examined in the study. Figure 3-15 shows  $\overline{C_D}$ ,  $C_{L\,rms}$  and  $\overline{C_P}$  of the fish with respect to different  $D^*$ . The scenario without the cylinder is also included for easy reference.

As depicted in Figure 3-15(a),  $\overline{C_D}$  are positive values for  $D^* = 0.5$ , 1 & 2 while negative values for  $D^* = 3$ , 4, 5, 6 & 7 (i.e. thrust) with all cases of  $D^*$  showing  $\overline{C_D}$  lower than that for the scenario without the presence of the cylinder. This again proves the effectiveness of the cylinder on drag reduction in fish swimming. It is observed that the lowest positive  $\overline{C_D}$  occurs for  $D^* = 1$  while the highest positive  $\overline{C_D}$  occurs for  $D^* = 2$ . It is intuitive that thrust is produced for  $D^* = 3$ , 4, 5, 6 & 7 as the size of the cylinder is sufficiently large to create a suction zone for the fish.

Figure 3-15(b) shows the comparison of  $C_{L\,rms}$  with similar results (i.e. value around 1.4 to 1,8), except for  $D^* = 0.5$ . All cases of  $D^*$  have larger  $C_{L\,rms}$  than the scenario without the cylinder as large lateral force is induced through the interaction between vortices shed from the cylinder and the undulation of fish body with "nose" fixed.  $\overline{C_P}$  follows the results of  $C_{L\,rms}$  generally with power extraction larger than power consumption for  $D^* = 2$  observed [see Figure 3-15(c)].

For  $D^* = 0.5$ , 1 & 2, the size of the fish is comparable to that of the cylinder. Therefore, the distance between the cylinder and the fish downstream is sufficient for the development of vortex and shedding from the cylinder as depicted in Figure 3-16(a1-a3). For  $D^* = 0.5$ , the vortex from the cylinder sheds around  $d_x^* = 2$ . Due to its comparable size with the width of the fish, the vortex creates a pressure as shown in Figure 3-16(b1) and thus drag force on the "nose" of the fish. There is not any significant lateral force exerted on other parts of the body [see Figure 3-16(c1)]. This corresponds the lowest  $C_{L\,rms}$  and  $\overline{C_P}$  as indicated in Figure 3-15.

For  $D^* = 1$ , the vortex sheds from the cylinder around  $d_x^* = 3$ . As the vortex is larger than the width of the fish, the interaction between the fish and the cylinder is not concentrated to the "nose",

but to both upper and lower body boundaries of the fish This creates a large pressure difference across the fish body and thus produces larger lateral force along the fish boundary [see Figure 3-16(b2) and (c2)]. That explains larger  $C_{L\,rms}$  and  $\overline{C_P}$  comparing with  $D^* = 0.5$ . A pair of vortices is found shedding from the upper posterior part of the fish as shown in Figure 3-16(a2). It exerts a force on the upper posterior part of the fish in the direction against the fluid flow [see Figure 3-16(c2)]. Thus, thrust is produced and  $\overline{C_D}$  is lower than  $D^* = 0.5 \& 2$  as displayed in Figure 3-15(a).

For  $D^* = 2$ , the size of vortex is much larger than the width of the fish. The vortex from the cylinder is elongated and not shed completely when it arrives at the "nose" of the fish [see Figure 3-16(a3)]. It affects the shear layer on the fish and creates drag over posterior part of the fish [see Figure 3-16(c3)]. As the fish extracts energy when it undulates in the same direction as the lateral force exerted on its boundary, it is observed that significant power extraction occurs at the posterior part. This corresponds to the significant large coefficient of power extraction over consumption for  $D^* = 2$  in Figure 3-15(c).

For  $D^* = 3, 4, 5, 6 \& 7$ , as shown in Figure 3-16(a4-a8), the size of the cylinder is large enough to produce the suction zone for the fish. The vortex shedding from the cylinder occurs at the posterior part of the fish for  $D^* = 3 \& 4$  and even downstream of the fish for  $D^* = 5, 6 \& 7$ . The shed vortices merely affect the nose and the anterior part of the fish. For  $D^* = 3 \& 4$ , the pressure difference between the anterior and posterior parts of the fish body creates thrust on the fish [see Figure 3-16(b4-b5)]. For  $D^* = 5, 6 \& 7$ , the vortices shed downstream of the fish create the reverse flow, striking the tail and the posterior part of the fish. Therefore, thrust is produced on the fish as shown in Figure 3-16(c6-c8). These explain the negative values of  $\overline{C_D}$  for  $D^* = 3, 4, 5, 6 \& 7$  in Figure 3-15(a).

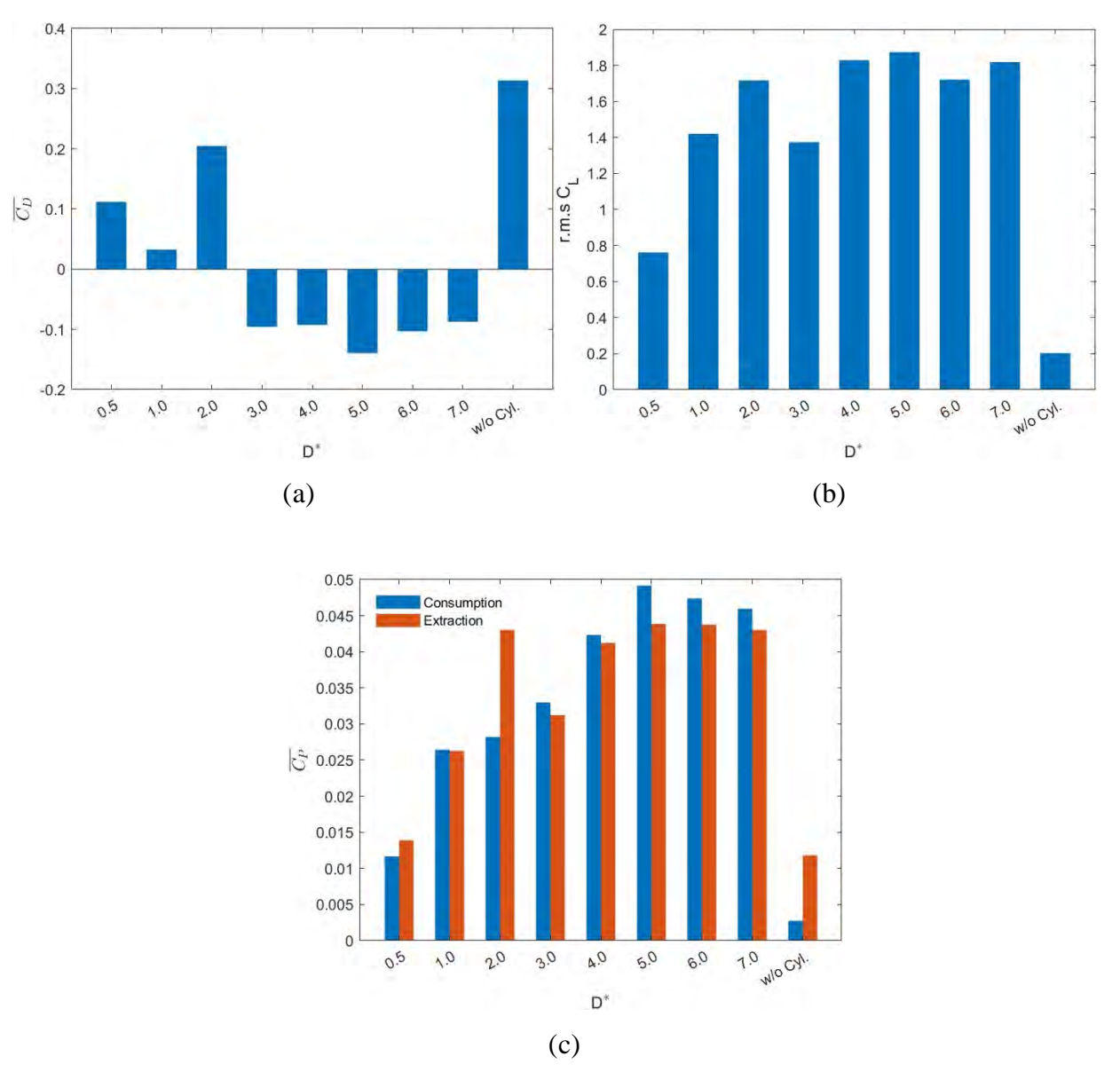


Figure 3-15 Performance parameters for diameter of the cylinder  $D^* = 0.5, 1, 2, 3, 4, 5, 6 \& 7$  and without the presence of the cylinder: (a) time-averaged drag coefficient  $(\overline{C_D})$ , (b) root-mean squared lift coefficient  $(C_{Lrms})$  and (c) time-averaged power coefficient  $(\overline{C_P})$  of the fish.

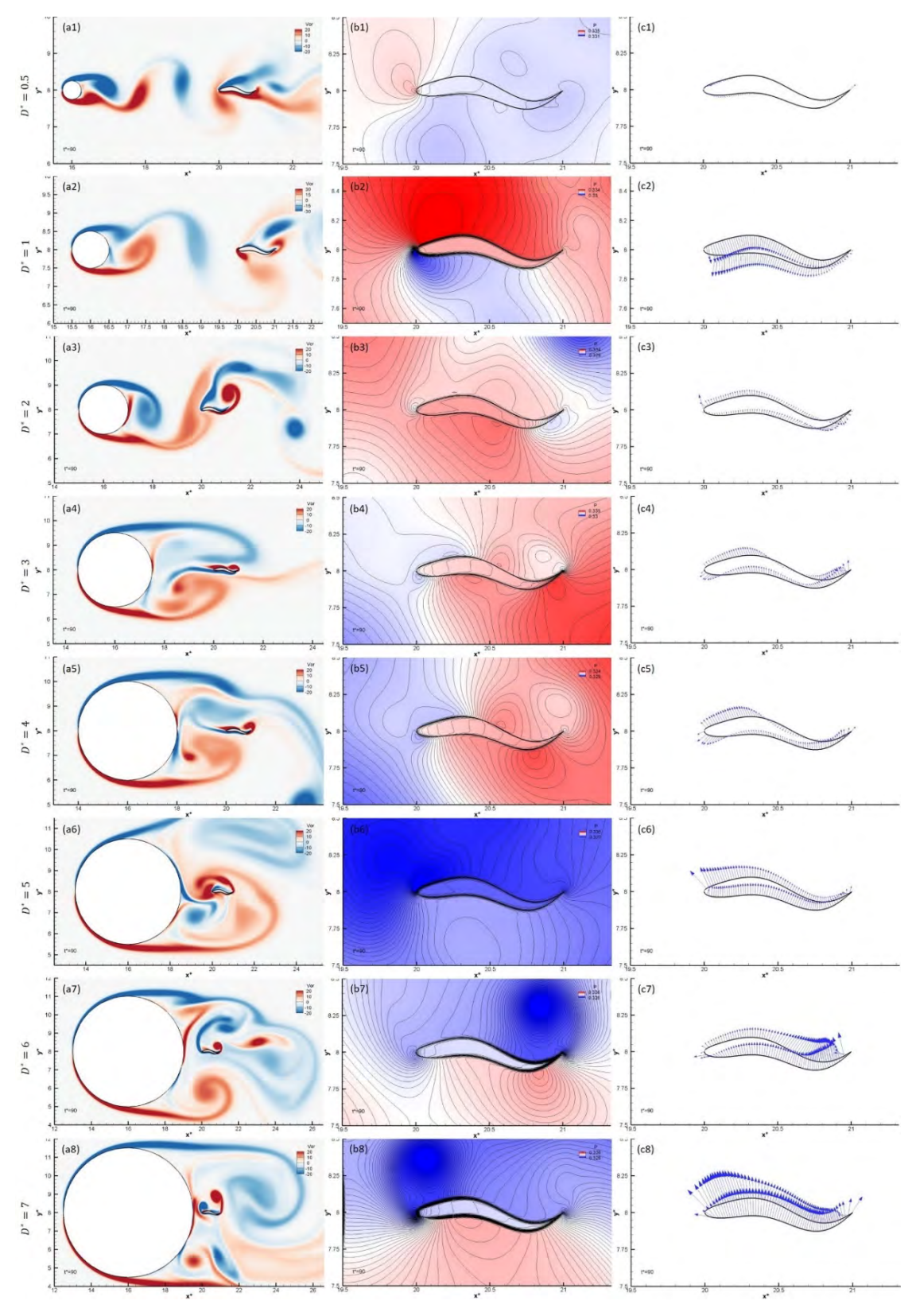


Figure 3-16 Instantaneous vorticity contours (left), pressure contours (centre), force diagrams along fish body boundary (right) at  $t^* = 90$  for  $D^* = 0.5, 1, 2, 3, 4, 5, 6 & 7$ .

## 3.5. Remarks

In this chapter, undulation without translation and rotation behind a single cylinder is studied. By varying controlling parameters, this constrained swimming motion mode was investigated with the results summarized as follows:

- Drag imposed on the fish decreases with free-stream velocity while lateral force increases with free-stream velocity. Power of consumption and extraction of the fish generally decreases with free-stream velocity. Common features regarding flow structure among different free-stream velocities at the moments of the smallest and largest drag and the largest lateral force on the fish are revealed.
- 2. Beating frequency, vortex shedding frequency and undulating frequency together with their relative harmonics are observed in the spectral analysis of drag and lateral force on the fish. These frequencies interact with each other to produce a complex spectrum.
- 3. Thrust is found on the fish body when it is positioned at the short streamwise distance with the cylinder (i.e.  $d_x^* = 1 \& 2$ ) with insignificant vortex shedding between the cylinder and the fish. In contrast, drag is discovered for longer streamwise distance (i.e.  $d_x^* = 3 \& 4$ ) with significant vortex shedding in between.
- 4. Drag decreases only when the fish is positioned close to the cylinder in the crossflow direction (i.e.  $d_y^* = 0 \& 1$ ). The fish undulates independently of the cylinder when it is far away from the cylinder in the crossflow direction.
- 5. When the cylinder size increases, the reverse flow occurs and pushes the fish towards the cylinder. This creates both thrust and large lateral force on the fish.

# Chapter 4 Undulation of Rotation only body behind Single Cylinder

After the study on the fundamental motion of the fish (i.e. undulation without translational and rotational motion) and its interaction with the wake from an upstream cylinder, the degree of freedom of the fish is released to allow rotational motion. As depicted in Figure 2-3(a), the "nose" of the fish model is positioned at a chosen position (i.e.  $d_x^* \& d_y^*$ ) initially. The fish model undulates as prescribed by equation (2.1) and rotation is allowed about its centroid. For ease of discussion, all relevant parameters with adopted values are listed in Table 4.1. Owing to the complexity involved in the computation with the rotation being released,  $U_\infty^*$  is reduced to 2.5 while  $Re_{fish}$  and  $D^*$  maintained to be 40 and 1 respectively. To explore the effect of different parameters, a baseline value is assigned to each parameter, i.e.,  $d_x^* = 2$  and  $d_y^* = 0$ .

Table 4.1 Definitions and chosen values of relevant parameters in Chapter 4

Parameter	Definition	Values <sup>a,b</sup>
Cylinder diameter	$D^* = D/L$	1
Streamwise distance	$d_x^* = d_x/L$	1, <b>2</b> , 2.5, 2.6, 2.7, 2.8, 2.9, 3, 4
Crossflow distance	$d_y^* = d_y/L$	<b>0</b> , 0.1, 0.2, 0.3, 0.4, 0.5, 1, 2, 3
Reynolds number	$Re_{fish} = V_{max}L/\nu$	40
(fish undulatory velocity)		
Reynolds number	$Re_{\infty} = U_{\infty}L/\nu$	127.3
(free-stream flow)		
Strouhal number	$St = f_{vor}D/U_{\infty}$	-
Time	$t^* = t/T_P = tU_{ref}/L$	-
Free-stream velocity	$U_{\infty}^{*}=U_{\infty}/U_{ref}$	2.5

<sup>&</sup>lt;sup>a</sup> The symbol '-' indicates that the parameters change according to different cases or are updated during the simulation.

<sup>&</sup>lt;sup>b</sup> The bold values are used as baseline parameters.

## 4.1. Effect of Streamwise Distance

To explore of effect of streamwise distance  $(d_x^*)$ , crossflow distance  $(d_y^*)$  is set to its baseline value, i.e.  $d_y^* = 0$ . Streamwise distances,  $d_x^* = 1, 2, 2.5, 2.6, 2.7, 2.8, 2.9, 3$  and 4, are examined in the study. Figure 4-1 shows the comparison of performance parameters,  $\overline{C_D}$ ,  $C_{L\,rms}$  and  $\overline{C_P}$  of the fish between undulation with and without rotation at different  $d_x^*$ . The scenario without the cylinder is included for the comparison.

The results for  $\overline{C_D}$  and  $C_{L\,rms}$  are categorized into two groups based on motion of the fish, undulation with or without rotation. Figure 4-1(a) shows negative values of  $\overline{C_D}$  for all cases of fish undulation only, except for  $d_x^* = 4$ . For fish undulation with rotation, the turning point is between  $d_x^* = 2.8$  and 2.9, in which negative  $\overline{C_D}$  obtained for  $d_x^* \leq 2.8$  and positive  $\overline{C_D}$  for  $d_x^* = 2.9$ , 3 & 4. There is a trend of decreasing  $\overline{C_D}$  from  $d_x^* = 2.9$  to 4. For both modes of motion, positive  $\overline{C_D}$  is shown in the scenario without the cylinder.

As depicted in Figure 4-1(b), same turning points as per  $\overline{C_D}$  exist for  $C_{L\,rms}$  in both modes of motion (i.e. undulation with and without rotation).  $C_{L\,rms}$  skyrockets from  $d_x^* = 3$  to 4 for undulation without rotation while it increases sharply from  $d_x^* = 2.9$  to 3 for undulation with rotation. All cases of both modes of motion show larger values of  $C_{L\,rms}$  than the scenario without the presence of the cylinder.

The results for  $\overline{C_P}$  are categorized in four groups, based on power consumption or extraction and undulation with or without rotation. As shown in Figure 4-1(c), coefficient of power consumption is always larger than coefficient of power extraction for all  $d_x^*$  regardless of mode of motion. It is also observed that the fish consume more power to undulate and rotate simultaneously than to undulate only for all  $d_x^*$ . Power consumption increases dramatically from  $d_x^* = 2.8$  to 2.9 when the fish is allowed undulation with rotation. Power extraction also shows an increasing trend across  $d_x^* = 2.8$  and 2.9 for fish undulation with rotation despite a smaller magnitude.

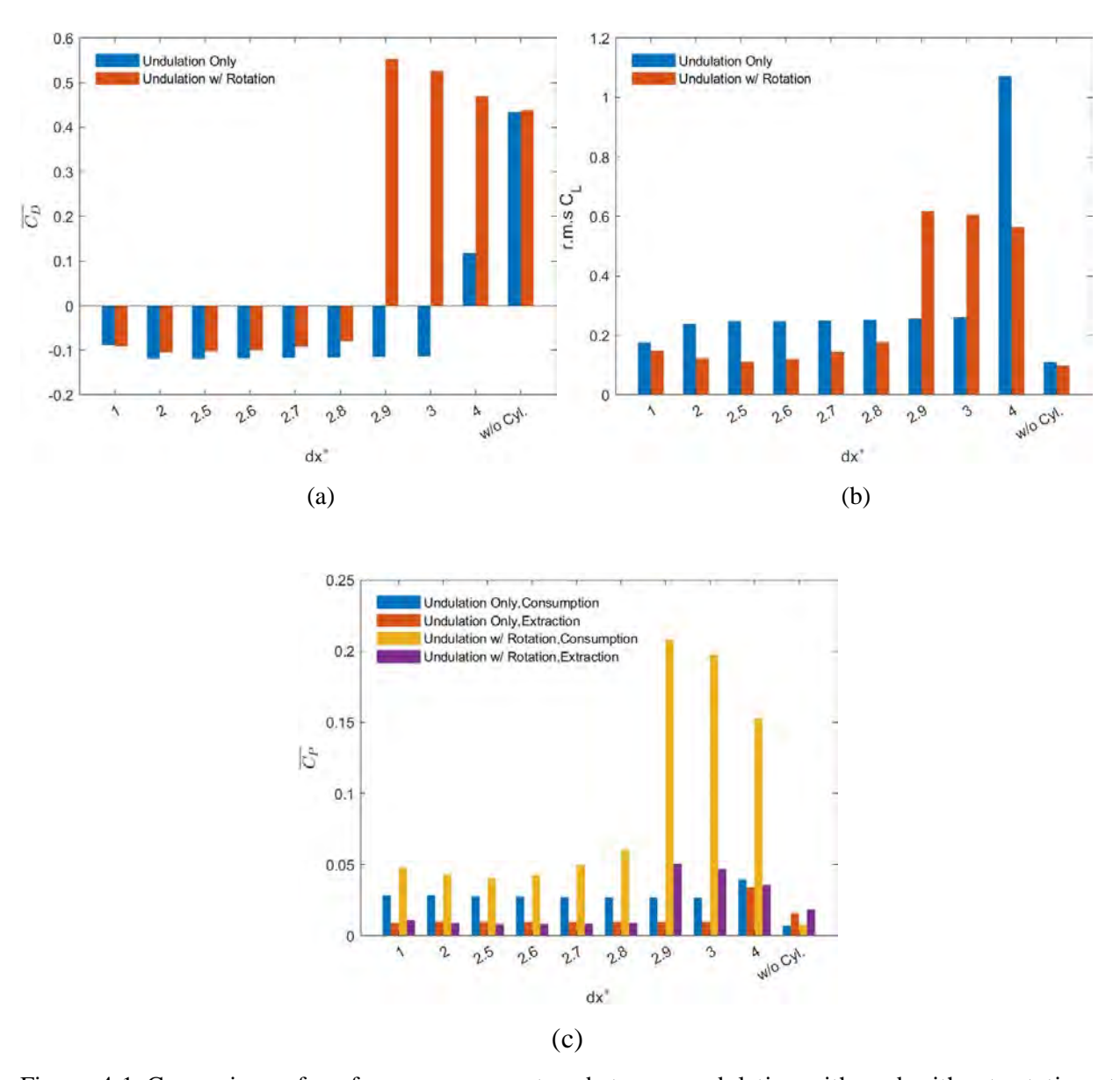


Figure 4-1 Comparison of performance parameters between undulation with and without rotation at different streamwise distances with the cylinder  $d_x^* = 1, 2, 2.5, 2.6, 2.7, 2.8, 2.9, 3 \& 4$  and without the presence of the cylinder: (a) time-averaged drag coefficient ( $\overline{C_D}$ ), (b) root-mean squared lift coefficient ( $C_{Lrms}$ ) and (c) time-averaged power coefficient ( $\overline{C_P}$ ) of the fish.

To understand the transition of performance parameters in two different modes of motion, it is necessary to investigate the flow structure around the fish and the cylinder at which the smallest and largest drag and the largest lateral force are experienced by the fish respectively. The transition occurred between  $d_x^* = 3$  and 4 for undulation without rotation is studied first.

Figure 4-2 shows the instantaneous vorticity contours with velocity field overlaid,  $C_D$  and  $C_L$  when the fish experiences the largest drag for both  $d_x^* = 3$  and 4. It clearly shows that vortex sheds from the cylinder significantly at  $d_x^* = 4$  while no significant vortex shedding is observed between the cylinder and the fish at  $d_x^* = 3$ . There is shedding of shear layers from both the upper and lower fish body at  $d_x^* = 4$  as shown in Figure 4-2(a2), which creates a pressure difference at the fish tail [see Figure 4-3(a2)]. Force towards downstream is produced at the fish tail as the result of the pressure difference as depicted in Figure 4-3(b2). On the other hand, the fish at  $d_x^* = 3$  locates at the suction zone of the cylinder, and thus benefits from thrust generated by the reverse flow in the zone. There is not much significant pressure difference across the fish body, except little at the posterior part [see Figure 4-3(a1)]. As a result, only small amount of lateral force is found at the posterior part of the fish as displayed in Figure 4-3(b1). These explain the fact that the value of the largest  $C_D$  for  $d_x^* = 3$  is lower than that for  $d_x^* = 4$ .

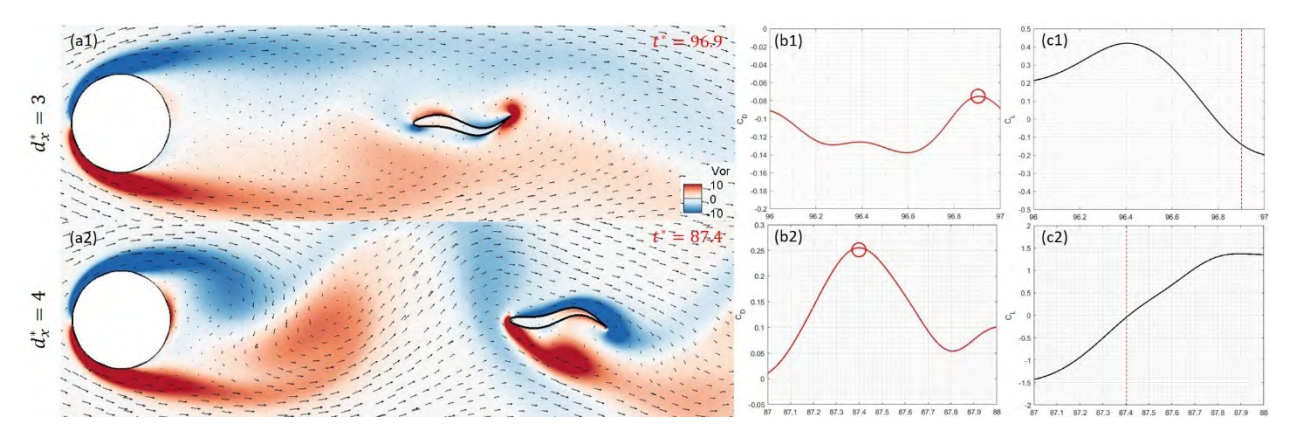


Figure 4-2 Instantaneous velocity field overlaid on vorticity contours (left), drag coefficient  $C_D$  (centre), and lift coefficient  $C_L$  (right) at the relevant time step when the fish body undulates only at  $d_{\chi}^* = 3$  and 4 respectively and experiences the largest  $C_D$ . Red circles and dash lines represent the corresponding  $C_D$  and  $C_L$  respectively at the relevant time steps for the largest  $C_D$ .

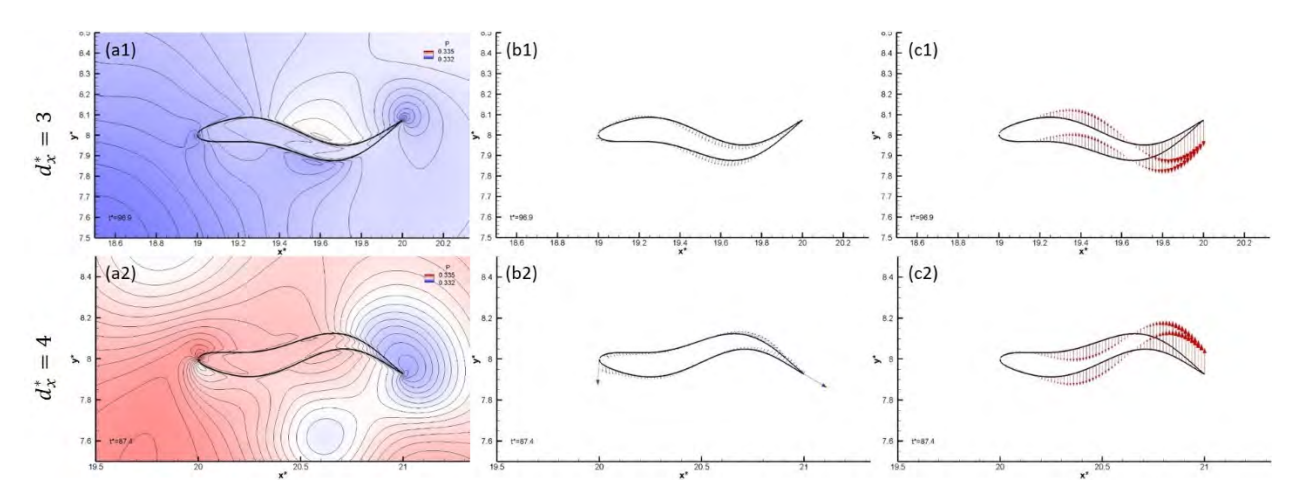


Figure 4-3 Pressure contours (left), force diagrams (centre) and velocity diagrams (right) along fish body boundary at the relevant time step when the fish body undulates only at  $d_x^* = 3$  and 4 and experiences the largest  $C_D$ .

Figure 4-4 shows the instantaneous vorticity contours with velocity field overlaid,  $C_D$  and  $C_L$  when the fish experiences the smallest drag for both  $d_x^* = 3$  and 4. The phenomenon of significant vortex shedding between the cylinder and the fish is only found in the case of  $d_x^* = 4$ , same as the study on the largest  $C_D$ . As we investigate the vorticity contour for the fish at  $d_x^* = 4$ , a pair of vortices is observed being shed from the upper posterior part of the fish [see Figure 4-4(a2)]. At the same time, separation of the shear layer from lower anterior part of the fish occurs. The combination of the separation of shear layer and the pair of vortices produces a significant pressure difference across the fish body [see Figure 4-5(a2)] in such a way that a large lateral force and a small thrust are obtained at the posterior part of the fish as depicted in Figure 4-5(b2). That is not the case for  $d_x^* = 3$ . The fish at  $d_x^* = 3$  locates at the suction zone of the cylinder. As shown in the vorticity contour for  $d_x^* = 3$  in Figure 4-4(a1), it is seen that the flow passing through the lower side of the cylinder rushes towards the lower posterior part of the fish. This creates a local pressure difference at the fish tail, and thus thrust is generated [see Figure 4-5(a1) and (b1) respectively]. These provide an explanation for more thrust obtained by the fish at  $d_x^* = 3$  than  $d_x^* = 4$ .

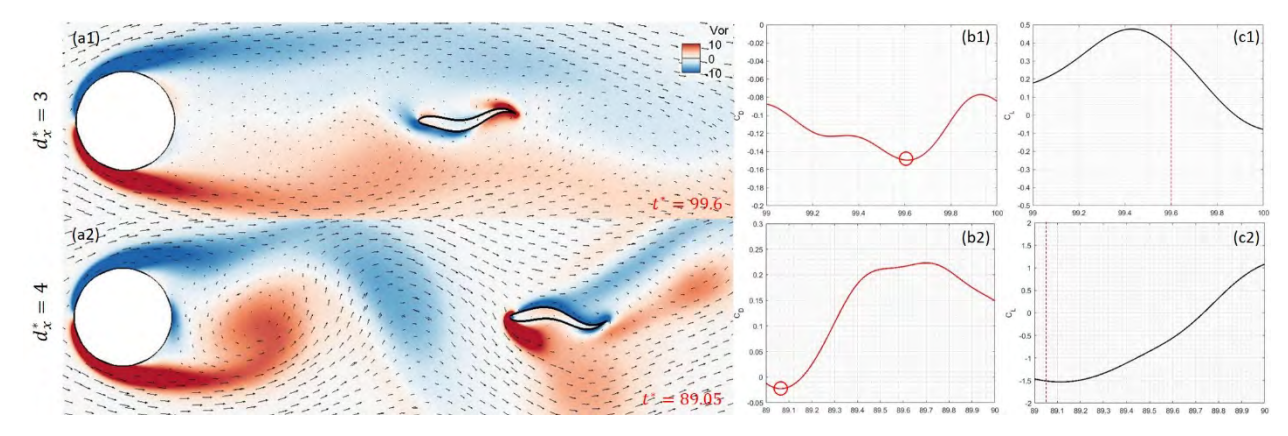


Figure 4-4 Instantaneous velocity field overlaid on vorticity contours (left), drag coefficient  $C_D$  (centre), and lift coefficient  $C_L$  (right) at the relevant time step when the fish body undulates only at  $d_x^* = 3$  and 4 respectively and experiences the smallest  $C_D$ . Red circles and dash lines represent the corresponding  $C_D$  and  $C_L$  respectively at the relevant time steps for the smallest  $C_D$ .

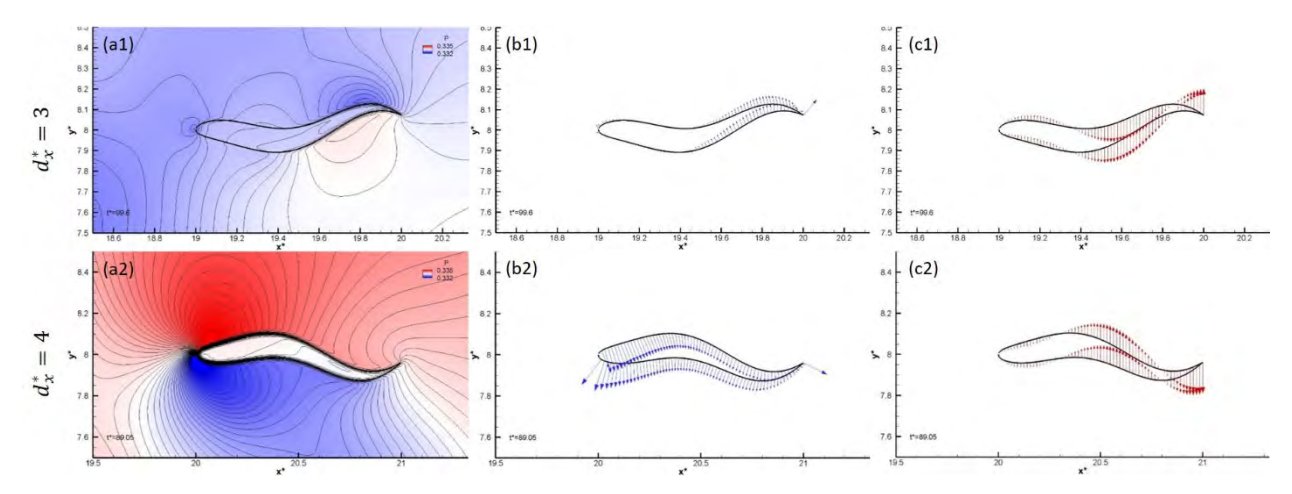


Figure 4-5 Pressure contours (left), force diagrams (centre) and velocity diagrams (right) along fish body boundary at the relevant time step when the fish body undulates only at  $d_x^* = 3$  and 4 and experiences the smallest  $C_D$ .

Figure 4-6 displays the instantaneous vorticity contours with velocity field overlaid,  $C_D$  and  $C_L$  when the fish experiences the largest lateral force for both  $d_x^* = 3$  and 4. The discrepancy of vortex shedding pattern between  $d_x^* = 3$  and 4 is similar to that of the studies regarding the largest and smallest drag experienced by the fish. As revealed in Figure 4-6(a2), a pair of vortices sheds from the upper posterior part of the fish. Together with the separation of the shear layer from underneath the anterior part of the fish, a strong pressure difference is formed across the fish body as shown in Figure 4-7(a2). This pressure difference produces a large lateral force and a small

amount of thrust on the fish [see Figure 4-7(b2)]. For  $d_x^* = 3$ , the fish is beneficial from the reverse flow inside the suction zone established by the vortex shedding from the cylinder. The flow underneath the cylinder travels downstream and becomes a vortical flow towards the lower posterior part of the fish as depicted by Figure 4-6(a1). A local pressure difference is formed near the fish tail as exhibited in Figure 4-7(a1) due to the vortical flow. Thus, the lateral force is found locally at the posterior part of the fish. However, this force is located only at the anterior part instead of the whole fish body at  $d_x^* = 4$ . This provides an explanation to a higher magnitude of  $C_L$  for  $d_x^* = 4$  than 3.

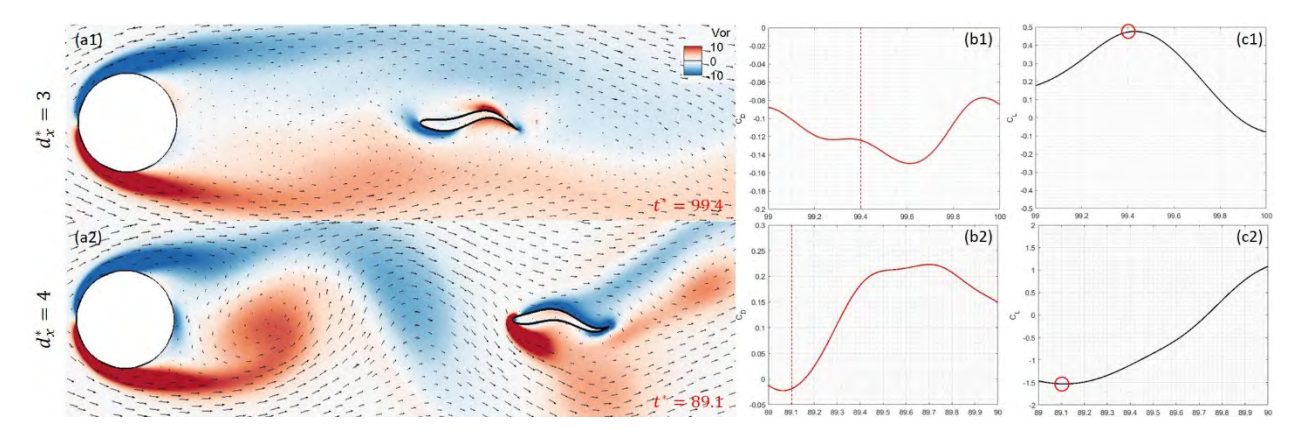


Figure 4-6 Instantaneous velocity field overlaid on vorticity contours (left), drag coefficient  $C_D$  (centre), and lift coefficient  $C_L$  (right) at the relevant time step when the fish body undulates only at  $d_{\chi}^* = 3$  and 4 respectively and experiences the largest magnitude of  $C_L$ . Red dash lines and circles represent the corresponding  $C_D$  and  $C_L$  respectively at the relevant time steps for the largest magnitude of  $C_L$ .

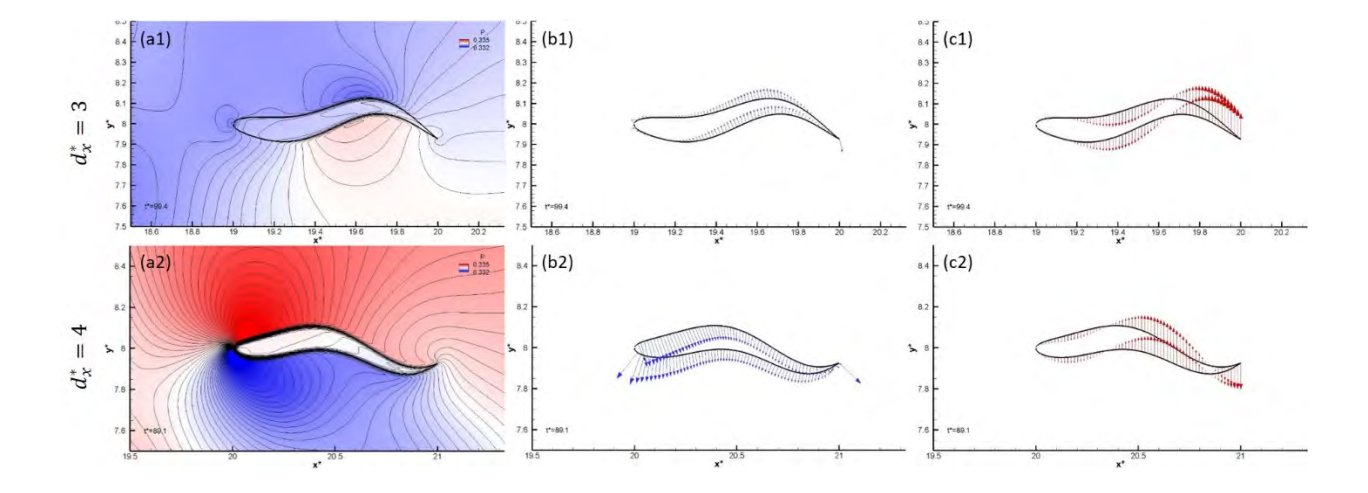


Figure 4-7 Pressure contours (left), force diagrams (centre) and velocity diagrams (right) along fish body boundary at the relevant time step when the fish body undulates only at  $d_x^* = 3$  and 4 and experiences the largest magnitude of  $C_L$ .

After the investigation on the transition occurred between  $d_x^* = 3$  and 4 for undulation without rotation, the study on the transition between  $d_x^* = 2.8$  and 2.9 for undulation with rotation is conducted. Figure 4-8 shows vorticity contours with velocity field overlaid for fish undulation with rotation at different  $d_x^*$  at the same time step. It uncovers an interesting finding in which a discrepancy in the location of vortex shedding exists. For  $d_x^* \le 2.8$ , significant vortex shedding happens downstream of the fish. In contrast, significant vortex shedding occurs between the cylinder and the fish for  $d_x^* \ge 2.9$ . To reveal effects of this discrepancy on the transition of performance parameters across  $d_x^* = 2.8$  and 2.9, detailed investigation is carried out at the time steps which the smallest and largest drag and the largest lateral force are experienced by the fish respectively.

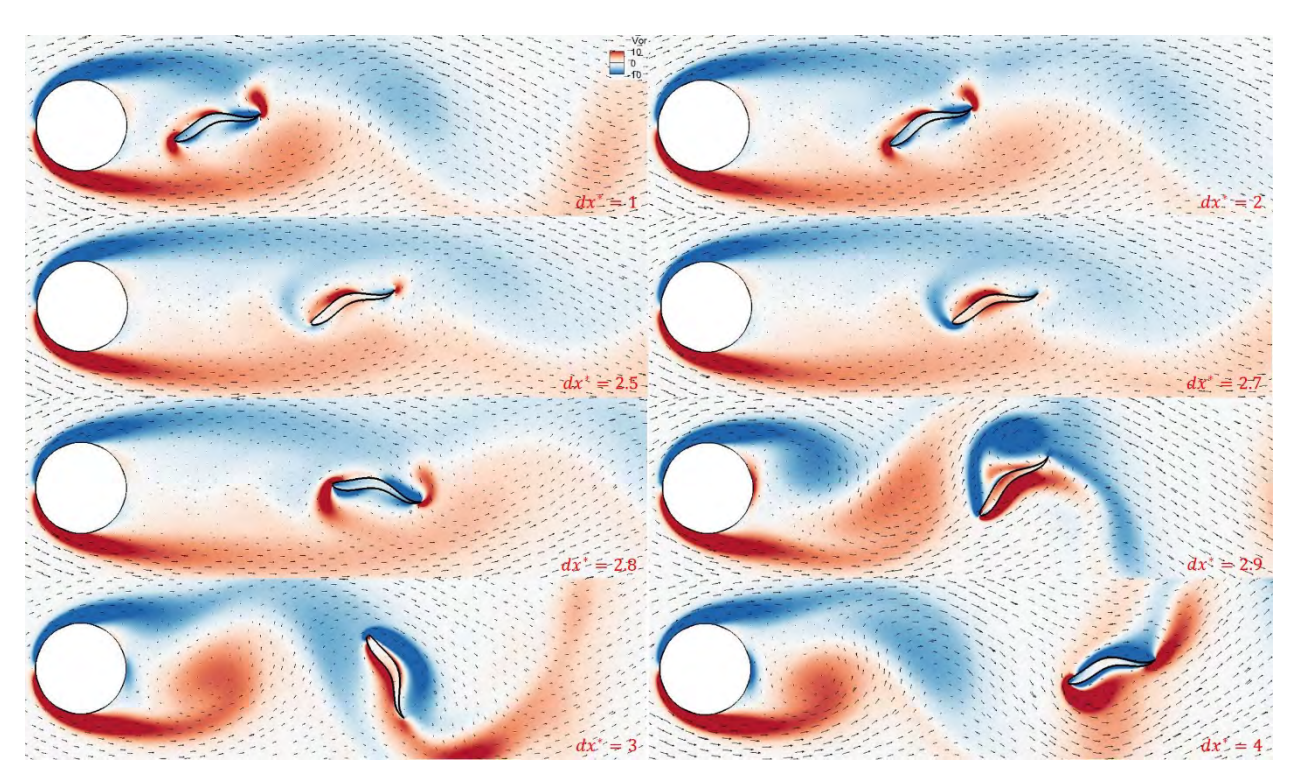


Figure 4-8 Comparison of vorticity contours with instantaneous velocity field overlaid for fish undulation with rotation at different streamwise distances with the cylinder  $d_x^* = 1, 2, 2.5, 2.6, 2.7, 2.8, 2.9, 3 & 4$  at the same time step.

Figure 4-9 shows the instantaneous vorticity contours with velocity field overlaid,  $C_D$ ,  $C_L$  and angle of rotation about the centroid at relevant time steps when the fish experiences the largest drag for both  $d_x^* = 2.8$  and 2.9. It is clearly seen that the fish interacts strongly with the vortex shed from the cylinder for  $d_x^* = 2.9$ . The vortical flow impacts on the anterior part of the fish and causes the fish to rotate vigorously [i.e.  $\theta \sim 65^\circ$  as shown in Figure 4-9(d2)]. The angle of rotation is large enough to create the separation of shear layer from the upper fish as shown in Figure 4-9(a2). Therefore, a significant pressure difference occurs across the fish body [see Figure 4-10(a2)] and large force vectors titled downstream are observed in Figure 4-9(b2). This implies a strong drag created on the fish at  $d_x^* = 2.9$  [i.e.  $C_D \sim 1.5$  in Figure 4-9(b2)].

In contrast, no significant vortex is observed between the cylinder and the fish at  $d_x^* = 2.8$  as aforementioned. The flow velocity in between the cylinder and the fish is sufficiently low to create a suction zone in which reverse flow is observed at posterior part and downstream of the fish [see Figure 4-9(a1)]. The reverse flow impacts the fish body and somehow causes the separation of shear layers from the fish head and tail when it rotates about its centroid. As a result, a small local pressure difference is noticed at the fish head and tail [see Figure 4-10(a1)] which produces a small amount of thrust at the anterior part of the fish as depicted in Figure 4-10(b1). That corresponds to the small negative value of  $C_D$  for  $d_x^* = 2.8$  [i.e.  $C_D \sim -0.01$  in Figure 4-9(b1)].

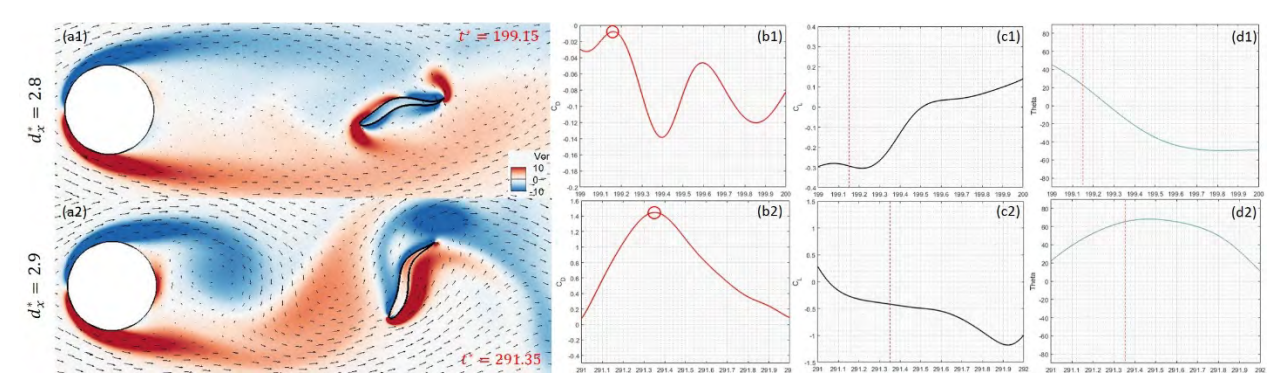


Figure 4-9 Instantaneous velocity field overlaid on vorticity contours (left), drag coefficient  $C_D$  (centre left), lift coefficient  $C_L$  (centre right) and angle of rotation about centroid  $\theta$  (right) at the relevant time step when the fish body undulates and rotates at  $d_x^* = 2.8$  and 2.9 respectively and experiences the largest  $C_D$ . Positive angle of rotation represents anticlockwise rotation while negative angle represents clockwise

rotation. Red circles and dash lines represent the corresponding  $C_D$ ,  $C_L$  and  $\theta$  respectively at the relevant time steps for the largest  $C_D$ .

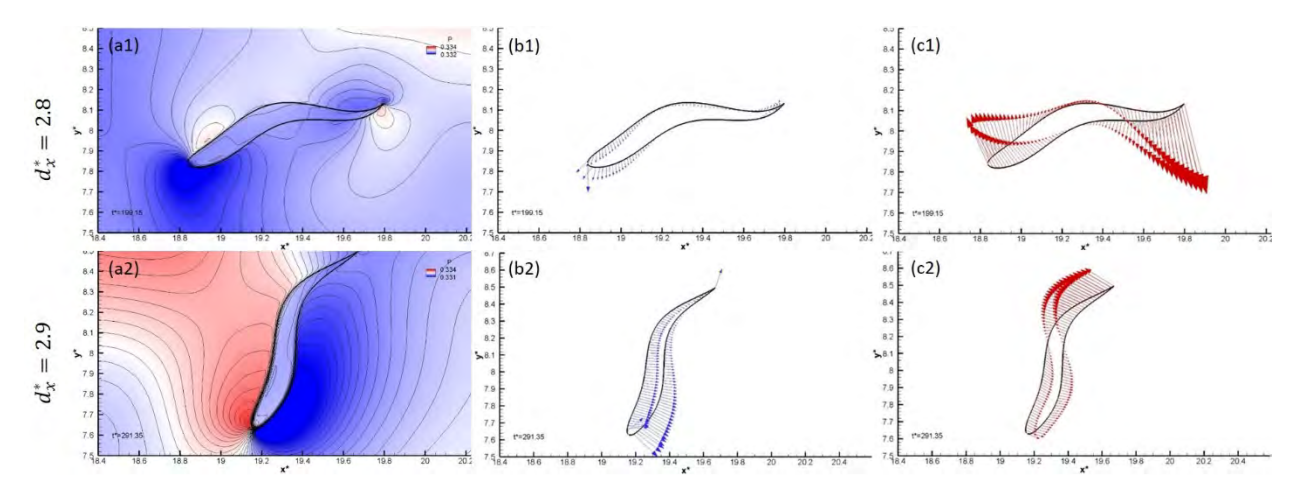


Figure 4-10 Pressure contours (left), force diagrams (centre) and velocity diagrams (right) along fish body boundary at the relevant time step when the fish body undulates and rotates at  $d_x^* = 2.8$  and 2.9 and experiences the largest  $C_D$ .

Figure 4-11 displays the instantaneous vorticity contours with velocity field overlaid,  $C_D$ ,  $C_L$  and angle of rotation about the centroid at relevant time steps when the fish experiences the smallest drag for both  $d_x^* = 2.8$  and 2.9. It is noticed that both fish have the same value of the lowest  $C_D$  [i.e.  $C_D \sim -0.19$  as shown in Figure 4-9(b1) and (b2)]. Although they have the same body shape (i.e. "C" shape), the flow structures around them are different. The interaction with vortices shed from the cylinder is strong for the fish at  $d_x^* = 2.9$  while the fish at  $d_x^* = 2.8$  is inside the suction zone as revealed in Figure 4-11(b1) and (a1) respectively. The strong vortical flow approaches the anterior part of the fish at  $d_x^* = 2.9$  with a large angle of attack which causes the flow separation [see Figure 4-11(b1) for separation of shear layer from upper fish body]. This produces significant local pressure difference at the fish head and tail as shown in Figure 4-12(b1). Therefore, a large lateral force is formed at the anterior part and a small amount of thrust is generated at the posterior of the fish [see Figure 4-12(b2)].

For the fish at  $d_x^* = 2.8$ , the flow velocity in the suction zone is low in which reverse flow is observed at both lower anterior and posterior parts of the fish [see Figure 4-11(a1)]. The reverse flow impacts the fish body and causes the separation of shear layers from the fish head and tail

when it rotates. Therefore, a small local pressure difference is noticed at the anterior and posterior parts of the fish. [see Figure 4-12(a1)] which generates a small amount of thrust as depicted in Figure 4-12(b1).

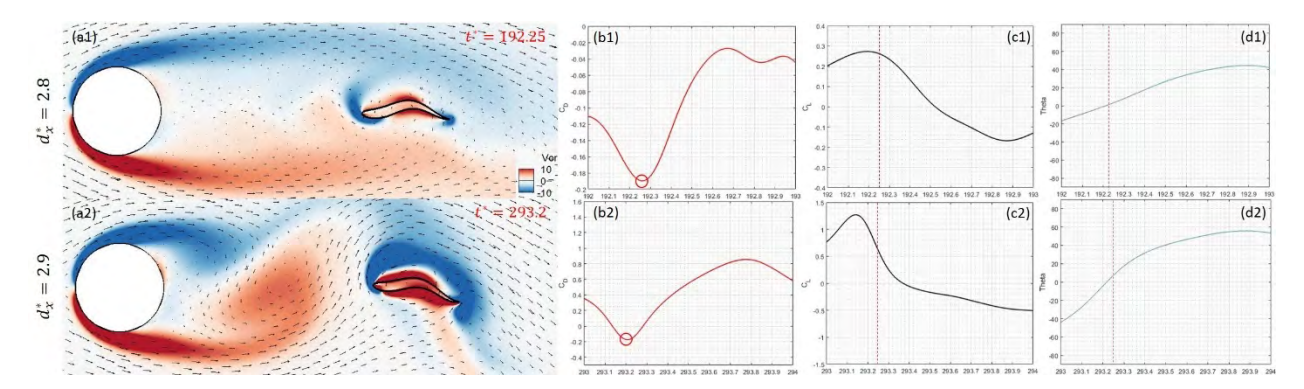


Figure 4-11 Instantaneous velocity field overlaid on vorticity contours (left), drag coefficient  $C_D$  (centre left), lift coefficient  $C_L$  (centre right) and angle of rotation about centroid  $\theta$  (right) at the relevant time step when the fish body undulates and rotates at  $d_x^* = 2.8$  and 2.9 respectively and experiences the smallest  $C_D$ . Red circles and dash lines represent the corresponding  $C_D$ ,  $C_L$  and  $\theta$  respectively at the relevant time steps for the smallest  $C_D$ .

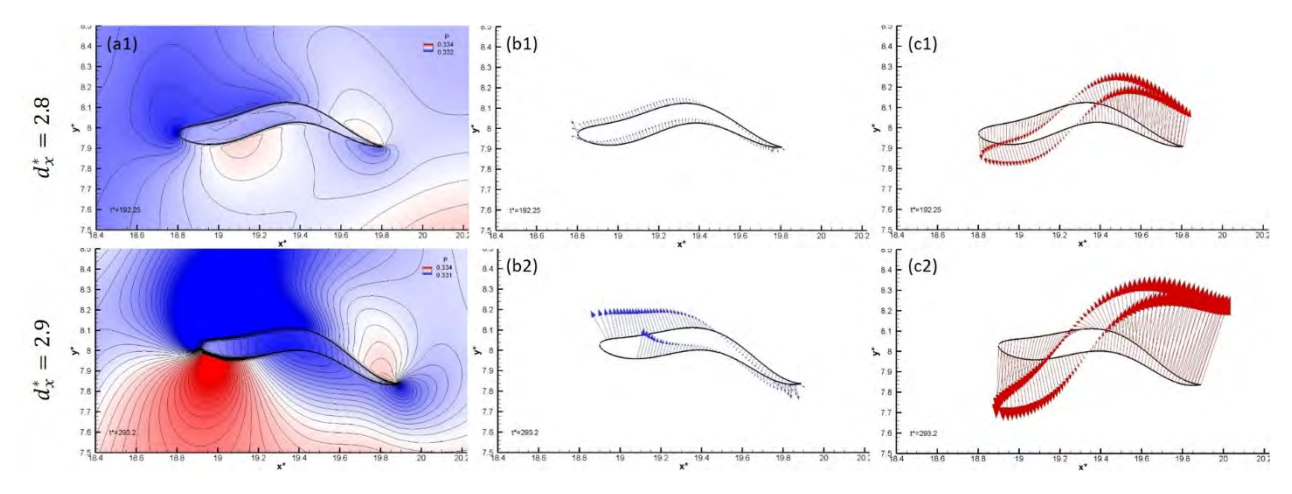


Figure 4-12 Pressure contours (left), force diagrams (centre) and velocity diagrams (right) along fish body boundary at the relevant time step when the fish body undulates and rotates at  $d_x^* = 2.8$  and 2.9 and experiences the smallest  $C_D$ .

Figure 4-13 shows the instantaneous vorticity contours with velocity field overlaid,  $C_D$ ,  $C_L$  and angle of rotation about the centroid at relevant time steps when the fish experiences the largest

magnitude of lateral force for both  $d_x^* = 2.8$  and 2.9. As outlined in the previous study on the largest and smallest drag, vortex shedding from the cylinder is more noticeable for  $d_x^* = 2.9$ . The vortical flow downstream of the cylinder approaches the upper anterior part of the fish and forms an angle of attack with the cord of the fish The angle is larger enough to cause the separation of flow from the upper fish body as shown in Figure 4-13(a2). Hence, a noticeable pressure difference occurs at the fish head [see Figure 4-14(a2)]. As the fish body is of a "C" shape at that moment and the anterior part of the fish is parallel to the streamwise direction [see Figure 4-13(a2)], most forces exerted on the anterior part of the fish are normal to the body as depicted in Figure 4-14(b2). This implies the large lateral force on the fish and thus corresponds to the largest magnitude of lateral force as indicated in Figure 4-13(c2).

On the other hand, the reverse flow is observed on the upper fish body at  $d_x^* = 2.8$  [see Figure 4-13(a1)]. The reverse flow in combination with the rotation about the fish centroid contributes to the separation of shear layers and thus local pressure differences across mid-body and tail of the fish as depicted in Figure 4-14(a1). These pressure differences create forces at mid-body and posterior part of the fish whereof lateral force is found at mid-body [see Figure 4-14(b1)]. However, the magnitude of this lateral force is not as large as that for  $d_x^* = 2.9$ . This corresponds to the smaller  $C_L$  for  $d_x^* = 2.8$  than 2.9 as shown in Figure 4-13(c1) and (c2).

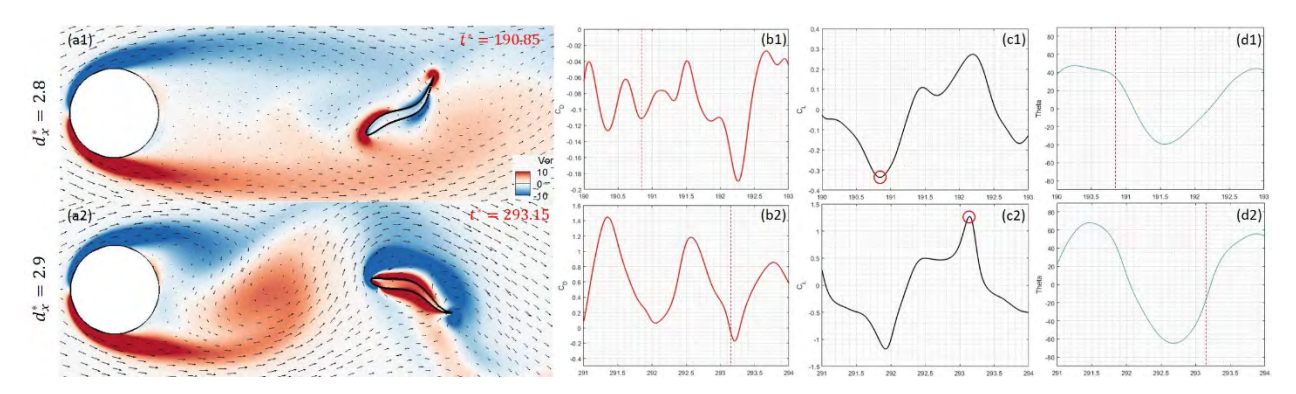


Figure 4-13 Instantaneous velocity field overlaid on vorticity contours (left), drag coefficient  $C_D$  (centre left), lift coefficient  $C_L$  (centre right) and angle of rotation about centroid  $\theta$  (right) at the relevant time step when the fish body undulates and rotates at  $d_{\chi}^* = 2.8$  and 2.9 respectively and experiences the largest magnitude of  $C_L$ . Red circles and dash lines represent the corresponding  $C_D$ ,  $C_L$  and  $\theta$  at the relevant time steps for the largest magnitude of  $C_L$ .

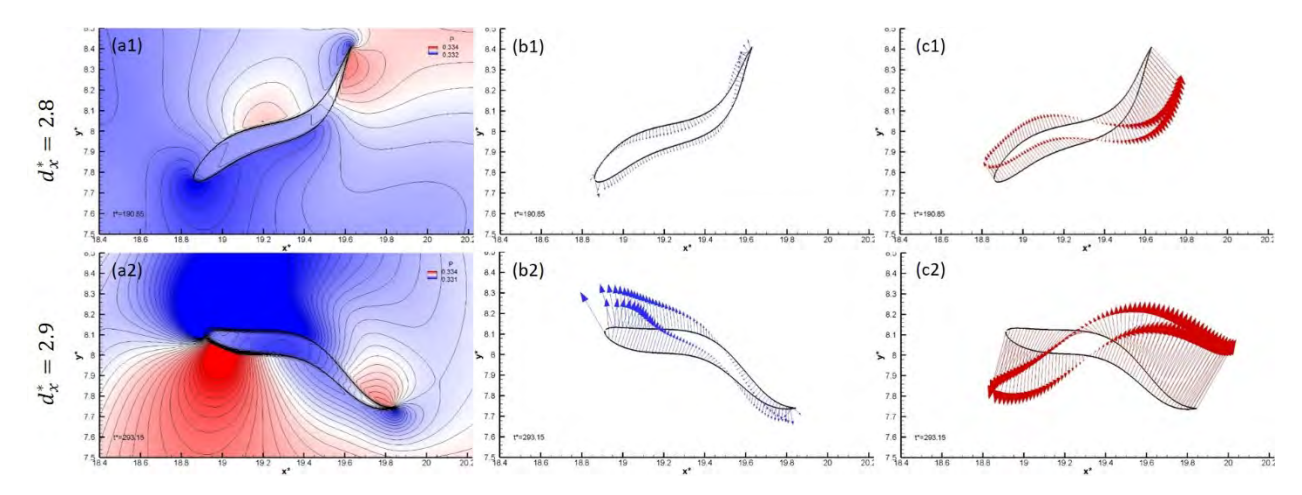


Figure 4-14 Pressure contours (left), force diagrams (centre) and velocity diagrams (right) along fish body boundary at the relevant time step when the fish body undulates and rotates at  $d_x^* = 2.8$  and 2.9 and experiences the largest magnitude of  $C_L$ .

From the studies on the largest and smallest drag and the largest lateral force experienced by the fish, we can make a small conclusion on the discrepancy between  $d_x^* = 2.8$  and 2.9. For fish undulation with rotation at  $d_x^* = 2.8$ , the angle of rotation is normally within  $\pm 50^\circ$ . There is no obvious vortex between the cylinder and the fish so the magnitude of force, both longitudinal and lateral, is smaller. For the fish at  $d_x^* = 2.9$ , the angle of rotation varies from  $-70^\circ$  to  $70^\circ$ , which is more vigorous than that for  $d_x^* = 2.8$ . Vortex shedding between the cylinder and the fish is significant most of the time. Therefore, it is common to observe large drag on the fish body when the angle of rotation exceeds  $\pm 50^\circ$ .

To summarize, the transition from thrust generated to drag experienced by the fish happens for both undulation with and without rotation. The transition occurs in between  $d_x^* = 3$  and 4 for undulation without rotation while  $d_x^* = 2.8$  and 2.9 for undulation with rotation. The discrepancy in terms of longitudinal force experienced by the fish is mainly due to the existence of vortex shedding between the cylinder and the fish.

## 4.2. Effect of Crossflow Distance

Crossflow distance  $(d_y^*)$  also affects the performance of the fish undulation with rotation. To explore its effect, streamwise distance  $(d_x^*)$  is set to its baseline value, i.e.  $d_x^* = 2$ . Crossflow

distances,  $d_y^* = 0$ , 0.1, 0.2, 0.3, 0.4, 0.5, 1, 2 and 3, are examined in the study. Figure 4-15 shows the comparison of performance parameters,  $\overline{C_D}$ ,  $C_{L\,rms}$  and  $\overline{C_P}$  of the fish between undulation with and without rotation at different  $d_y^*$ . The scenario without the cylinder is included for the comparison.

The results for  $\overline{C_D}$  and  $C_{L\,rms}$  are categorized into two groups based on motion of the fish, undulation with or without rotation. The results for  $\overline{C_P}$  are categorized in four groups, based on power consumption or extraction and undulation with or without rotation. In Figure 4-15, we can see that the results for undulation with rotation from  $d_y^* = 0.1$  to 0.4 are missing. It is because of the excessive rotation about the fish centroid when the fish is positioned at  $d_y^* = 0.1, 0.2, 0.3$  and 0.4. The details could be further revealed by analysing the flow structure around the cylinder and the fish.

For fish undulation without rotation, negative  $\overline{C_D}$  are recorded for  $d_y^* \leq 0.3$  while positive  $\overline{C_D}$  for  $d_y^* \geq 0.4$ . The increasing trend from  $d_y^* = 0$  to 1 is gradual as shown in Figure 4-15(a). The placement of the cylinder upstream of the fish could effectively reduce the drag of the fish at  $d_y^* \leq 1$  in comparison with the scenario without the presence of the cylinder. For fish undulation with rotation, it is believed that the fish at  $d_y^* = 0$  is the most beneficial case in terms of drag reduction though data could not be obtained between  $d_y^* = 0.1$  and 0.4.

As shown in Figure 4-15(b), for fish undulation only, the largest  $C_{L\,rms}$  among all cases is at  $d_y^* = 1$ . Similar values are recorded from  $d_y^* = 0$  to 0.5 with a peak at  $d_y^* = 0.3$ .  $C_{L\,rms}$  decreases gradually with  $d_y^*$  from  $d_y^* = 1$ . For fish undulation with rotation, with the available data, it is observed that  $C_{L\,rms}$  for  $d_y^* = 0$  is similar to the scenario without the cylinder.

In figure 4-15(c), it is noticed that power of consumption is always larger than power of extraction from  $d_y^* = 0$  to 0.5 whether the fish is allowed to rotate or not, provided that data for undulation with rotation is not available for  $d_y^* = 0.1, 0.2, 0.3 \& 0.4$ . In contrast, power consumption is smaller than extraction for  $d_y^* \ge 1$  and the scenario without the presence of the cylinder. It is

notable that power consumption is large for  $d_y^* = 0 \& 0.5$  when the fish undulates and rotates. It is believed that vortex shedding and fish rotation influence energy consumption positively when the fish is placed laterally closer to the centre of the cylinder.

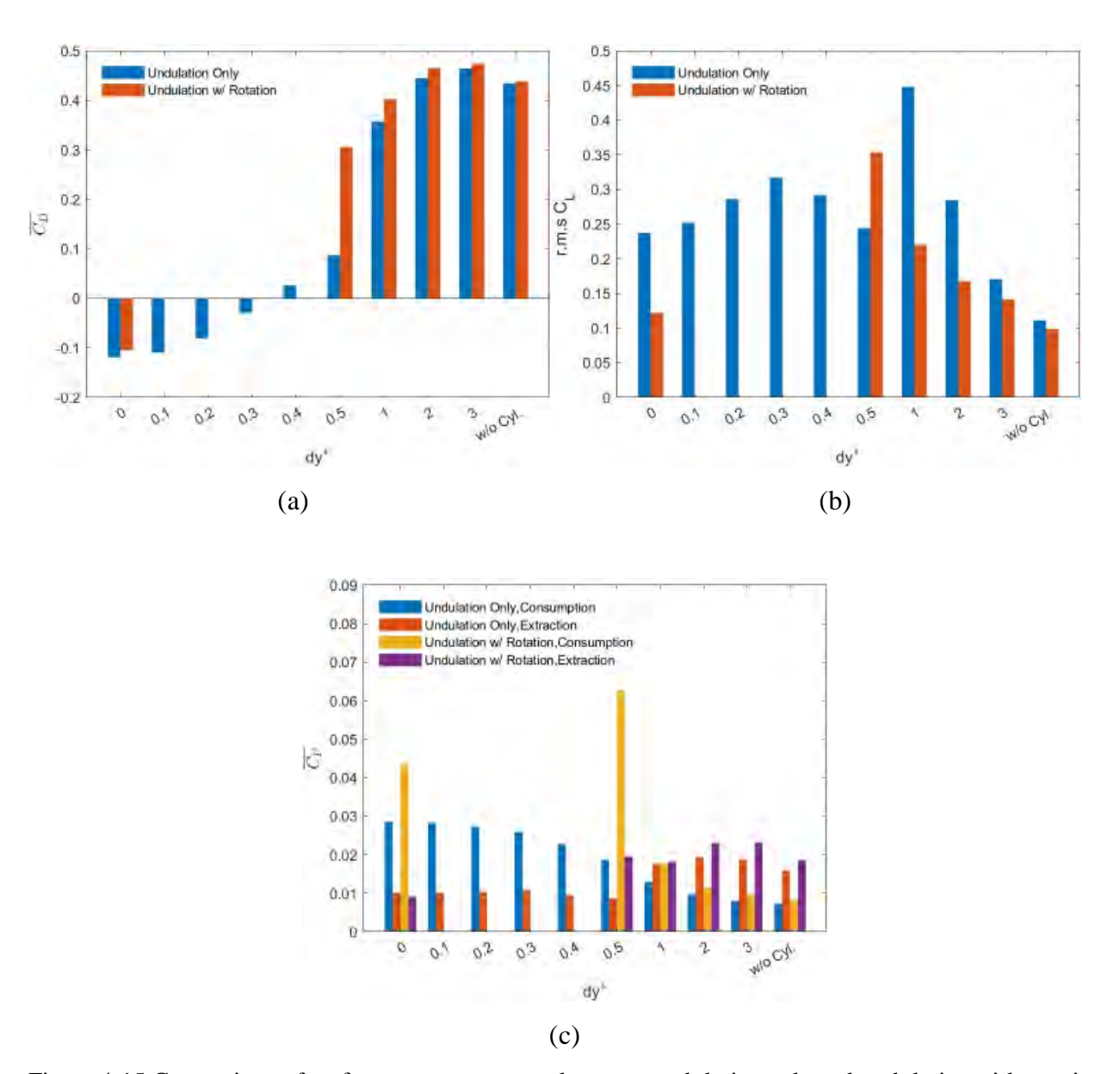


Figure 4-15 Comparison of performance parameters between undulation only and undulation with rotation at crossflow distance with the cylinder  $d_y^* = 0$ , 0.1, 0.2, 0.3, 0.4, 0.5, 1, 2 & 3 and without the presence of the cylinder: (a) time-averaged drag coefficient ( $\overline{C_D}$ ), (b) root-mean squared lift coefficient ( $C_{Lrms}$ ) and (c) time-averaged power coefficient ( $\overline{C_P}$ ) of the fish.

To understand the reason behind the missing data from  $d_y^* = 0.1, 0.2, 0.3 \& 0.4$ , the flow structure around the cylinder and the fish is analysed. The cases of  $d_y^* = 0 \& 0.5$  are first studied to show fish rotation within normal range which enables performance data to be recorded. After that, it is followed by studies on  $d_y^* = 0.1, 0.2, 0.3 \& 0.4$ .

Figure 4-16 shows the instantaneous velocity field overlaid on vorticity contours, velocity diagrams along fish body boundary and angle of rotation about centroid at several time steps between  $t^* = 90.85$  and 92.75 when the fish undulates and rotates at  $d_v^* = 0$ . As we can see, the centroid of the fish aligns longitudinally with the centre of the cylinder. Vortex shedding between the cylinder and the fish is not as strong as in other cases. The vortical flow mostly meets the anterior part of the fish at the first instance. It influences the velocity of the fish tail in the sense that affects the rotation. When the fish body is parallel to the free-stream flow (i.e. angle of rotation  $\theta = 0^{\circ}$ ), the vortical flow acts at the anterior part of the fish body [see Figure 4-16(a2) and (a4)] and creates the tendency of rotation about the fish centroid. The velocity vectors at the anterior part are in the opposite direction of those at the posterior part of the fish [see Figure 4-16(b2) and (b4)]. This "velocity couple" further enhances the rotation about the centroid. When this fish rotates to an angle of either  $+50^{\circ}$  or  $-40^{\circ}$  as demonstrated in Figure 4-16(a1) and (a3) respectively, large velocity vectors are observed at the posterior part of the fish with the opposite sense to the rotation [see Figure 4-16(b1) and (b3)]. This suppresses the further rotation and tries to get the fish back to its equilibrium position (i.e. angle of rotation  $\theta = 0^{\circ}$ ). As shown in Figure 4-17(b1) and (b3), forces of small magnitude are exerted on the posterior part of the fish. These force vectors are opposite to those velocity vectors on that part as depicted in Figure 4-16(b1) and (b3). As the fish consumes energy to act against force exerted by the flow, this explains the reason behind the large power consumption for  $d_y^* = 0$  in Figure 4-15(c). The fish maintains the stable and continuous rotation about its centroid in the range of  $-40^{\circ}$  to  $+50^{\circ}$  as displayed in Figure 4-17(c1-c4).

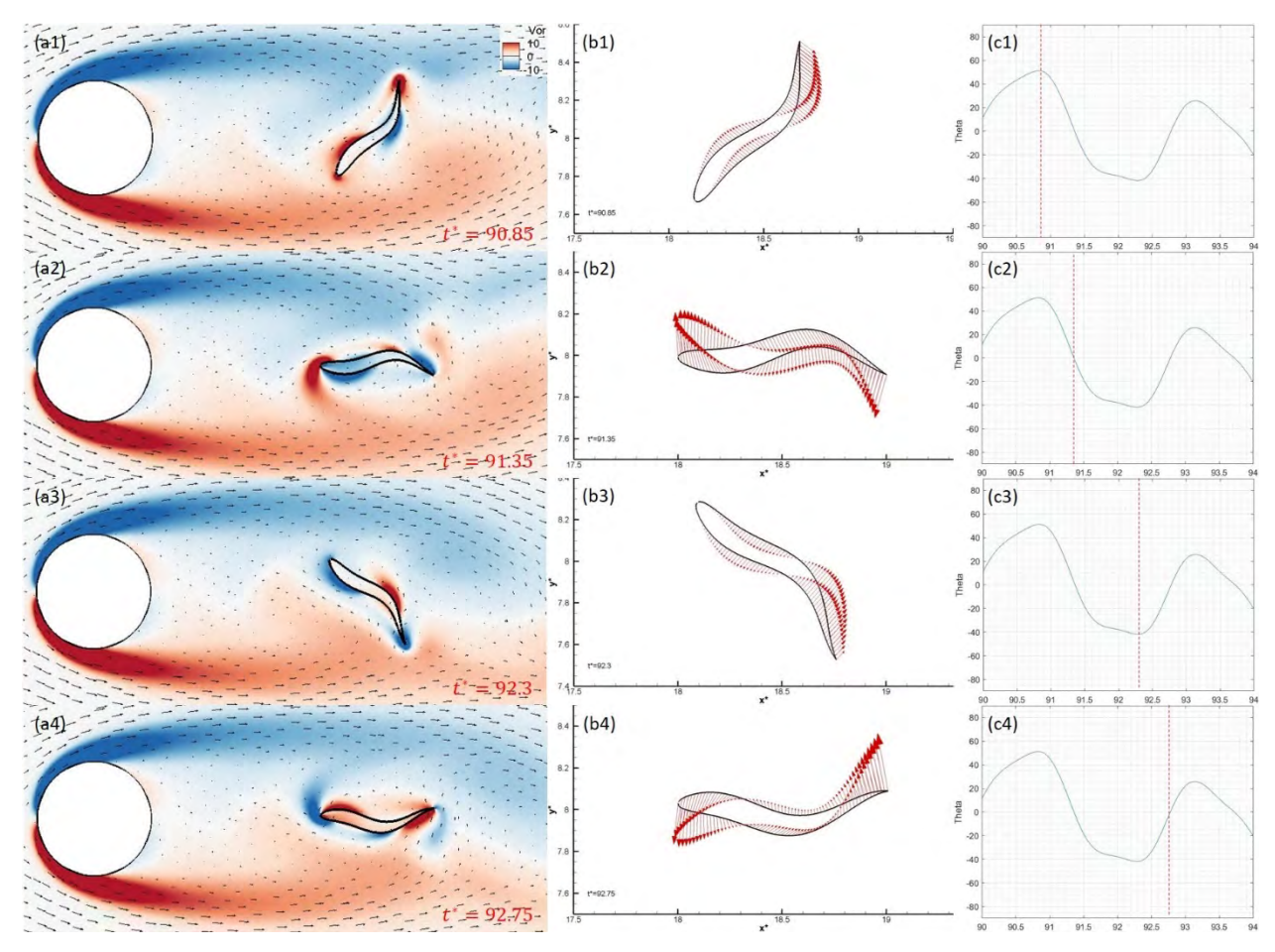


Figure 4-16 Instantaneous velocity field overlaid on vorticity contours (left), velocity diagrams along fish body boundary (centre) and angle of rotation about centroid  $\theta$  (right) at time steps  $t^* = 90.85, 91.35, 92.2 \& 92.75$  when the fish body undulates and rotates at  $d_y^* = 0$ . Red dash lines represent the corresponding  $\theta$  at the relevant time steps.

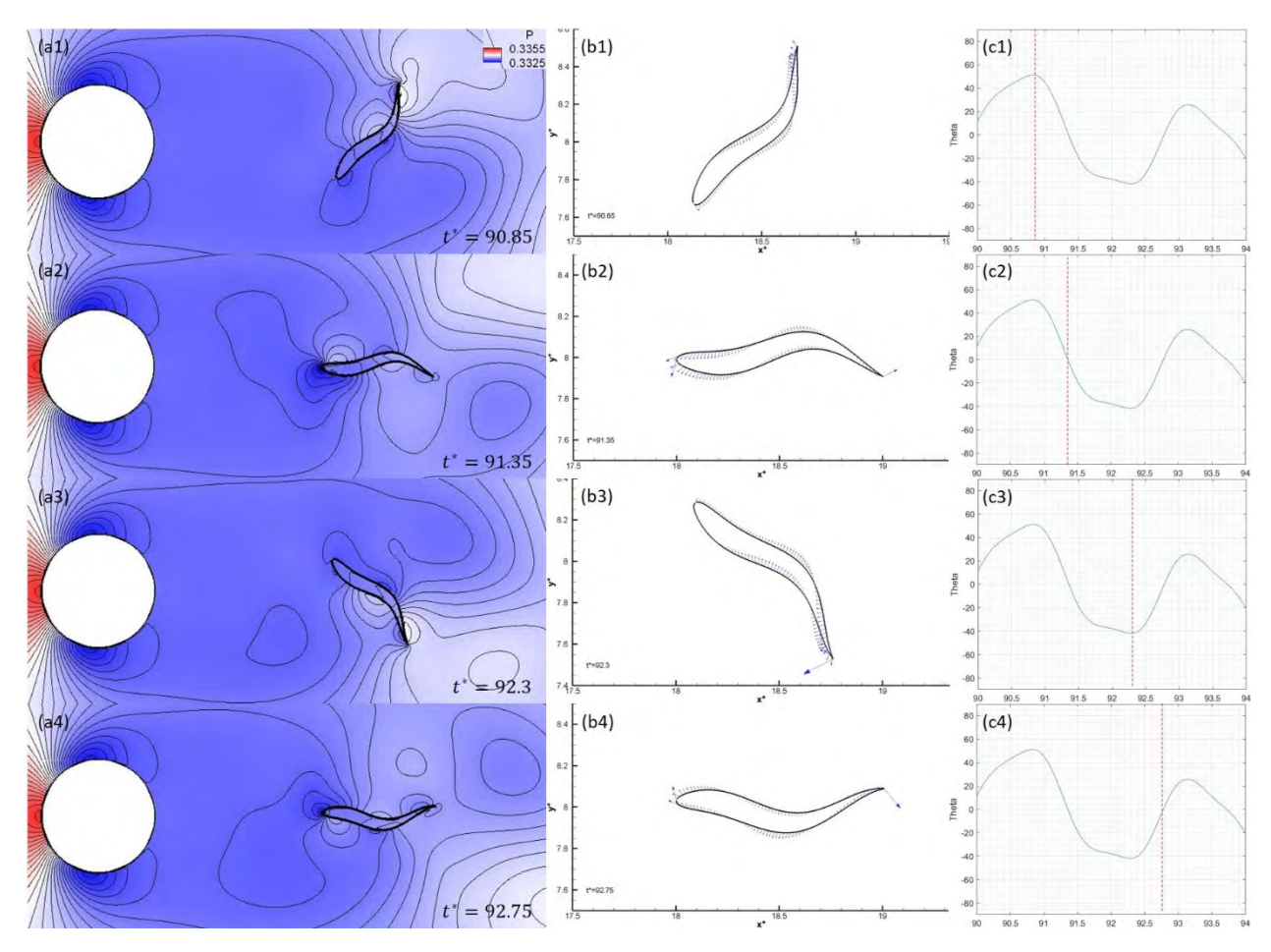


Figure 4-17 Pressure contours (left), force diagrams along fish body boundary (centre) and angle of rotation about centroid  $\theta$  (right) at time steps  $t^* = 90.85, 91.35, 92.3 \& 92.75$  when the fish body undulates and rotates at  $d_v^* = 0$ . Red dash lines represent the corresponding  $\theta$  at the relevant time steps.

According to the vorticity contours in Figure 4-18, the centroid of the fish aligns longitudinally with the shed shear layer from the cylinder for  $d_y^* = 0.5$ . Vortex shedding from the cylinder is obvious throughout the whole tail-beat cycle. These vortices influence the fish significantly by causing separation of shear layers from the fish body boundary. When the fish body is parallel to the freestream flow (i.e.  $t^* = 91.85 \& 92.85$ ), it is clearly seen that large velocity vectors occur at both anterior and posterior parts of the fish which are opposite to each other [see Figure 4-18(b1) and (b3)]. These opposite velocity vectors cause the rotation about the fish centroid. At the same time, vortical flow approaches the anterior and posterior parts in an opposite direction to the body boundary (i.e. velocity vectors on the fish body boundary) as depicted in Figure 4-18(a1) and (a3). Therefore, significant pressure difference is observed across the fish body [see Figure 4-19(a1)

and (a3)] which creates force vectors against velocity vectors on the fish boundary [see Figure 4-19(b1) and (b3)]. As the fish consumes energy to withstand the force exerted by the flow, this explains the reason behind the exceptionally large power consumption in Figure 4-15(c). The fish is observed to maintain the stable rotation about its centroid within the range of  $\pm 50^{\circ}$  as demonstrated in Figure 4-19(c1-c4). Unless its head is perpendicular to the shed shear layer from the cylinder, the fish would not be overturned by the vortical flow.

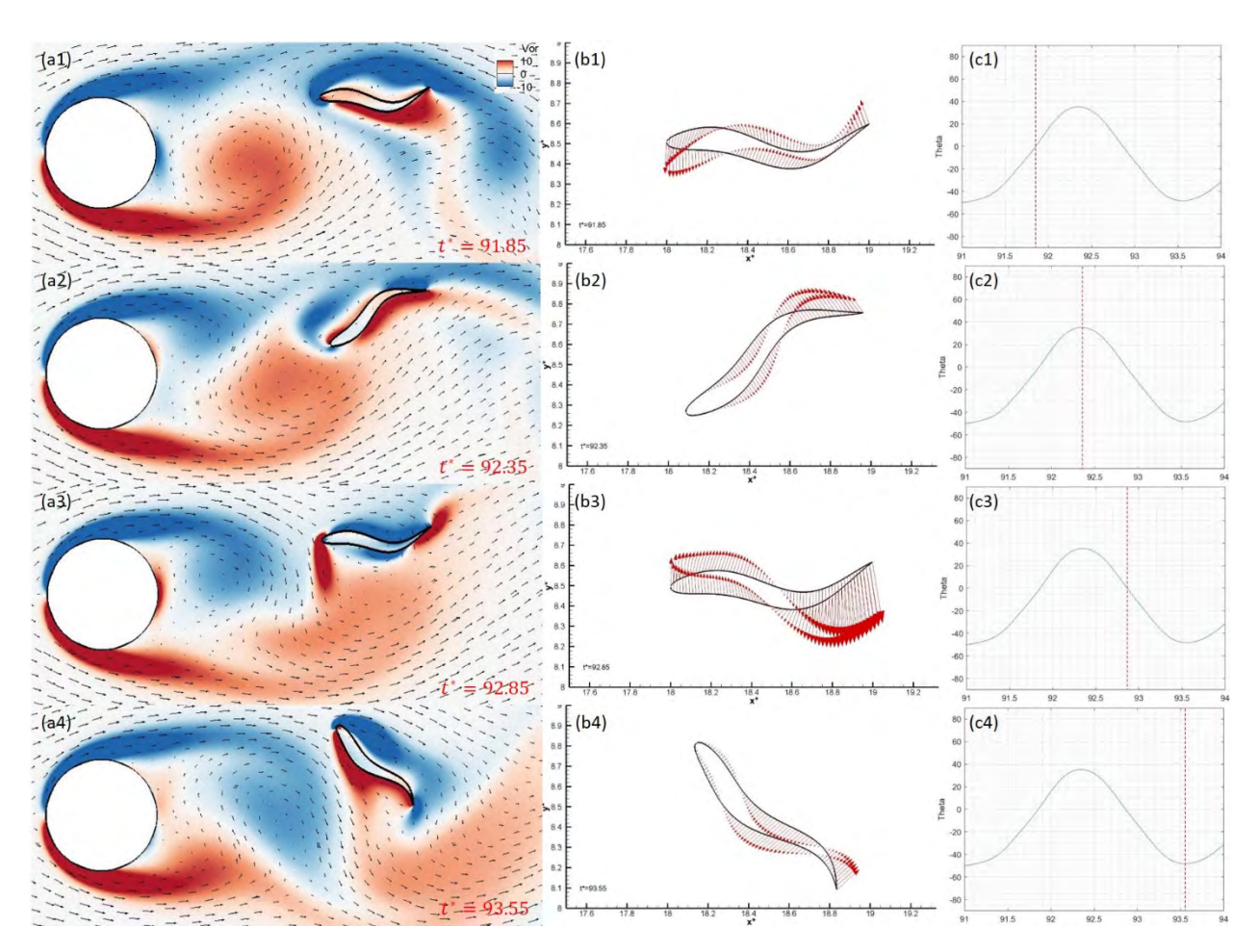


Figure 4-18 Instantaneous velocity field overlaid on vorticity contours (left), velocity diagrams along fish body boundary (centre) and angle of rotation about centroid  $\theta$  (right) at time steps  $t^* = 91.85, 92.35, 92.85 \& 93.55$  when the fish body undulates and rotates at  $d_y^* = 0.5$ . Red dash lines represent the corresponding  $\theta$  at the relevant time steps.

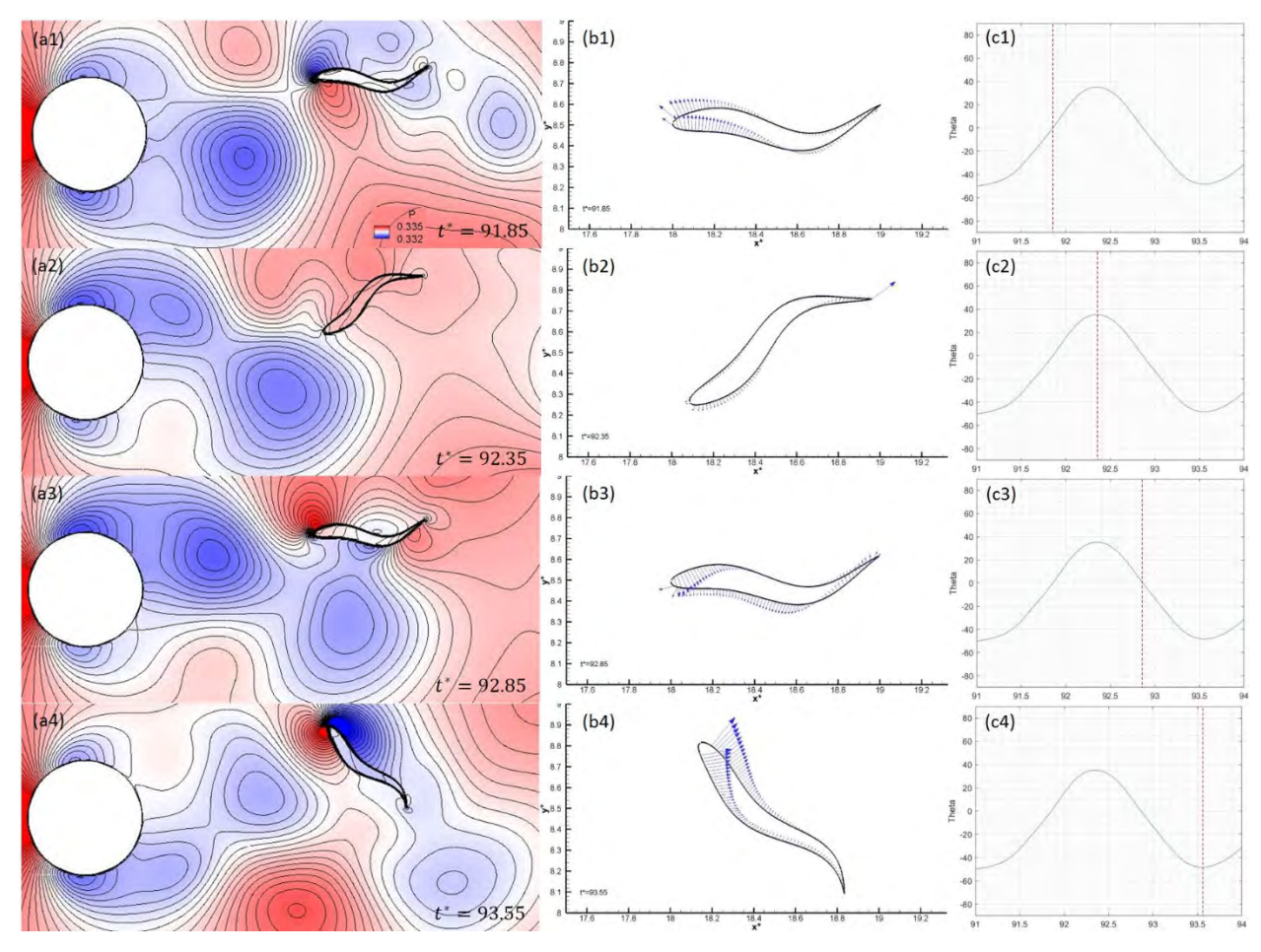


Figure 4-19 Pressure contours (left), force diagrams along fish body boundary (centre) and angle of rotation about centroid  $\theta$  (right) at time steps  $t^* = 91.85, 92.35, 92.85 \& 93.55$  when the fish body undulates and rotates at  $d_y^* = 0.5$ . Red dash lines represent the corresponding  $\theta$  at the relevant time steps.

Cases of  $d_y^* = 0.1$ , 0.2, 0.3 & 0.4 share several common features which lead to the absence of valid data for performance parameters. As the fluid flows past the cylinder, it travels around the upper and lower sides of the cylinder with two shear layers formed and shed in the later moment. As we can see from the vorticity contours when the fish body is approaching perpendicular to the free-stream flow (i.e.  $-70^{\circ}$  to  $-90^{\circ}$ ) [see Figure 4-20(a4), 4-22(a3), 4-24(a4) and 4-26(a4)], the fish head is at the shed shear layer from the upper side of the cylinder. The shed shear layer causes a significant pressure difference across the upper and lower anterior part of the fish, especially for the fish at  $d_y^* = 0.3$  & 0.4, as shown in Figure 4-25(a4) and 4-27(a4). This is because the fish head is right at the core of the shear layer with the strongest vortical flow produced by the vortex shedding from the cylinder for  $d_y^* = 0.3$  & 0.4. The force generated by the pressure difference on

the fish head forms a clockwise moment about the fish centroid [see Figure 4-25(b4) and 4-27(b4)]. Therefore, the fish further rotates in the clockwise direction as indicated by velocity vectors at the anterior part of the fish in Figure 4-24(b4) and 4-26(b4). The rotation is further enhanced by the opposite velocity at the fish tail [see Figure 4-20(b3), 4-22(b3), 4-24(b4) and 4-26(b4)] so a "couple" is formed about the centroid. Finally, the excessive rotation beyond  $-90^{\circ}$  results in the overturning of the fish body as shown in Figure 4-20(a5), 4-22(a4), 4-24(a5) and 4-26(a5). The overturning of the fish prevents the acquisition of valid performance data from the computation.

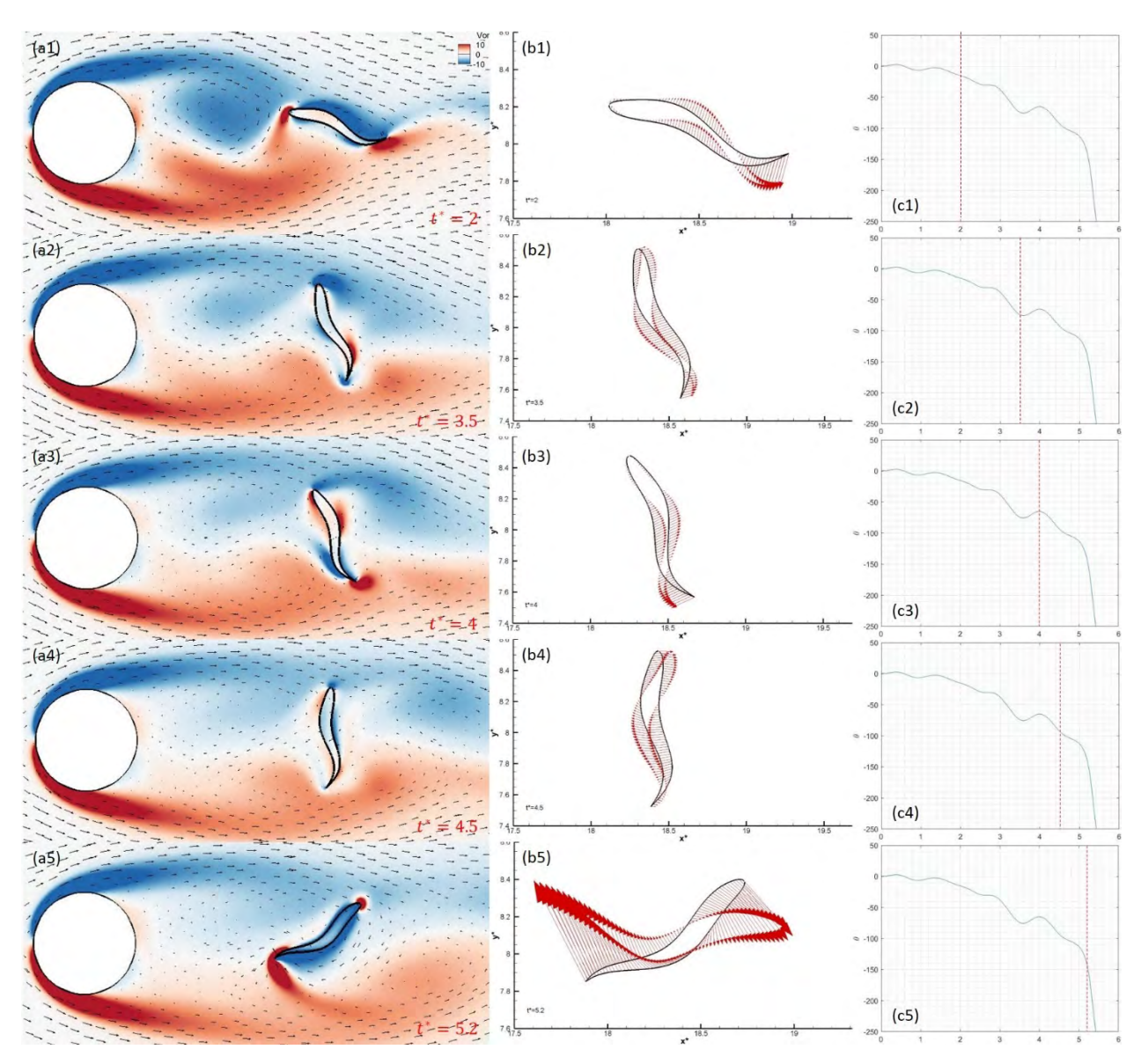


Figure 4-20 Instantaneous velocity field overlaid on vorticity contours (left), velocity diagrams along fish body boundary (centre) and angle of rotation about centroid  $\theta$  (right) at time steps  $t^* = 2, 3.5, 4, 4.5 \& 5.2$ 

when the fish body undulates and rotates at  $d_y^* = 0.1$ . Red dash lines represent the corresponding  $\theta$  at the relevant time steps.

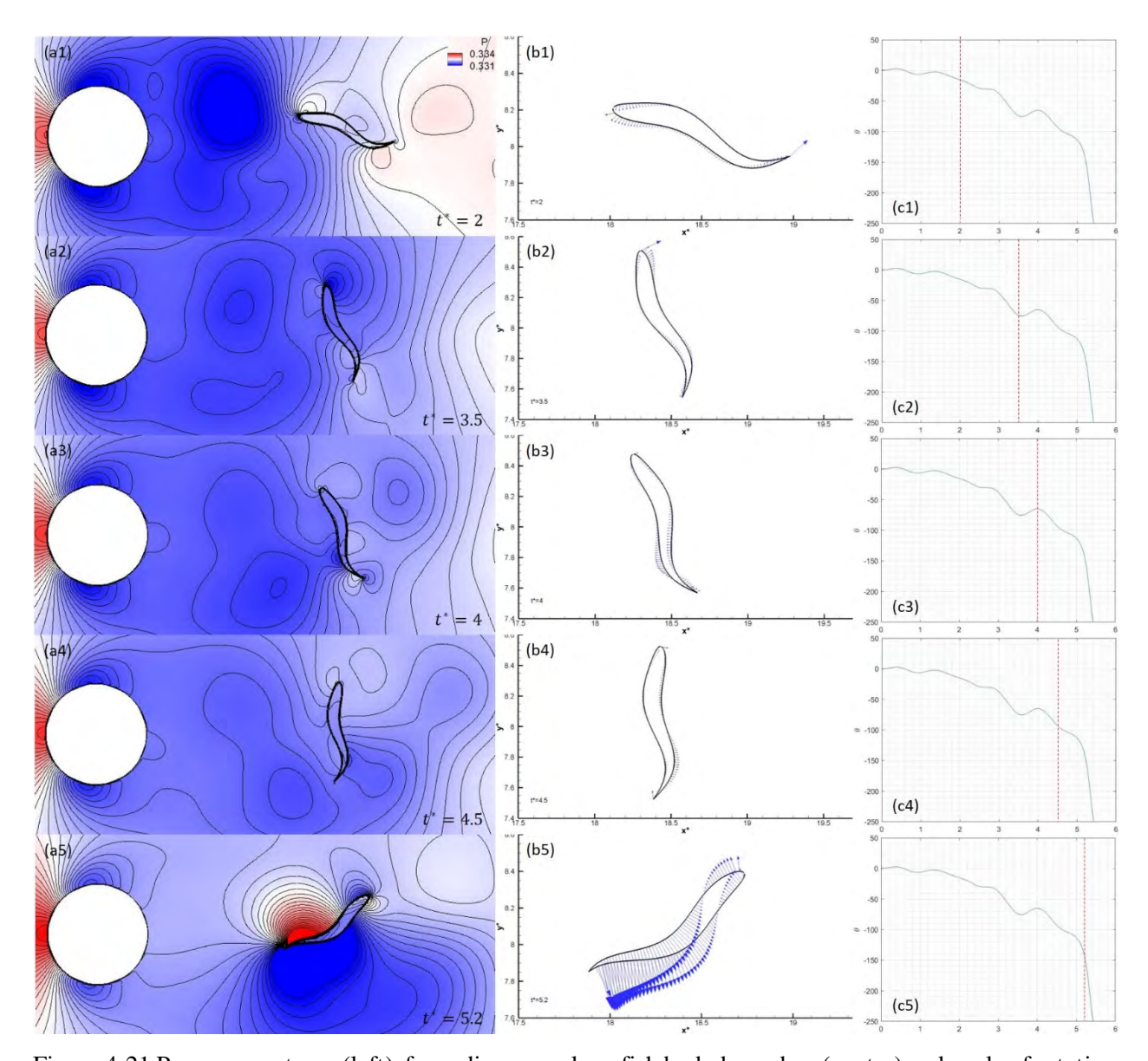


Figure 4-21 Pressure contours (left), force diagrams along fish body boundary (centre) and angle of rotation about centroid  $\theta$  (right) at time steps  $t^* = 2, 3.5, 4, 4.5 \& 5.2$  when the fish body undulates and rotates at  $d_y^* = 0.1$ . Red dash lines represent the corresponding  $\theta$  at the relevant time steps.

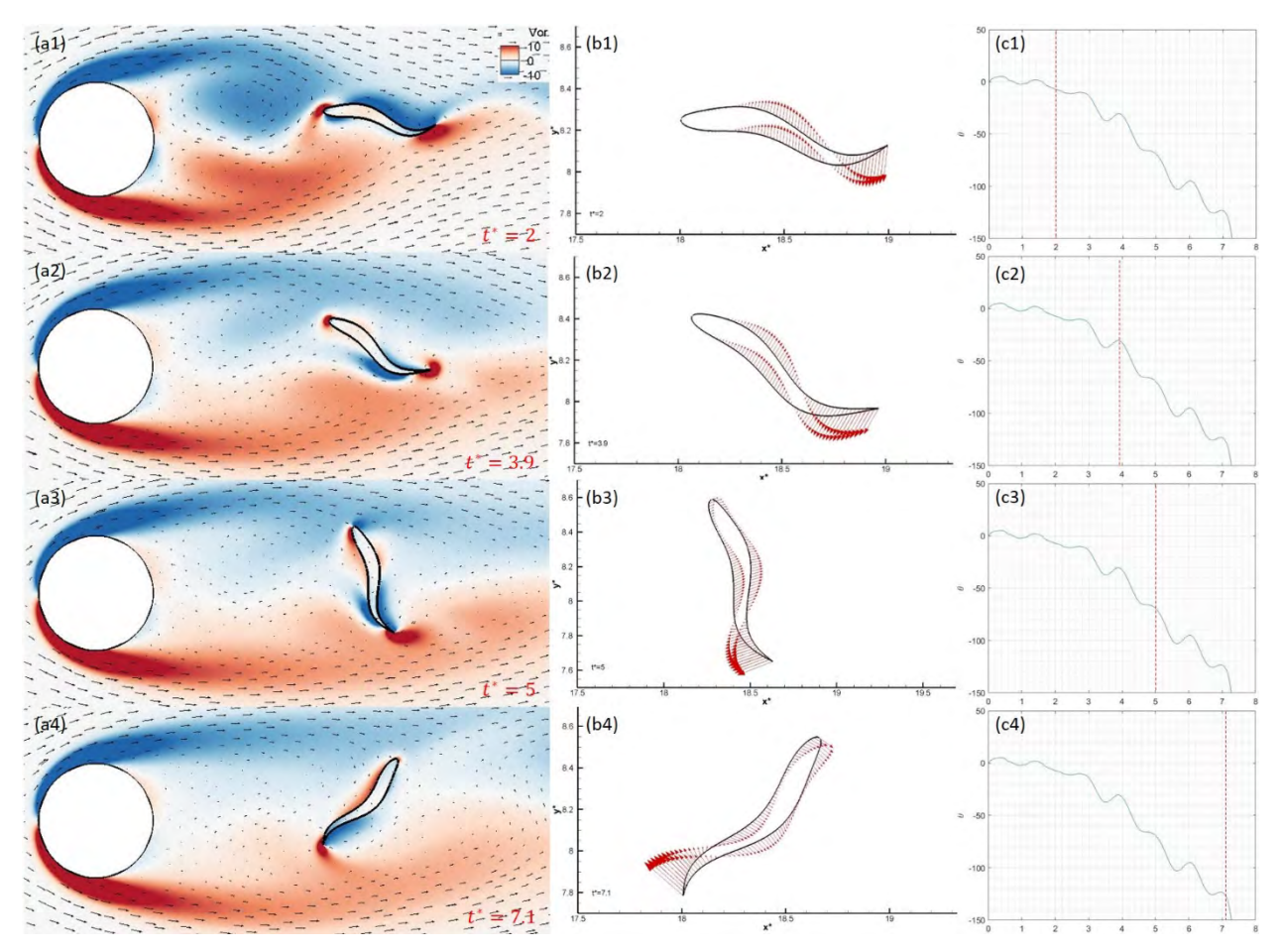


Figure 4-22 Instantaneous velocity field overlaid on vorticity contours (left), velocity diagrams along fish body boundary (centre) and angle of rotation about centroid  $\theta$  (right) at time steps  $t^* = 2, 3.9, 5 \& 7.1$  when the fish body undulates and rotates at  $d_y^* = 0.2$ . Red dash lines represent the corresponding  $\theta$  at the relevant time steps.

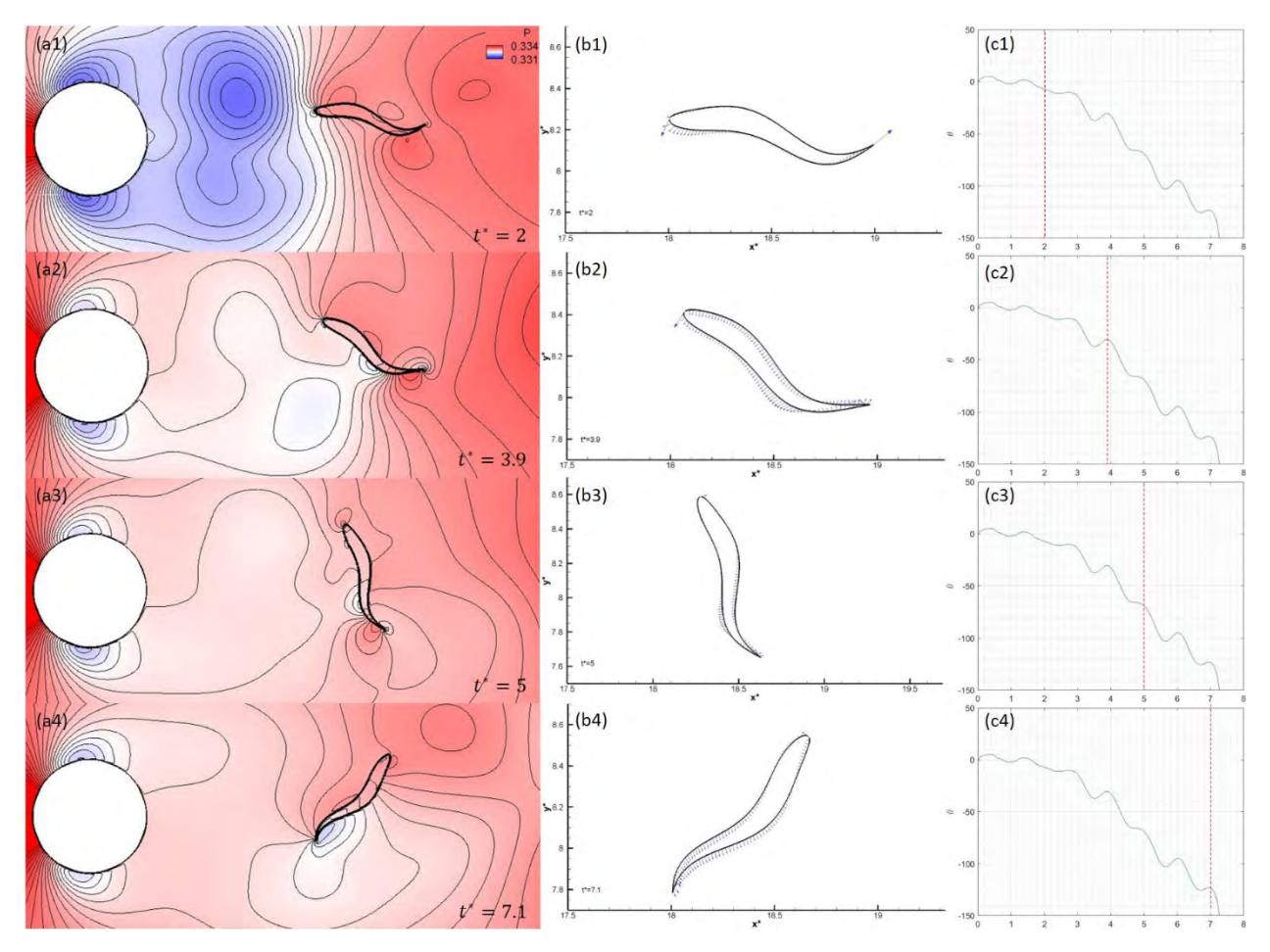


Figure 4-23 Pressure contours (left), force diagrams along fish body boundary (centre) and angle of rotation about centroid  $\theta$  (right) at time steps  $t^* = 2,3.9,5 \& 7.1$  when the fish body undulates and rotates at  $d_y^* = 0.2$ . Red dash lines represent the corresponding  $\theta$  at the relevant time steps.

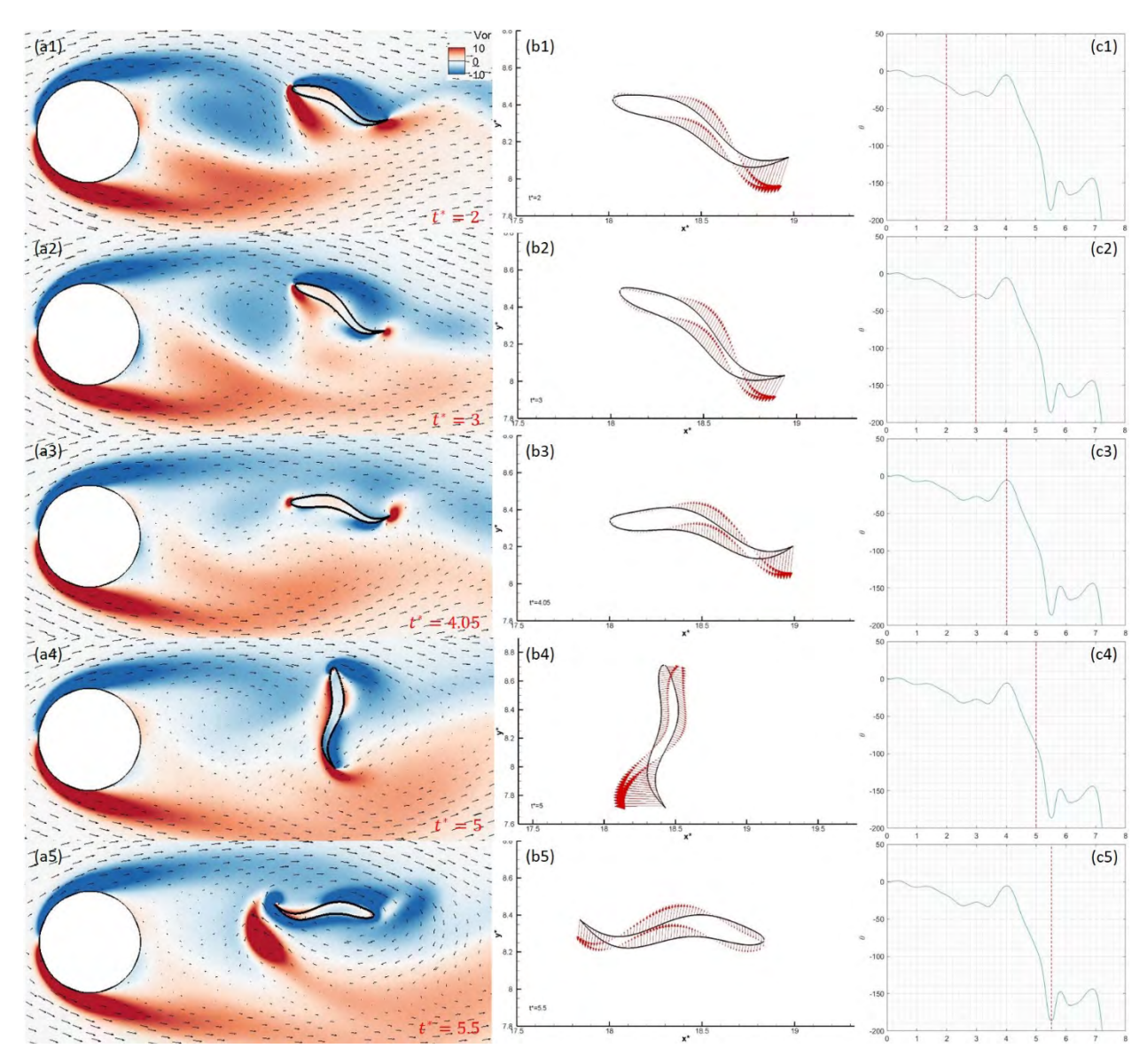


Figure 4-24 Instantaneous velocity field overlaid on vorticity contours (left), velocity diagrams along fish body boundary (centre) and angle of rotation about centroid  $\theta$  (right) at time steps  $t^* = 2, 3, 4.05, 5 \& 5.5$  when the fish body undulates and rotates at  $d_y^* = 0.3$ . Red dash lines represent the corresponding  $\theta$  at the relevant time steps.

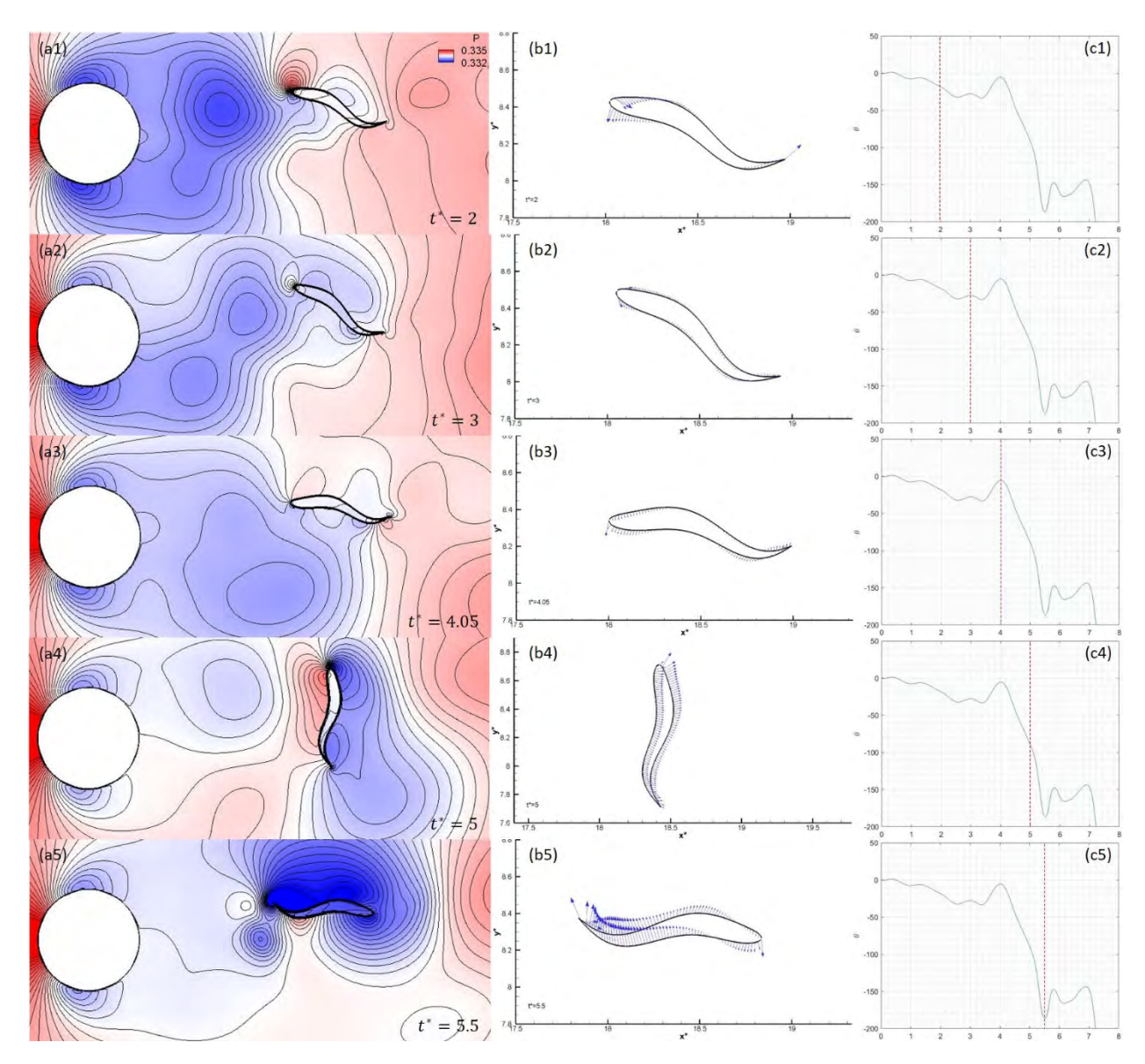


Figure 4-25 Pressure contours (left), force diagrams along fish body boundary (centre) and angle of rotation about centroid  $\theta$  (right) at time steps  $t^* = 2,3,4.05,5 \& 5.5$  when the fish body undulates and rotates at  $d_y^* = 0.3$ . Red dash lines represent the corresponding  $\theta$  at the relevant time steps.

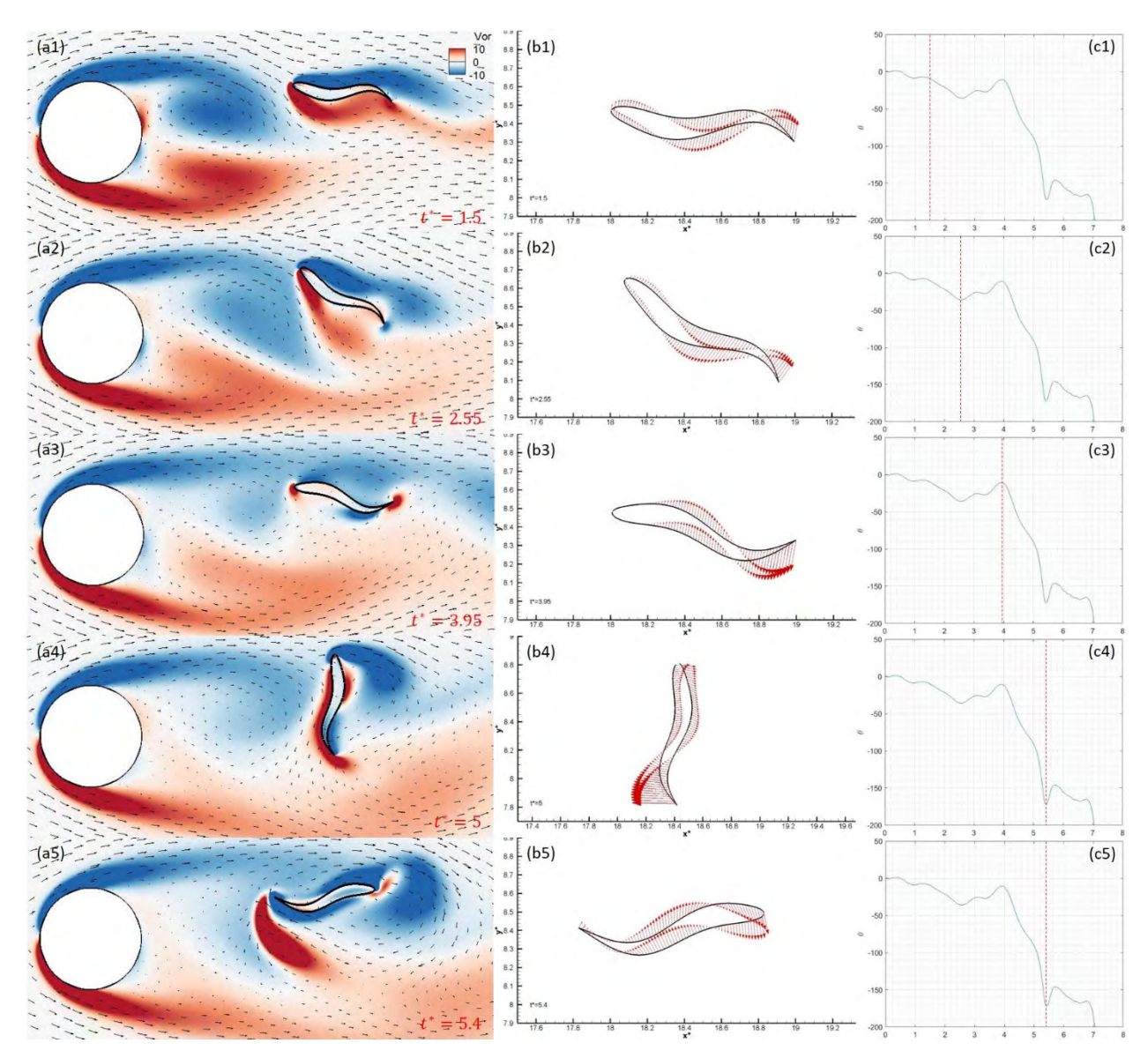


Figure 4-26 Instantaneous velocity field overlaid on vorticity contours (left), velocity diagrams along fish body boundary (centre) and angle of rotation about centroid  $\theta$  (right) at time steps  $t^* = 1.5, 2.55, 3.95, 5 \& 5.4$  when the fish body undulates and rotates at  $d_y^* = 0.4$ . Red dash lines represent the corresponding  $\theta$  at the relevant time steps.

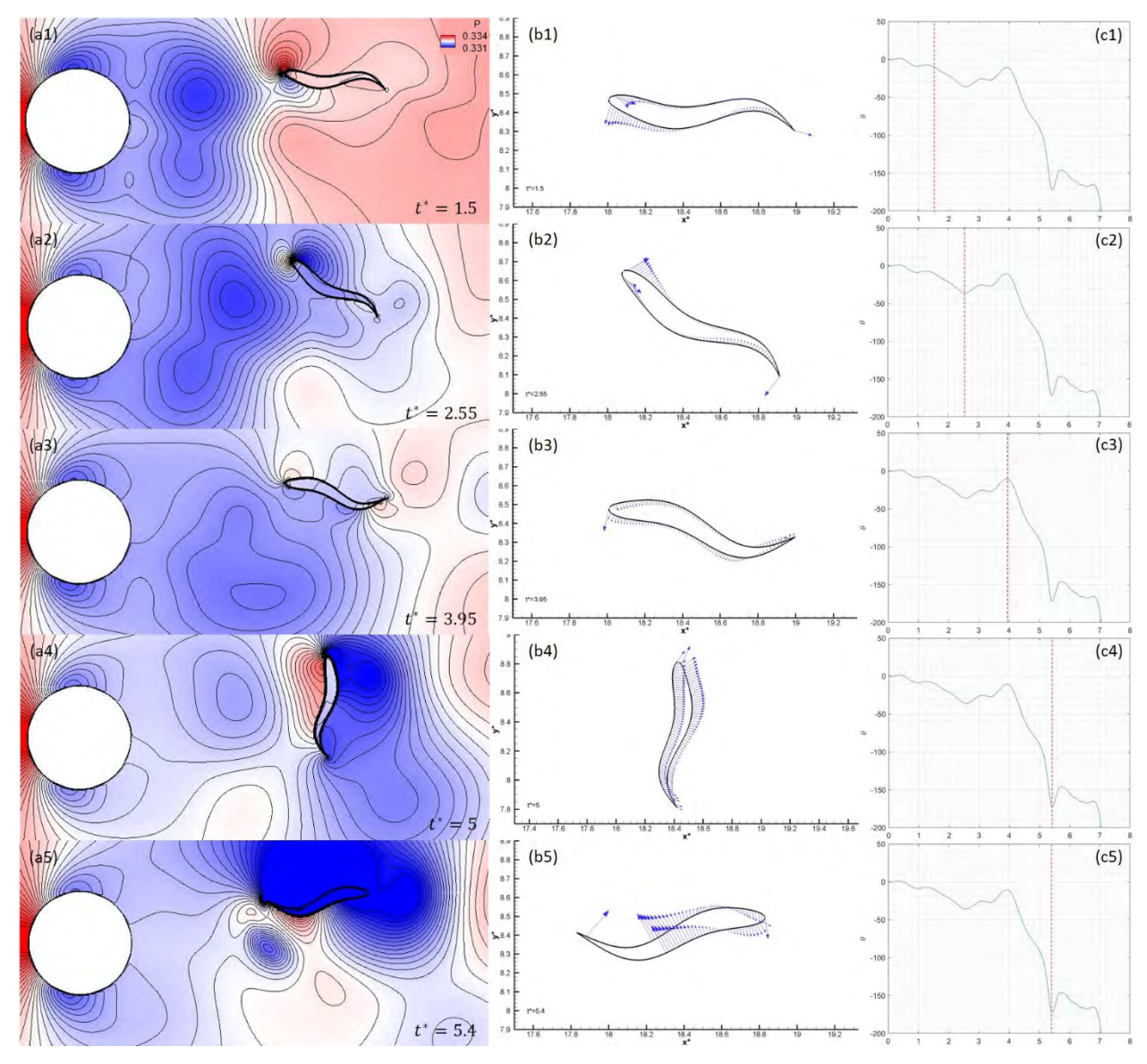


Figure 4-27 Pressure contours (left), force diagrams along fish body boundary (centre) and angle of rotation about centroid  $\theta$  (right) at time steps  $t^* = 1.5, 2.55, 3.95, 5 \& 5.4$  when the fish body undulates and rotates at  $d_y^* = 0.4$ . Red dash lines represent the corresponding  $\theta$  at the relevant time steps.

## 4.3. Remarks

For fish undulation with rotation, two controlling parameters are studied with the results summarised as follows:

- Thrust is generated when the fish is positioned close to the cylinder in the streamwise direction
   (i.e. d<sub>x</sub>\* ≤ 2.8). When the fish is positioned further downstream from the cylinder, drag is
   experienced by the fish. Rotation angle is the contributing factor to drag experienced by the
   fish. Moreover, obvious vortex shedding is observed behind the cylinder when the fish
   experiences drag.
- 2. Overturning of the fish body is observed because of excessive rotation about the fish centroid when the fish head is at the shed shear layer. Otherwise, when the fish centroid is either aligned with the centre of the cylinder or the shed shear layer, a stable rotation is observed.

# Chapter 5 Self-Propelled Swimming behind Single Cylinder

After the study on undulation and rotation of the swimmer, the fundamental understanding of the interaction between the swimmer and the cylinder is acquired. In this chapter, the degree of freedom of the swimmer is further released to enable the investigation on another mode of motion, translation, and ultimately free swimming. Section 5.1 covers the study on the swimmer translating in the streamwise direction together with rotation and undulation. In Section 5.2, free swimming is actualized in which the swimmer could undulate, rotate and translate in both streamwise and crossflow directions simultaneously.

# 5.1. Swimming in Streamwise Direction

With reference to Figure 2-3(a), the fish model is initially positioned with the "nose" at the chosen position (i.e.  $d_x^* \& d_y^*$ ). The fish body undulates as prescribed by equation (2.1) and is allowed to rotate and translate in streamwise direction. Based on the experience gained from previous studies in chapter 4,  $Re_{fish}$ ,  $U_\infty^*$  and  $D^*$  are maintained as 40, 2.5 and 1 respectively. The ranges of initial streamwise and crossflow distances are chosen considering the results in chapter 4. For ease of discussion, all relevant parameters with adopted values are listed in Table 5.1.

Table 5.1 Definitions and chosen values of relevant parameters in Chapter 5.1

Parameter	Definition	Values <sup>a,b</sup>
Cylinder diameter	$D^* = D/L$	1
Streamwise distance	$d_x^* = d_x/L$	2.8, 2.9, 3, 3.1, 3.2, 3.3, <b>3.4</b> , <b>3.5</b> , 3.6,
		3.7, 3.8, 3.9, 4
Crossflow distance	$d_y^* = d_y/L$	<b>0</b> , 0.1, 0.2, 0.5
Reynolds number	$Re_{fish} = V_{max}L/\nu$	40
(fish undulatory velocity)		
Reynolds number	$Re_{\infty} = U_{\infty}L/\nu$	127.3
(free-stream flow)		
Strouhal number	$St = f_{vor}D/U_{\infty}$	-
Time	$t^* = t/T_P = tU_{ref}/L$	-
Free-stream velocity	$U_{\infty}^* = U_{\infty}/U_{ref}$	2.5
Angle of rotation	$\theta$	-

<sup>&</sup>lt;sup>a</sup> The symbol '-' indicates that the parameters change according to different cases or are updated during the simulation.

#### **5.1.1.** Effect of Initial Streamwise Distance

To explore the effect of initial streamwise distance  $(d_x^*)$ , crossflow distance  $(d_y^*)$  is set to the baseline value, i.e.  $d_y^* = 0$ , based on the results in chapter 4. Initial streamwise distances,  $d_x^* = 2.8$  to 4, are examined in the study. Figure 5-1 shows the streamwise trajectories and angle of rotation about the fish centroid for cases with different  $d_x^*$ . We can see that the fish swim towards the cylinder for  $d_x^* \leq 3.4$  as indicated by the decrease in  $d_x^*$  with  $t^*$ . In contrast, the fish is drifted away from the cylinder when  $d_x^* \geq 3.7$ . This phenomenon is also observed when the fish is initially positioned at  $d_x^* = 4$  without the presence of the cylinder upstream. For  $d_x^* = 3.5 \otimes 3.6$ , the result is not as the expected trend. The fish is drifted downstream from the cylinder when  $d_x^* = 3.5$  while it swims towards the cylinder when  $d_x^* = 3.6$ . On the other hand, it is found that the fish rotates within the range of  $\pm 40^\circ$  for  $d_x^* \leq 3.4$  and  $d_x^* = 3.6$  while the angle of rotation  $(\theta)$  exceeds  $\pm 90^\circ$  sharply for  $d_x^* = 3.5$  and  $d_x^* \geq 3.7$ .

<sup>&</sup>lt;sup>b</sup> The bold values are used as baseline parameters.

Vorticity contours are displayed to reveal the reason behind the discrepancy between  $d_x^* = 3.4$  and 3.7. Figure 5-2 and 5-3 clearly show that the vortex shedding from the cylinder is more significant for  $d_x^* = 3.5 \& 3.7$ . The strong vortical flow approaches the anterior part of the fish at initial  $d_x^* = 3.5 \& 3.7$  with a high velocity as shown by intense velocity vectors pointing towards the fish body [see Figure 5-2(b1-b3) and 5-3(b1-b2)]. The flow causes a vigorous rotation about the fish centroid. As the fish rotation approaches  $-90^\circ$ , the fish is nearly perpendicular to the vortical flow as shown in Figure 5-2(b5) and 5-3(b3). The strong flow exerts a force on the anterior part of the fish, especially the nose. This creates a large drag on the fish in which the strong vortical flow pushes the fish further downstream. The flow at the fish nose also constitutes a clockwise torque about the centroid at the same time. This torque overturns the fish body which explains the exceedance of angle of rotation beyond  $-90^\circ$  dramatically in Figure 5-1(b).

On the other hand, for  $d_x^* = 3.4 \& 3.6$ , the vortex shedding from the cylinder is weaker than  $d_x^* = 3.5 \& 3.7$ . The vortical flow approaches the anterior part of the fish with a lower velocity as we can only observe small velocity vectors around the fish body in Figure 5-2(a1-a6) and 5-3(a1-a6). The flow does not cause the fish to rotate vigorously as in the cases with initial  $d_x^* = 3.5 \& 3.7$ . This corresponds to the range of rotation between  $-40^\circ$  and  $40^\circ$  in Figure 5-1(b). This condition favours the fish swimming that it creates a suction zone for the fish. Therefore, the fish keeps swimming towards the cylinder.

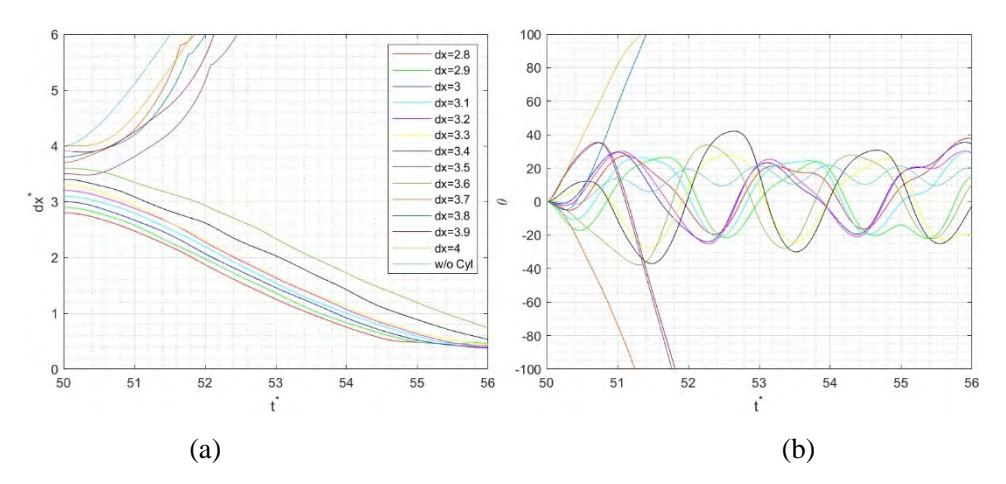


Figure 5-1 (a) Streamwise trajectories and (b) angles of rotation about centroid  $\theta$  of the fish in cases with different initial streamwise positions  $d_x^* = 2.8$  to 4. The case without the presence of the cylinder is also included as a reference.

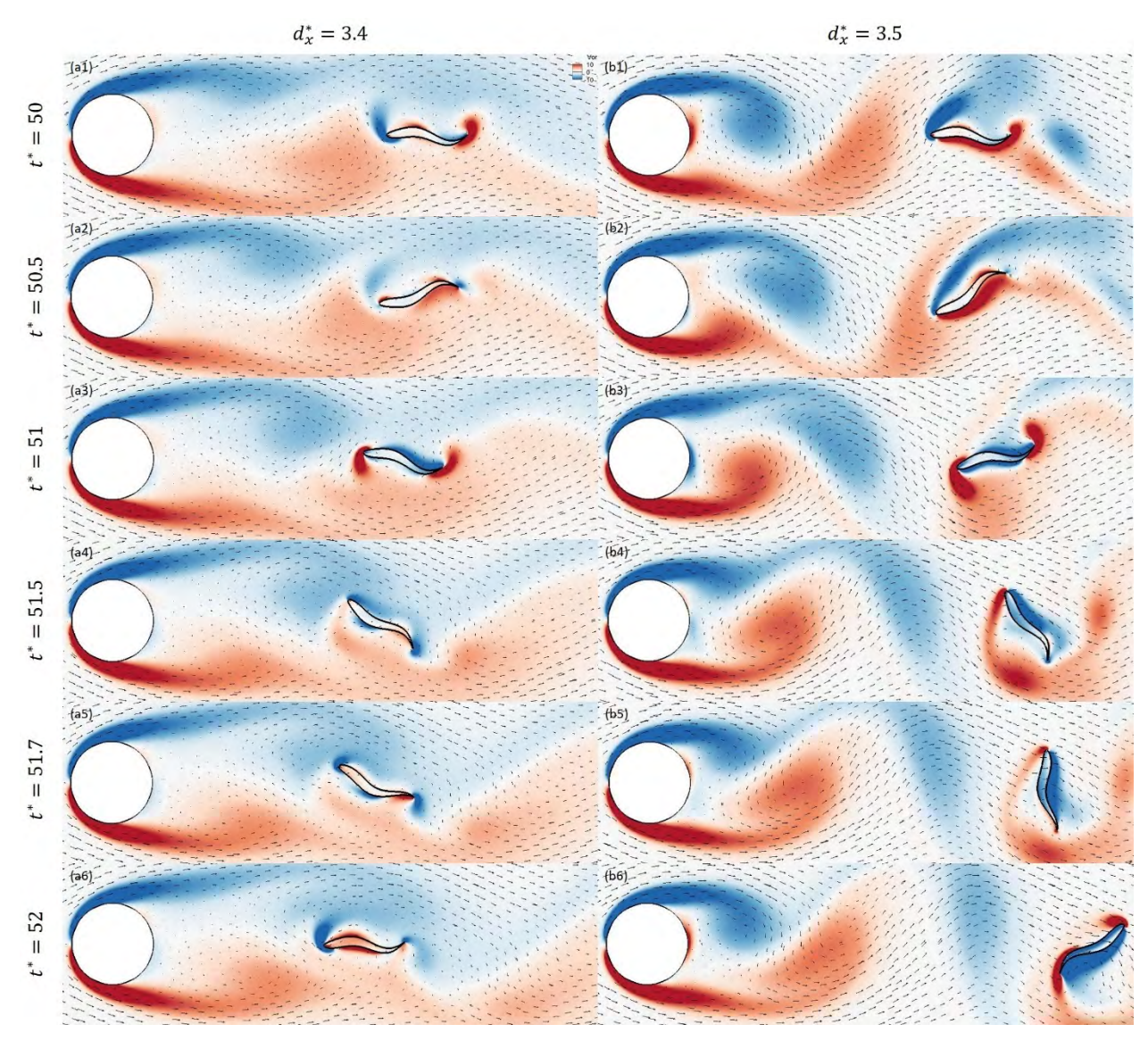


Figure 5-2 Comparison of instantaneous velocity field overlaid on vorticity contours when the fish body undulates, rotates and translates in streamwise direction from the initial position of  $d_x^* = 3.4$  (left) and 3.5 (right) for time step of  $t^* = 50, 50.5, 51, 51.5, 51.7 \& 52$ .

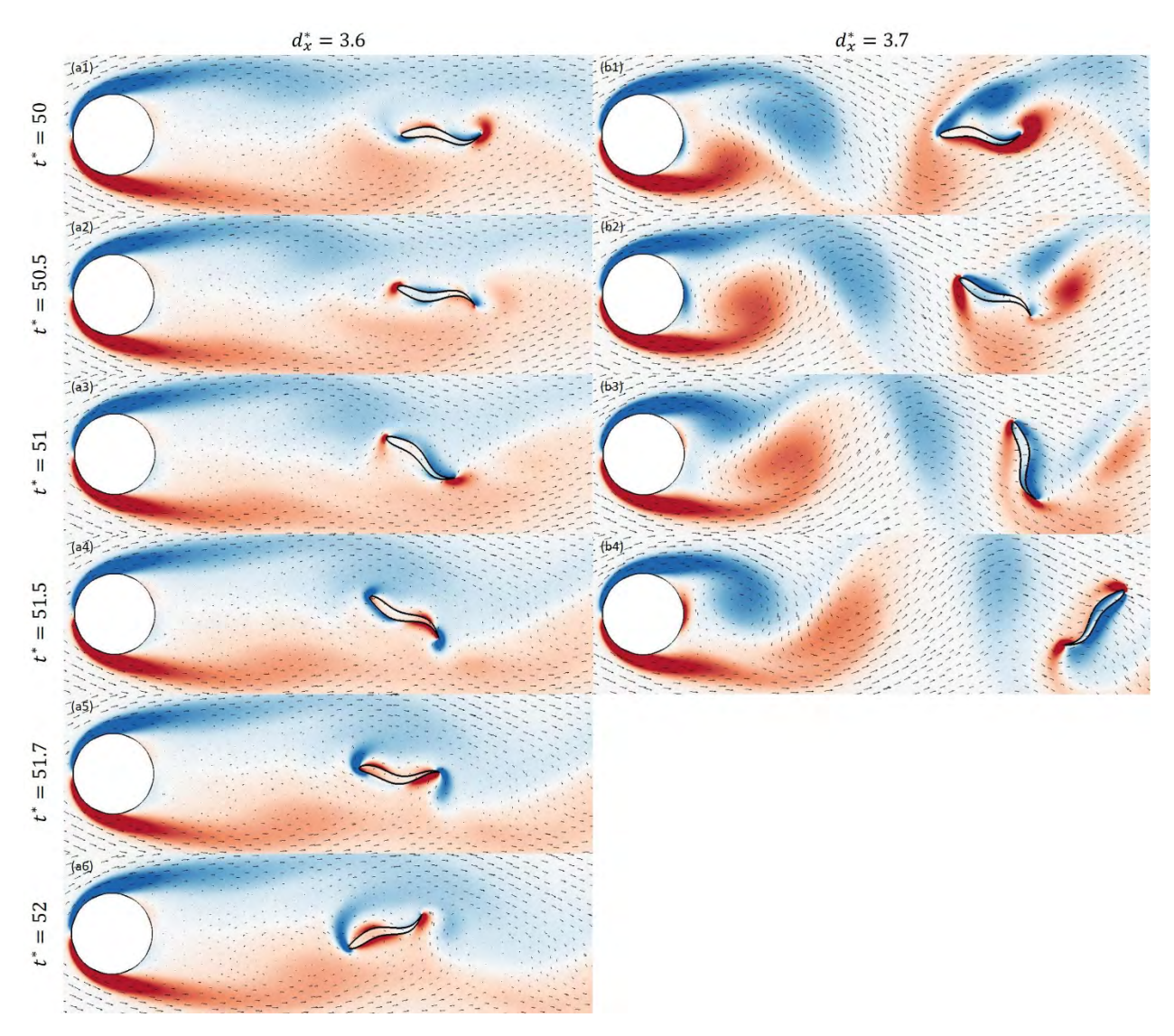


Figure 5-3 Comparison of instantaneous velocity field overlaid on vorticity contours when the fish body undulates, rotates and translates in streamwise direction from the initial position of  $d_x^* = 3.6$  (left) for time step of  $t^* = 50, 50.5, 51, 51.5, 51.7$  & 52 and  $d_x^* = 3.7$  (right) for time step of  $t^* = 50, 50.5, 51$  & 51.5.

#### **5.1.2.** Effect of Initial Crossflow Distance

After the investigation on the effect of initial streamwise distance  $(d_x^*)$ , our next focus is the effect of initial crossflow distance  $(d_y^*)$ . Based on the discrepancy observed in the study of initial  $d_x^*$ , the baseline values of  $d_x^* = 3.4 \& 3.5$  are set. Initial crossflow distances,  $d_y^* = 0, 0.1, 0.2$  and 0.5, are examined. Figure 5-4 shows the streamwise trajectories and angle of rotation about the fish centroid for cases with different  $d_y^*$  among  $d_x^* = 3.4 \& 3.5$ . It is observed that the fish only swims towards the cylinder in the cases of  $d_x^* = 3.4, d_y^* = 0$  and  $d_x^* = 3.4, d_y^* = 0.1$ . In these cases, the

fish rotates within the range of  $\pm 50^{\circ}$  with a decreasing trend of angle of rotation. The fish drifts away from the cylinder in other cases of  $d_y^*$  with initial  $d_x^* = 3.4$  and all cases with initial  $d_x^* = 3.5$ .

Vorticity contours are employed to reveal the reason behind the discrepancy between  $d_y^* = 0$ , 0.1 and 0.2 with initial  $d_x^* = 3.4$ . Figure 5-5 shows that the vortex shedding from the cylinder is more significant for initial  $d_y^* = 0.2$ . The strong vortical flow mostly acts on the anterior part of the fish. When the fish body is approaching perpendicular to the free-stream flow (i.e.  $-70^\circ$  to  $-90^\circ$ ) [see Figure 5-5(c4)], the fish head is at the shed shear layer from the upper side of the cylinder. The strong flow acts on the lower anterior part of the fish, as shown by the intense velocity vectors. This causes the fish to rotate about its centroid in the clockwise direction and exerts large drag on the fish body. As a result, the fish is overturned and pushed downstream by the shed shear layer and vortical flow as shown in Figure 5-5(c5).

In contrast, the vortex shedding from the cylinder is weaker for the case with initial  $d_y^* = 0$  and 0.1. The vortical flow acts on the whole body of the fish evenly. As the centroid maintains aligned with the centre of the cylinder laterally, the periodic vortex shedding from the cylinder acts on the anterior and posterior parts of the fish alternatively [see Figure 5-5(a1-a5) and (b1-b5)]. The fish returns to its equilibrium position (i.e.  $\theta = 0^{\circ}$ ) periodically. Hence, the range of rotation is maintained within  $\pm 50^{\circ}$  in which overturning of the fish body would not happen.

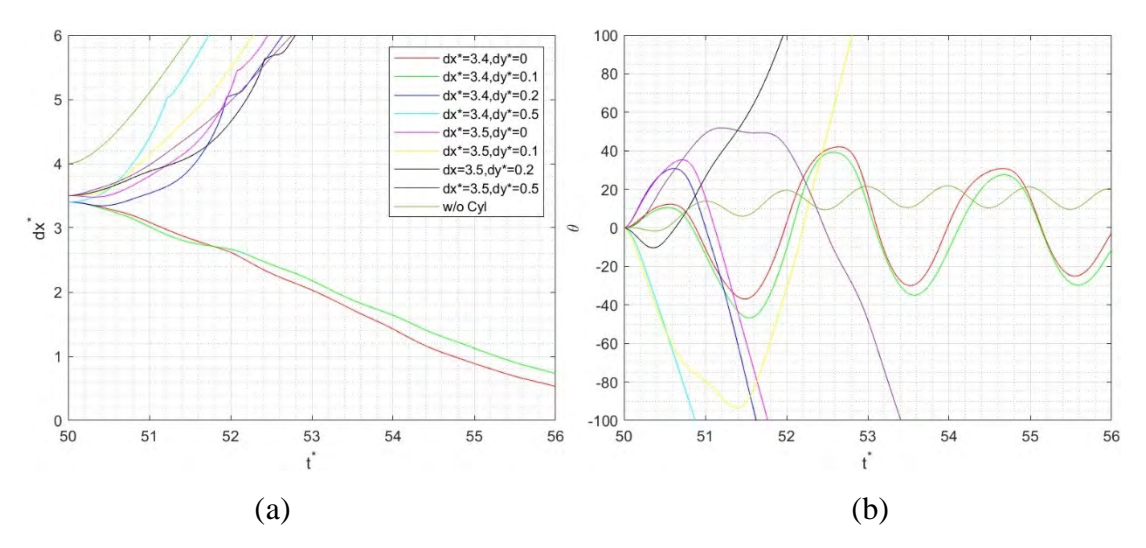


Figure 5-4 (a) Streamwise trajectories and (b) angles of rotation about centroid  $\theta$  of the fish in cases with different initial streamwise positions among  $d_x^* = 3.4 \& 3.5$  and varying crossflow positions between  $d_y^* = 0$ , 0.1, 0.2 and 0.5. The case without the presence of the cylinder is also included as a reference.

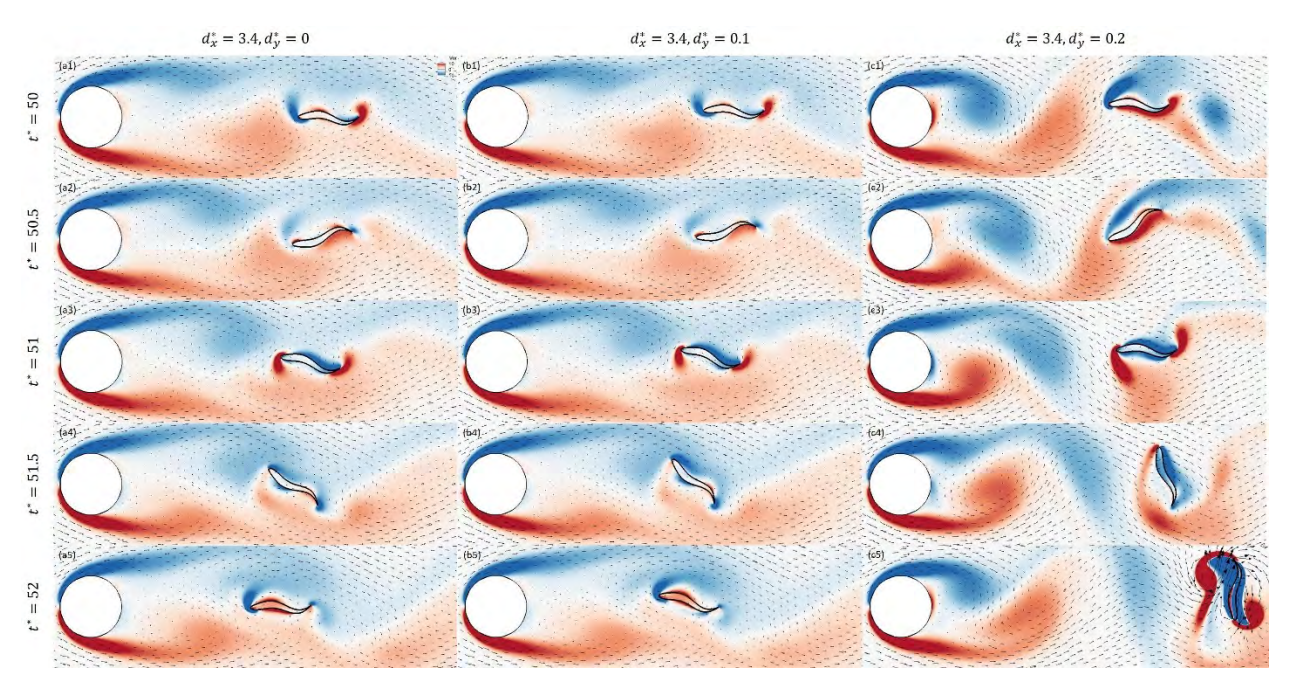


Figure 5-5 Comparison of instantaneous velocity field overlaid on vorticity contours when the fish body undulates, rotates and translates in streamwise direction from the initial position of  $d_x^* = 3.4$ ,  $d_y^* = 0$  (left),  $d_x^* = 3.4$ ,  $d_y^* = 0.1$  (centre) and  $d_x^* = 3.4$ ,  $d_y^* = 0.2$  (right) for time step of  $t^* = 50$ , 50.5, 51, 51.5 & 52.

# **5.2.** Free Swimming

With the knowledge gained from previous studies about different modes of motion, the degree of freedom of the fish is finally released to allow free swimming. As described in Figure 2-3(a), the "nose" of the fish model is positioned at a chosen position (i.e.  $d_x^* \& d_y^*$ ) initially. The fish model undulates as prescribed by equation (2.1) with rotation allowed about its centroid. It is also allowed to swim longitudinally and laterally in streamwise and crossflow directions respectively.  $Re_{fish}$ ,  $U_\infty^*$  and  $D^*$  are maintained as 40, 2.5 and 1 respectively based on studies in previous chapters. The range of initial streamwise distance is chosen by considering the results in chapter 5.1. For ease of discussion, all relevant parameters with adopted values are listed in Table 5.2.

Table 5.2 Definitions and chosen values of relevant parameters in Chapter 5.2

Parameter	Definition	Values <sup>a</sup>
Cylinder diameter	$D^* = D/L$	1
Streamwise distance	$d_x^* = d_x/L$	3, 3.3, 3.4, 3.45, 3.5, 3.6, 3.65, 3.7, 3.8, 3.9, 4
Crossflow distance	$d_y^* = d_y/L$	0
Reynolds number	$Re_{fish} = V_{max}L/\nu$	40
(fish undulatory velocity)		
Reynolds number	$Re_{\infty} = U_{\infty}L/\nu$	127.3
(free-stream flow)		
Strouhal number	$St = f_{vor}D/U_{\infty}$	-
Time	$t^* = t/T_P = tU_{ref}/L$	-
Free-stream velocity	$U_{\infty}^{*}=U_{\infty}/U_{ref}$	2.5
Angle of rotation	heta	-

<sup>&</sup>lt;sup>a</sup> The symbol '-' indicates that the parameters change according to different cases or are updated during the simulation.

As revealed in previous studies on the effect of crossflow distance,  $d_y^* = 0$  would be the most ideal initial lateral position to place the fish model. Therefore, in this section, our focus would be the effect of initial streamwise distance  $(d_x^*)$  with crossflow distance set to  $d_y^* = 0$ . Figure 5-6 shows the streamwise trajectory, crossflow trajectory and angle of rotation about the fish centroid for cases with different initial  $d_x^*$ . We can observe the discrepancy between  $d_x^* = 3.4$  and 3.7. For

cases of  $d_x^* \le 3.4$ , the fish swims towards the cylinder and the lateral displacement is maintained within a range of  $-0.3 < d_y^* < 0.3$ . For the case of  $d_x^* = 3.5$ , the fish swims towards the cylinder initially and then drifts away. The magnitude of lateral movement (i.e.  $|d_y^*|$ ) increases with time. For the case of  $d_x^* = 3.6$ , the result is the same as  $d_x^* = 3.4$  with swimming towards the cylinder and lateral movement within the range of  $|d_y^*| < 0.3$ . In contrast, for cases of  $d_x^* \ge 3.7$ , the fish is drifted away from the cylinder immediately at the beginning of the simulation. Its lateral displacement shows an increasing trend with time.

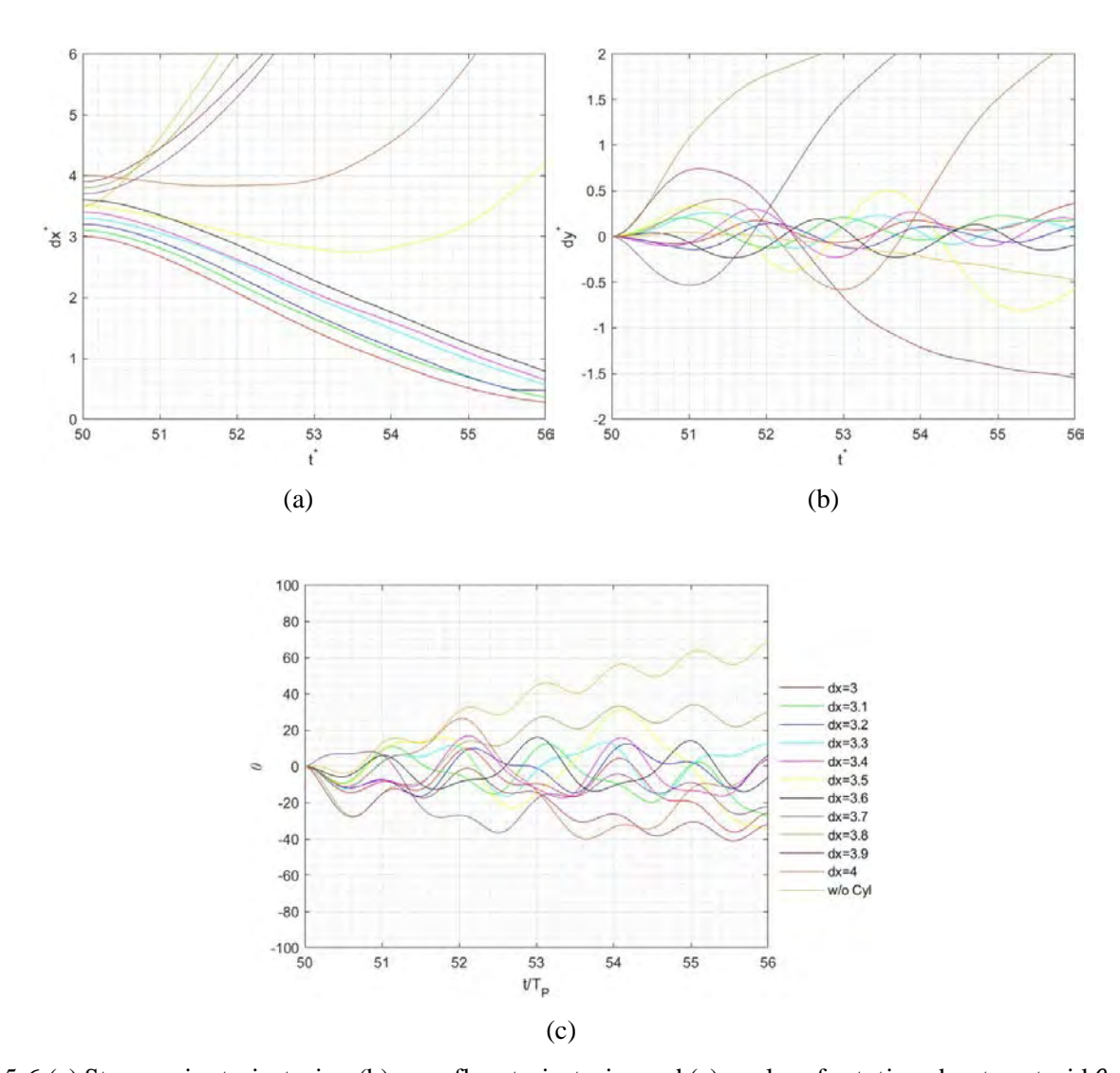


Figure 5-6 (a) Streamwise trajectories, (b) crossflow trajectories and (c) angles of rotation about centroid  $\theta$  of the fish in cases with different initial streamwise positions  $d_x^* = 3, 3.1, 3.2, 3.3, 3.4, 3.5, 3.6, 3.7, 3.8, 3.9 & 4$ . The case without the presence of the cylinder is also included as a reference.

To have a better understanding of the discrepancy between  $d_x^* = 3.4$  and 3.7, the flow structure around the cylinder and the fish is analysed. Figure 5-7 and 5-8 show the vorticity contours with instantaneous velocity field overlaid for initial position at  $d_x^* = 3.4, 3.5, 3.6 \& 3.7$ . It is obvious that vortex shedding from the cylinder is the strongest for the case of  $d_x^* = 3.7$  [see Figure 5-8(b1)]. The strong vortical flow acts on the anterior part of the fish and causes it displaced laterally to the shed shear layer rapidly. The shear layer combined with the vortical flow further push the fish away from the cylinder in a short period of time [see Figure 5-8(b2-b3)]. In contrast, vortex shedding from the cylinder is not as significant as other cases for  $d_x^* = 3.4 \& 3.6$ . The fish maintains its trajectory along the extended line from the centre of the cylinder nearly the whole time (i.e.  $|d_y^*| < 0.3$ ) [see Figure 5-7(a1-a7) and 5-8(a1-a7)]. The fish keeps staying in the suction zone and is not affected by the strong shear layer shed from either side of the cylinder. Therefore, the reverse flow downstream of the fish pushes the fish towards the cylinder.

The case for  $d_x^* = 3.5$  is different from other cases in which the flow structure changes from weak to strong vortical flow [see Figure 5-7(b1) and (b6)]. It is observed that the fish is slightly affected by the weak vortical flow at the beginning as shown by its lateral displacement from the initial position (i.e.  $d_y^* = 0$ ) During this time interval, the fish keeps swimming towards the cylinder as depicted in Figure 5-7(b2-b5). However, at  $t^* = 54$ , the fish swims up to the position in which the vorticity becomes stronger [see Figure 5-7(b5)]. The fish rotates in the anticlockwise direction because of strong vortical flow. The fish is now inclined in an angle such that the strong flow exerts the force normal to the upper body. This force pushes the fish downstream and laterally to the lower shear layer shed from the cylinder at the same time. Once the fish is along the shear layer, the strong flow acts on the fish body aggressively by pushing it downstream and causing significant rotation [see Figure 5-7(b6) and (b7)].

Though the investigation on flow structure around the cylinder ad the fish at different initial  $d_x^*$ , it is found that the initial position of the fish affects the intensity of vortex shedding from the cylinder. When the fish is positioned at  $d_x^* \geq 3.7$ , the vortex shedding is unlikely influenced by the fish, thus a strong intensity of vorticity is recorded. On the contrary, when the fish is positioned at  $d_x^* \leq 3.6$  and  $-0.3 < d_y^* < 0.3$ , it seems that vortex shedding is suppressed by the presence of the fish. As long as the fish maintains its streamwise and crossflow distances within the aforementioned

ranges, it is inside the suction zone and beneficial from thrust generated by the action of reverse flow.

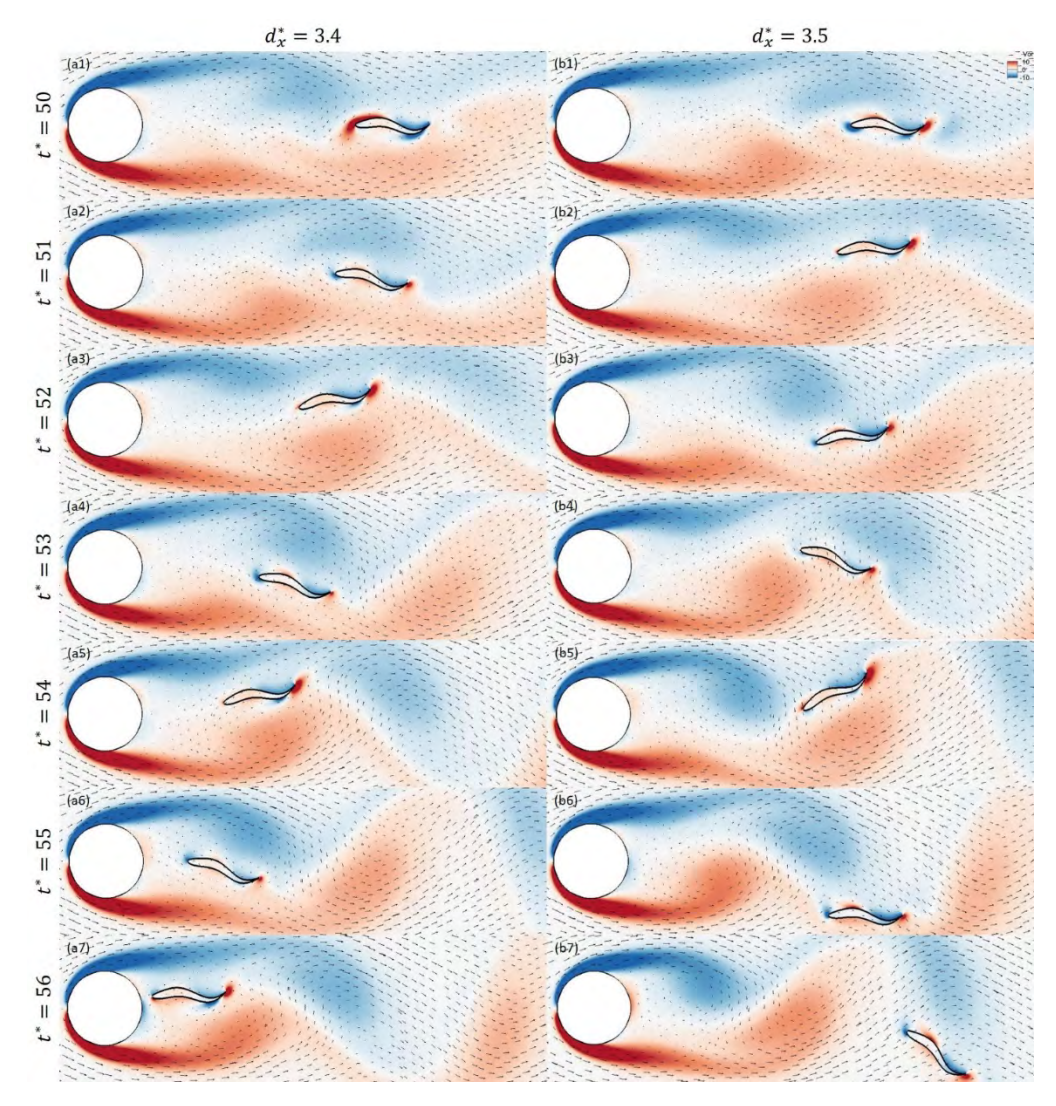


Figure 5-7 Comparison of instantaneous velocity field overlaid on vorticity contours when the fish body swims freely from the initial position of  $d_x^* = 3.4$ ,  $d_y^* = 0$  (left) and  $d_x^* = 3.5$ ,  $d_y^* = 0$  (right) for time step of  $t^* = 50,51,52,53,54,55 \& 56$ .

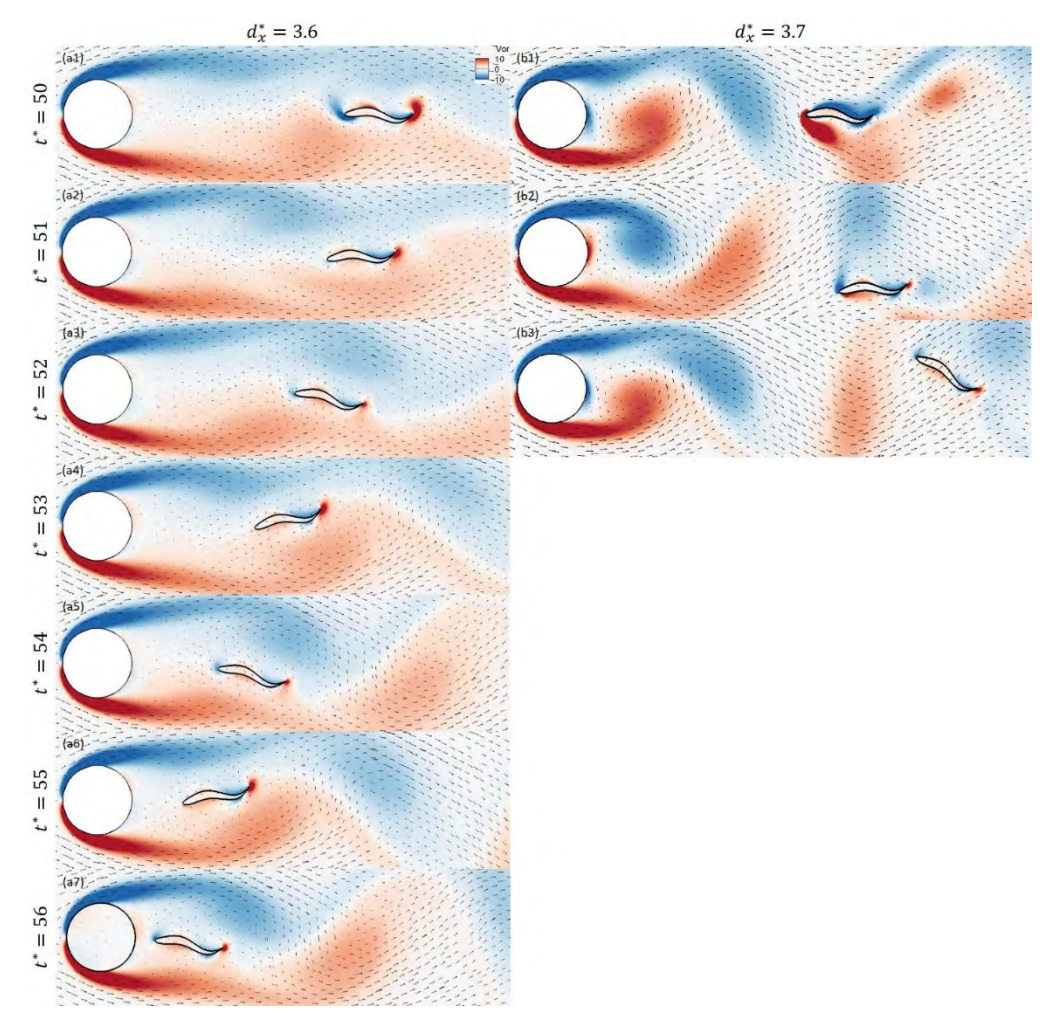


Figure 5-8 Comparison of instantaneous velocity field overlaid on vorticity contours when the fish body swims freely from the initial position of  $d_x^* = 3.6$ ,  $d_y^* = 0$  for time step of  $t^* = 50, 51, 52, 53, 54, 55 & 56$  (left) and  $d_x^* = 3.7$ ,  $d_y^* = 0$  for  $t^* = 50, 51 & 52$  (right).

## 5.3. Remarks

This chapter covers the study on self-propelled swimming behind a single cylinder. Two controlling parameters, i.e. initial streamwise and crossflow distances, are varied to investigate their effect on swimming performance. Free swimming is then actualized to present a more realistic study on fish swimming. The results are summarised as follows:

- For swimming in streamwise direction only, the fish swims towards the cylinder with initial streamwise distance of d<sub>x</sub>\* ≤ 3.4 and away from the cylinder for any distance longer than that. It is observed that the fish rotates stably within a range of angle when it swims towards the cylinder. The fish is drifted away from the cylinder as the strong vortex shedding causes the fish overturned.
- 2. The fish only swims towards the cylinder when it is initially positioned close to the cylinder in the crossflow direction (i.e.  $d_y^* = 0 \& 0.1$ ) because it is not affected by shear layer shed from the cylinder. When the fish is initially positioned away from the cylinder in the crossflow direction, the angle of rotation increases with time.
- 3. For free swimming, results vary between different initial streamwise. In cases of swimming towards the cylinder (i.e.  $d_x^* \le 3.4 \& d_x^* = 3.6$ ), fish movement in the crossflow direction is maintained minimal within a small range. In another case (i.e.  $dx^* = 3.5$ ), the fish initially swims towards but then away from the cylinder with its crossflow movement increasing with time. For remaining cases, the fish is drifted away from the cylinder with its crossflow movement increasing with time.

# **Chapter 6** Swimming behind Two Cylinders

The knowledge acquired from previous studies on fish swimming behind a single cylinder forms a solid foundation to our further investigation on free swimming behind multiple cylinders. In this chapter, we investigate the effect of different cylinder arrangement on the performance of fish swimming. Section 6.1 covers the study on free swimming behind two tandem cylinders. In Section 6.2, free swimming behind two side-by-side cylinders.

# **6.1.** Swimming behind Two Tandem Cylinders

The first cylinder arrangement to be studied is the tandem arrangement of two cylinders. With reference to Figure 2-3(b), two cylinders are placed in series upstream of the fish model and separated by the streamwise distance between centres of two cylinders  $(D_x^*)$ . The fish model is initially positioned with the "nose" at the chosen position from the centre of the downstream cylinder (i.e.  $d_x^* \& d_y^*$ ). The fish body undulates as prescribed by equation (2.1) and is allowed to swim freely in both streamwise and crossflow directions.  $Re_{fish}$ ,  $U_\infty^*$  and  $D^*$  are maintained as 40, 2.5 and 1 respectively, owing to the computational complexity. Based on knowledge gained from studies on crossflow distance,  $d_y^* = 0$  is employed as the initial lateral position for the fish. The focus of this section would be the relationship between initial streamwise distance  $(d_x^*)$  and streamwise distance between two cylinders  $(D_x^*)$  on the fish swimming. For ease of discussion, all relevant parameters with adopted values are listed in Table 6.1.

Table 6.1 Definitions and chosen values of relevant parameters in Chapter 6.1

Parameter	Definition	Valuesa
Cylinder diameter	$D^* = D/L$	1
Streamwise distance	$d_x^* = d_x/L$	2.4 to 3.6
Crossflow distance	$d_y^* = d_y/L$	0
Streamwise distance between cylinders	$D_{x}^{*}=D_{x}/L$	1 to 1.5
Reynolds number	$Re_{fish} = V_{max}L/v$	40
(fish undulatory velocity)		
Reynolds number	$Re_{\infty} = U_{\infty}L/\nu$	127.3
(free-stream flow)		
Time	$t^* = t/T_P = tU_{ref}/L$	-
Free-stream velocity	$U_{\infty}^* = U_{\infty}/U_{ref}$	2.5

<sup>&</sup>lt;sup>a</sup> The symbol '-' indicates that the parameters change according to different cases or are updated during the simulation.

Figure 6-1 is the phase diagram showing the distribution of two motion modes in the  $d_x^* - D_x^*$  plane. The motion mode describes the displacement of the fish during its swimming. The fish would either drift upstream towards (DU mode) or downstream away from (DD mode) the cylinders. It is observed that the region of DU mode is separated from that of DD mode as shown by the red dashed line in Figure 6-1. In between the regions of DU and DD modes, there are two transition regions in which the simulation outcome is not as expected (i.e. result of DU mode obtained in the region of DD mode).

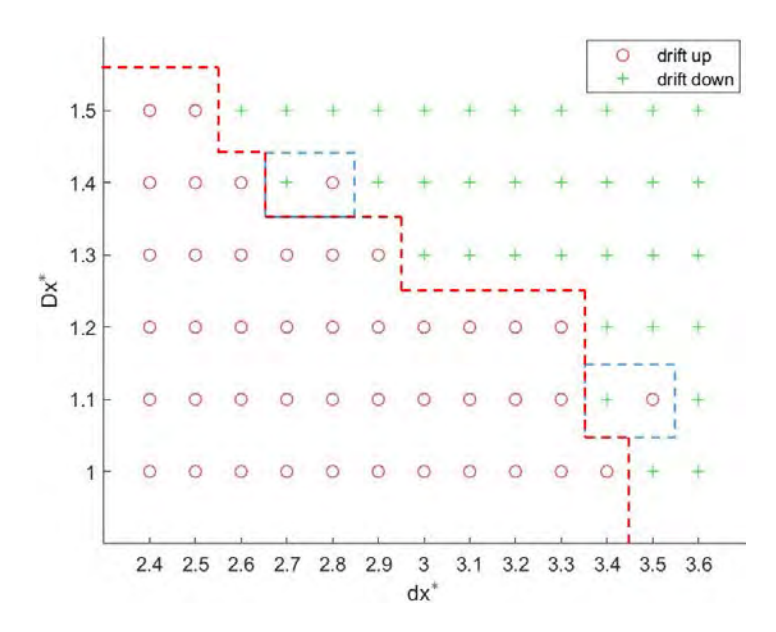


Figure 6-1 Phase diagram for the two motion modes in the  $d_x^* - D_x^*$  plane. Symbols  $\circ$ , + represent drifting upstream (DU) and drifting downstream (DD) modes respectively. The red dashed line separates the region of DU and DD modes. The blue dashed line defines the transition regions between the boundary of DU and DD modes.

To find out the difference between two motion modes, the comparison on streamwise and crossflow trajectories together with angle of rotation about the centroid are conducted. The comparison between  $d_x^* = 2.9 \& 3$  with the same  $D_x^* = 1.3$  is taken as an example. The case of  $d_x^* = 2.9$ ,  $D_x^* = 1.3$  represents DU mode while the case of  $d_x^* = 3$ ,  $D_x^* = 1.3$  represents DD mode. As shown in Figure 6-2, the fish under DD mode drifts away from its initial position dramatically. It also swims laterally away from the centreline joining two cylinders sharply with the angle of rotation showing an increasing trend. In contrast, the fish under DU mode swims towards the cylinders progressively. Its lateral displacement is kept within  $|d_y^*| = 0.1$  the whole time with the angle of rotation maintained within  $\pm 20^\circ$ . Vorticity contours are applied to reveal the physics behind the difference of fluid flow structure around the cylinders and the fish between two cases.

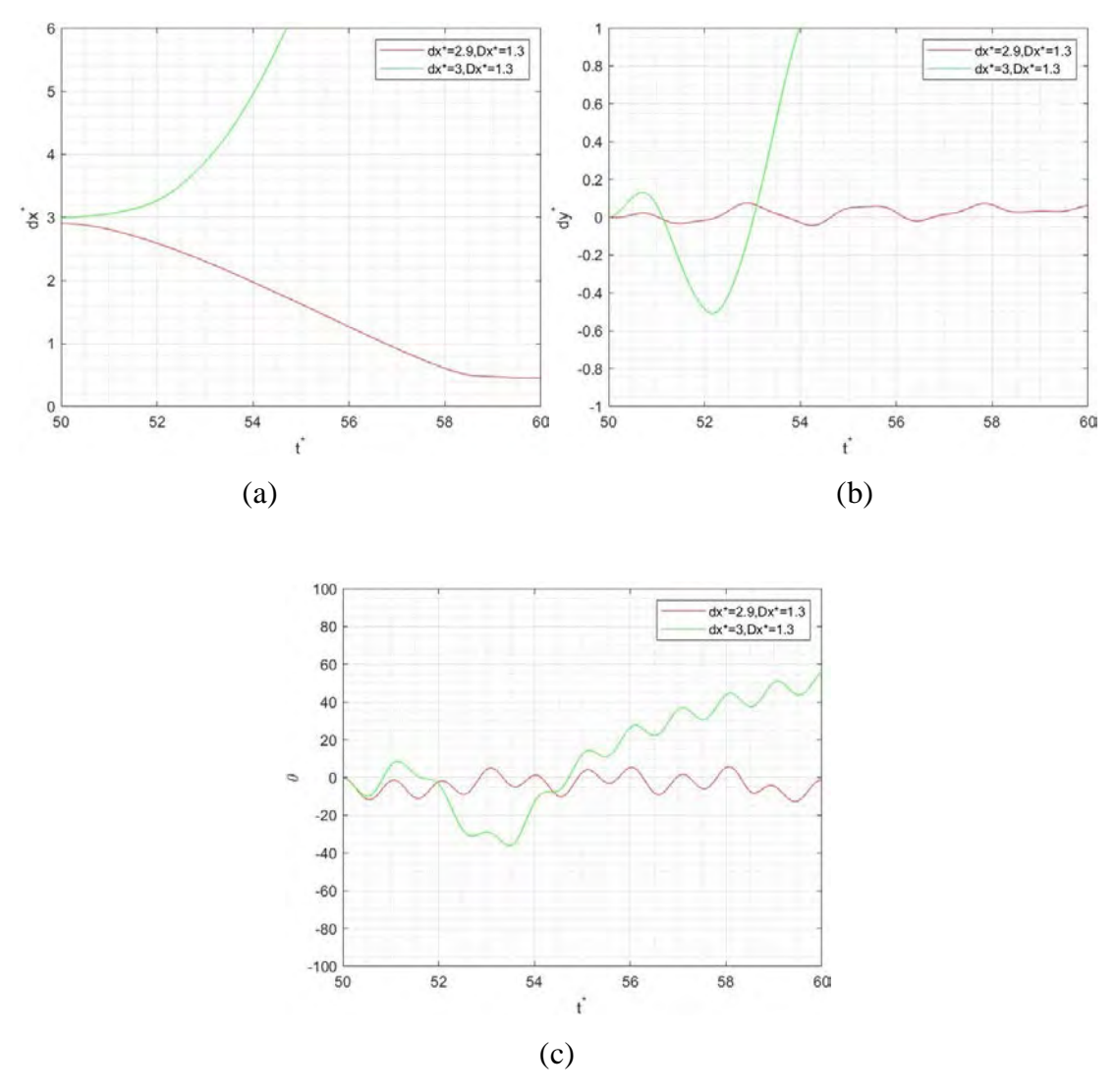


Figure 6-2 Comparison of (a) streamwise trajectories, (b) crossflow trajectories and (c) angles of rotation about centroid  $\theta$  of the fish between initial streamwise positions  $d_x^* = 2.9 \& 3$  with the same streamwise distance between two tandem cylinders  $D_x^* = 1.3$ .

In Figure 6-3(b1-b5), we could clearly see that vortex shedding happens between the tandem cylinders and the fish for  $d_x^* = 3$ ,  $D_x^* = 1.3$ . The vortical flow pushes the fish aside laterally from the centreline joining the tandem cylinders. Once the fish is pushed to the shear layer shed from the tandem cylinders, the fish is subject to the strong vortical flow as depicted in Figure 6-3(b3). The fluid flow expels the fish downstream and further away from the centreline [see Figure 6-3(b5)].

On the other hand, vortex shedding is not observed for  $d_x^* = 2.9$ ,  $D_x^* = 1.3$ . The velocity of fluid flow downstream of the tandem cylinders is minimal which forms an elongated suction zone for the fish. The fish keeps aligned with the centreline of the tandem cylinders most of the time [see Figure 6-3(a1-a7)]. It swims inside this elongated suction zone without any influence from the shear layer shed from the cylinders. In other words, a beneficial environment is created for the fish to self-propel towards the cylinders.

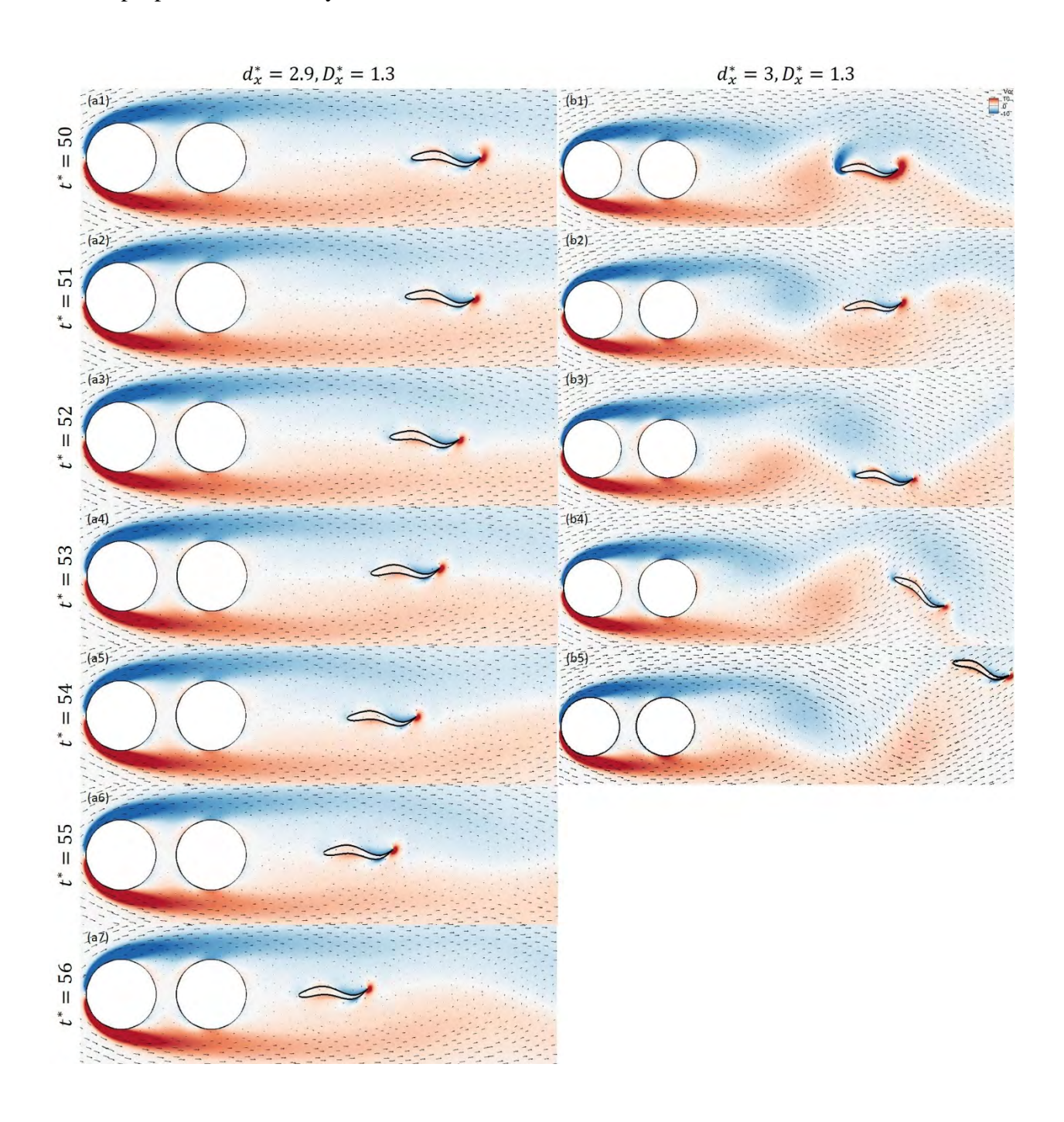


Figure 6-3 Comparison of instantaneous velocity field overlaid on vorticity contours when the fish body swims freely from the initial streamwise position of  $d_x^* = 2.9$  for time step of  $t^* = 50$  to 56 (left) and  $d_x^* = 3$  for  $t^* = 50$  to 54 (right) with the same streamwise distance between two tandem cylinders  $D_x^* = 1.3$ .

Two transition regions along the boundary of DU and DD modes also attract our attention. Both transition regions share similar features as observed in Figure 6-4 and 6-6. For DU mode in the transition region (i.e.  $d_x^* = 2.8$ ,  $D_x^* = 1.4$  and  $d_x^* = 3.5$ ,  $D_x^* = 1.1$ ), the fish swims towards the cylinders steadily. The lateral displacement always maintains within  $|d_y^*| = 0.1$  with the rotation in the range of  $-20^\circ$  to  $20^\circ$ . For DD mode in the transition region (i.e.  $d_x^* = 2.7$ ,  $D_x^* = 1.4$  and  $d_x^* = 3.4$ ,  $D_x^* = 1.1$ ), the fish drifts away from its initial position drastically. It also moves aside from the centreline joining two cylinders in a short time interval with a larger angle of rotation than DU mode.

For DU mode in the transition region (i.e.  $d_x^* = 2.8$ ,  $D_x^* = 1.4$  and  $d_x^* = 3.5$ ,  $D_x^* = 1.1$ ), we could not observe any obvious vortex shedding between the tandem cylinders and the fish. The fluid flow in the region between the downstream cylinder and the fish is calm such that the flow velocity is minimal [see Figure 6-5(b1-b5) and 6-7(b1-b9)]. This forms a suction zone in which the fish swims towards the tandem cylinders without experiencing much drag.

For DD mode in the transition region (i.e.  $d_x^* = 2.7$ ,  $D_x^* = 1.4$  and  $d_x^* = 3.4$ ,  $D_x^* = 1.1$ ), significant vortex shedding occurs between the tandem cylinders and the fish. The strong vortical flow pushes the fish laterally towards either lower or upper shear layer shed from the cylinders as shown in Figure 6-5(a2) and 6-7(a2-a4). When the fish reaches the shear layer, the strong flow together with the vortices shed from the tandem cylinders eject the fish downstream and further away from the centreline of the tandem cylinders [see Figure 6-5(a3-a5) and 6-7(a5-a7)]. That causes a significant rotation at the same time.

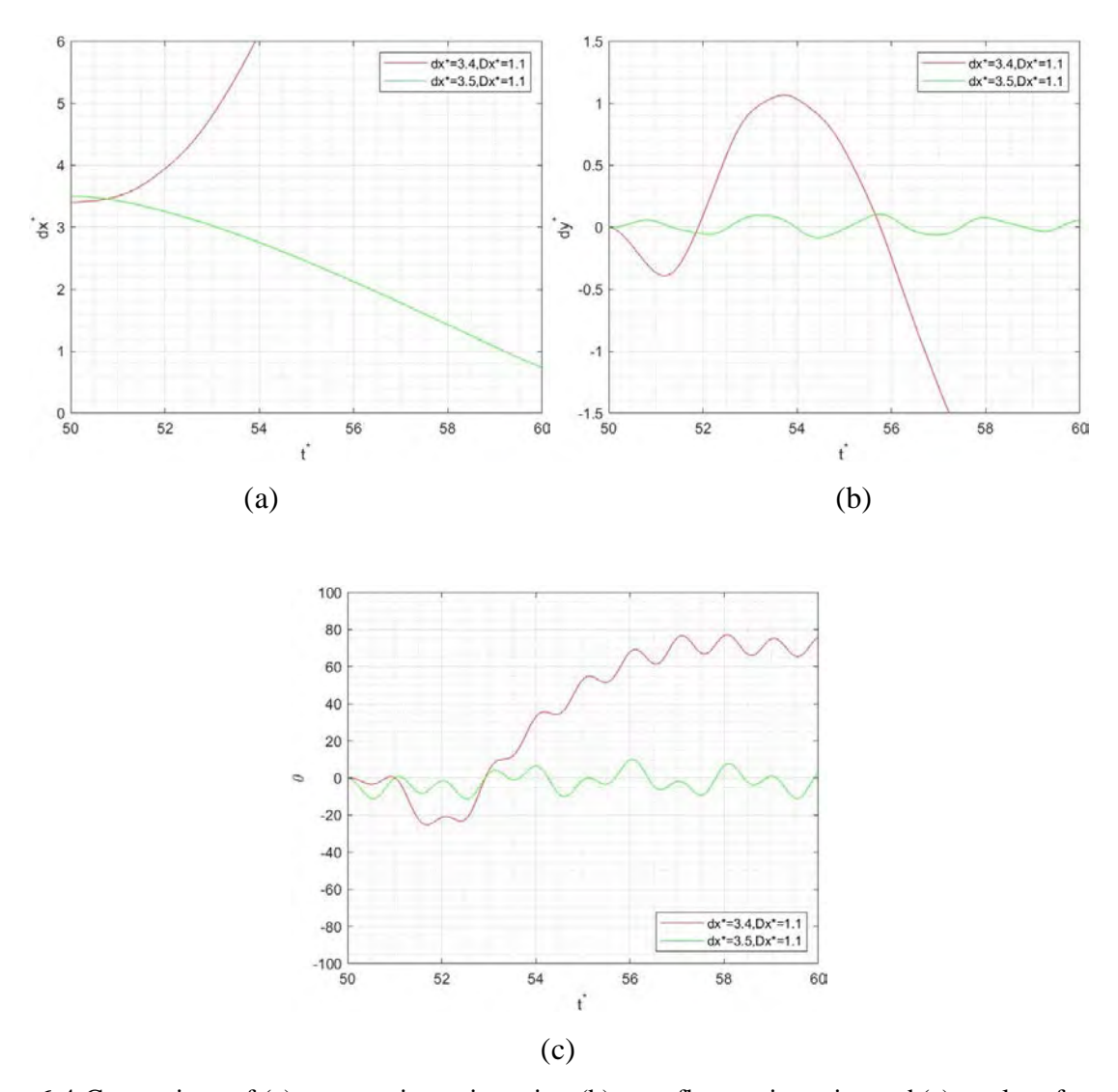


Figure 6-4 Comparison of (a) streamwise trajectories, (b) crossflow trajectories and (c) angles of rotation about centroid  $\theta$  of the fish between initial streamwise positions  $d_x^* = 3.4 \& 3.5$  with the same streamwise distance between two tandem cylinders  $D_x^* = 1.1$ . This is one of the transition regions (blue dashed line) defined in Figure 6-1.

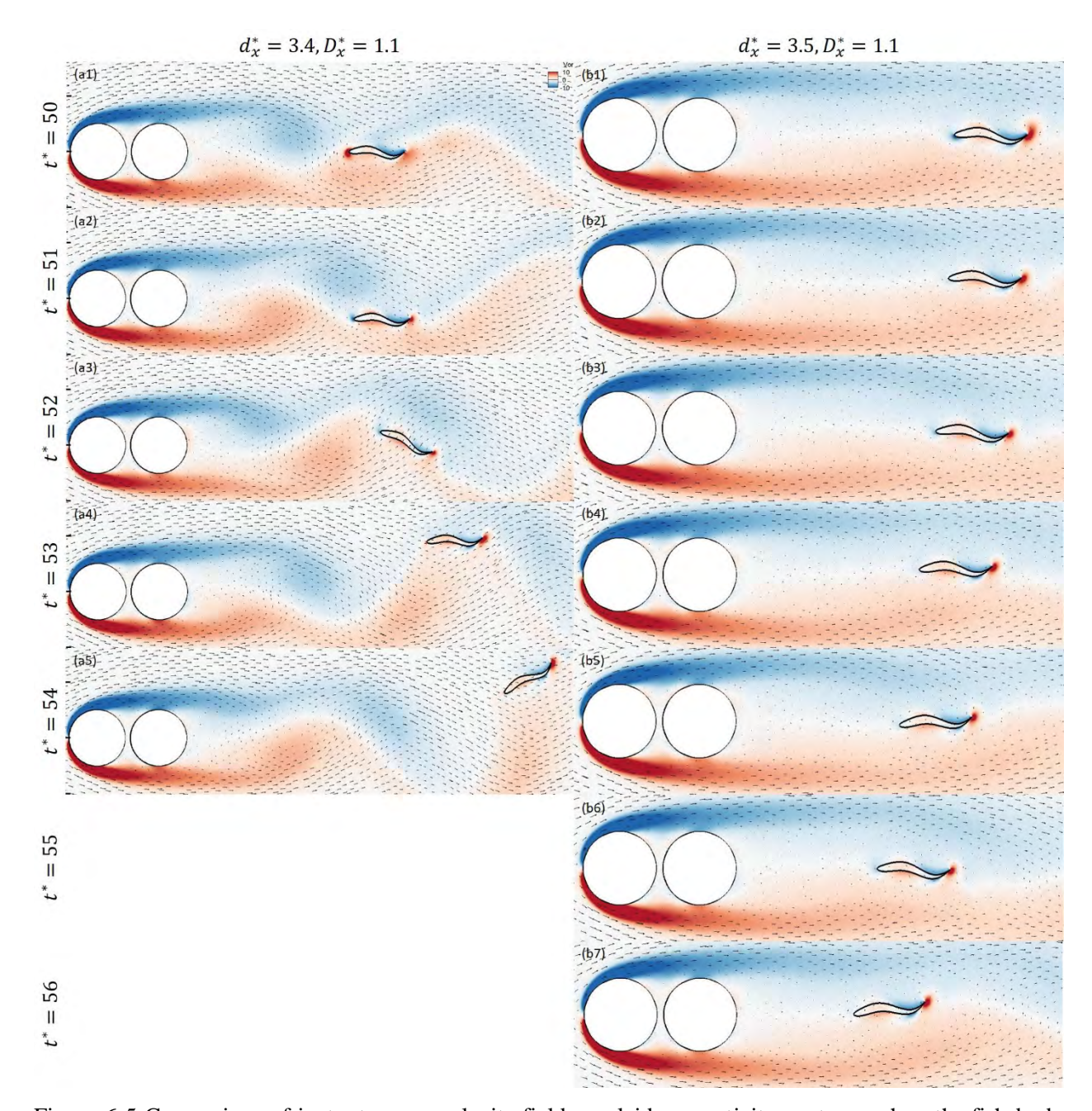


Figure 6-5 Comparison of instantaneous velocity field overlaid on vorticity contours when the fish body swims freely from the initial streamwise position of  $d_x^* = 3.4$  for time step of  $t^* = 50$  to 54 (left) and  $d_x^* = 3.5$  for  $t^* = 50$  to 56 (right) with the same streamwise distance between two tandem cylinders  $D_x^* = 1.1$ . This is one of the transition regions (blue dashed line) defined in Figure 6-1.

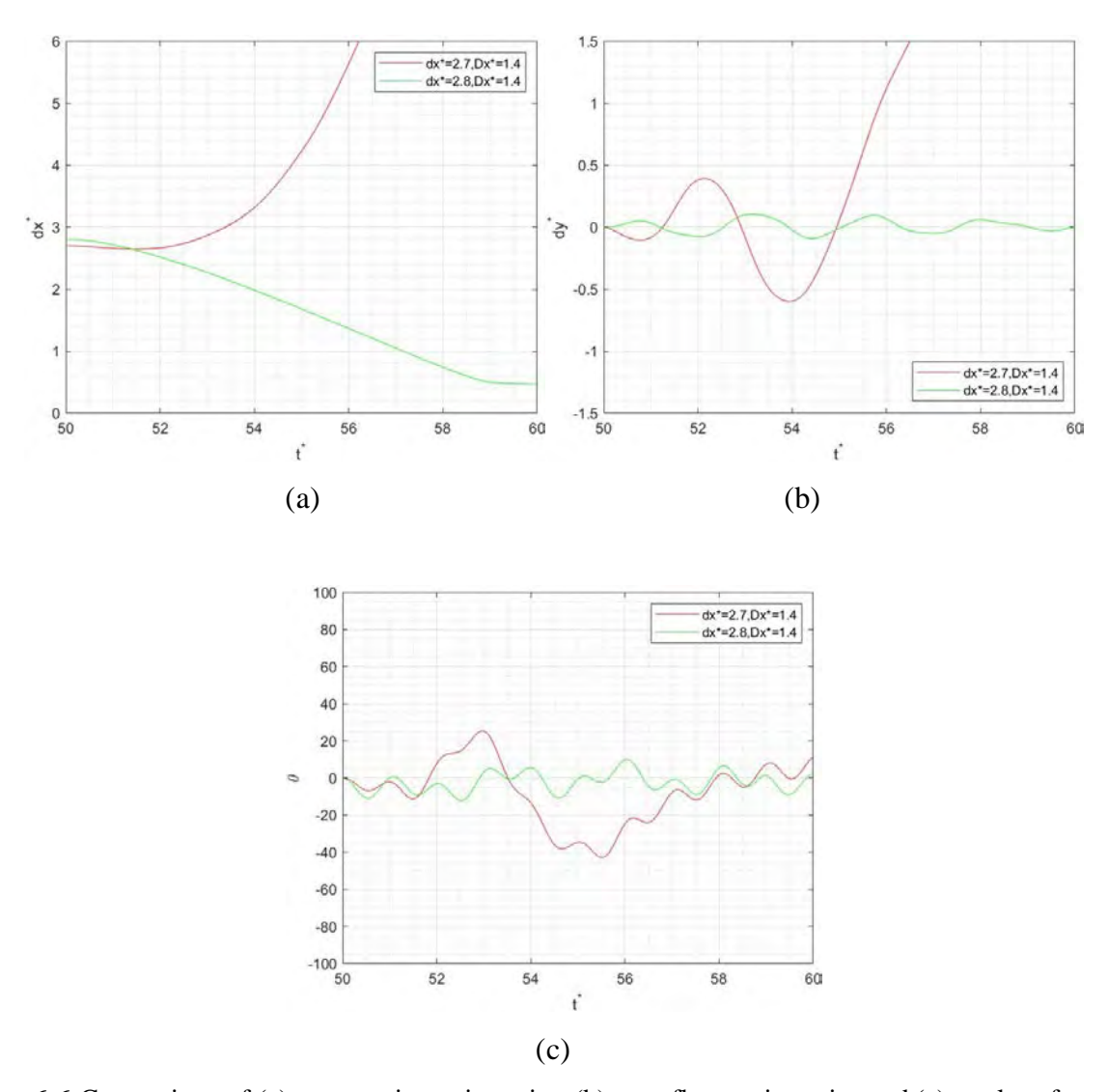


Figure 6-6 Comparison of (a) streamwise trajectories, (b) crossflow trajectories and (c) angles of rotation about centroid  $\theta$  of the fish between initial streamwise positions  $d_x^* = 2.7 \& 2.8$  with the same streamwise distance between two tandem cylinders  $D_x^* = 1.4$ . This is one of the transition regions (blue dashed line) defined in Figure 6-1.

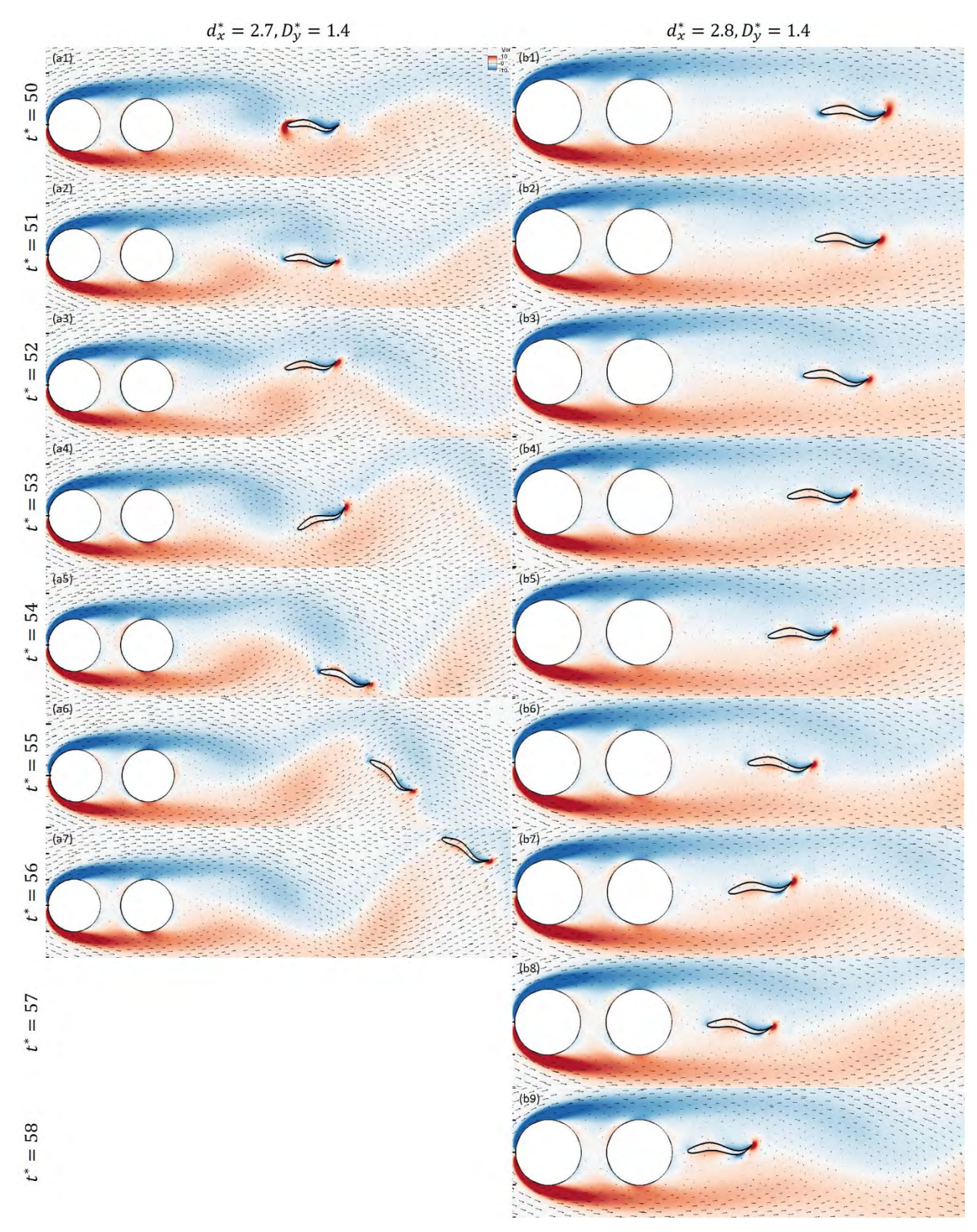


Figure 6-7 Comparison of instantaneous velocity field overlaid on vorticity contours when the fish body swims freely from the initial streamwise position of  $d_x^* = 2.7$  for time step of  $t^* = 50$  to 56 (left) and  $d_x^* = 1.5$ 

2.8 for  $t^* = 50$  to 58 (right) with the same streamwise distance between two tandem cylinders  $D_x^* = 1.4$ . This is one of the transition regions (blue dashed line) defined in Figure 6-1.

To summarize, two motion modes, DD mode and DU mode, are discovered when we study the relationship between initial  $d_x^*$  and  $D_y^*$ . A boundary is observed in the distribution of two modes with two transition regions existed. For DD mode, significant vortex shedding is observed between the tandem cylinders and the fish. The fish is pushed downstream and aside laterally by both the shear layer and vortices shed from the cylinders. This also causes significant rotation of the fish. For DU mode, no obvious vortex shedding is shown. The fish swims towards the tandem cylinders inside the suction zone and maintains aligned with the centreline of cylinders. Its rotation is within  $\pm 20^\circ$ .

# 6.2. Swimming behind Two Side-by-Side Cylinders

Another cylinder arrangement to be studied is the side-by-side arrangement of two cylinders. With reference to Figure 2-3(c), two cylinders are placed parallel to each other in the position upstream of the fish model and separated by the crossflow distance between centres of two cylinders  $(D_y^*)$ . The fish model is initially positioned with the "nose" at the chosen position from the line joining centres of two cylinders (i.e.  $d_x^* \& d_y^*$ ). The fish body undulates as prescribed by equation (2.1) and is allowed to swim freely in both streamwise and crossflow directions.  $Re_{fish}$ ,  $U_\infty^*$ ,  $D^*$  and  $d_y^*$  are maintained as 40, 2.5, 1 and 0 respectively as previous section. The focus of the section would be the relationship between initial streamwise distance  $(d_x^*)$  and crossflow distance between two cylinders  $(D_y^*)$  on the fish swimming. For ease of discussion, all relevant parameters with adopted values are listed in Table 6.2.

Table 6.2 Definitions and chosen values of relevant parameters in Chapter 6.2

Parameter	Definition	Values <sup>a</sup>
Cylinder diameter	$D^* = D/L$	1
Streamwise distance	$d_x^* = d_x/L$	3 to 4
Crossflow distance	$d_{\mathcal{Y}}^* = d_{\mathcal{Y}}/L$	0
Crossflow distance between cylinders	$D_{\mathcal{Y}}^* = D_{\mathcal{Y}}/L$	1 to 1.3
Reynolds number	$Re_{fish} = V_{max}L/\nu$	40
(fish undulatory velocity)		
Reynolds number	$Re_{\infty} = U_{\infty}L/\nu$	127.3
(free-stream flow)		
Time	$t^* = t/T_P = tU_{ref}/L$	-
Free-stream velocity	$U_{\infty}^* = U_{\infty}/U_{ref}$	2.5

<sup>&</sup>lt;sup>a</sup> The symbol '-' indicates that the parameters change according to different cases or are updated during the simulation.

Figure 6-8 shows the phase diagram of motion modes in the  $d_x^* - D_y^*$  plane. In addition of DD and DU modes described in Section 6.1, another motion mode is discovered in this study. The fish is observed to swim upstream towards the cylinders initially and then drift away to the downstream after a certain time interval (DUD mode). The distribution of motion modes under the side-by-side arrangement does not show a significant pattern as the tandem arrangement. Three modes (i.e. DD mode, DU mode and DUD mode) are distributed randomly with respect to different combinations of  $d_x^*$  and  $D_y^*$ .

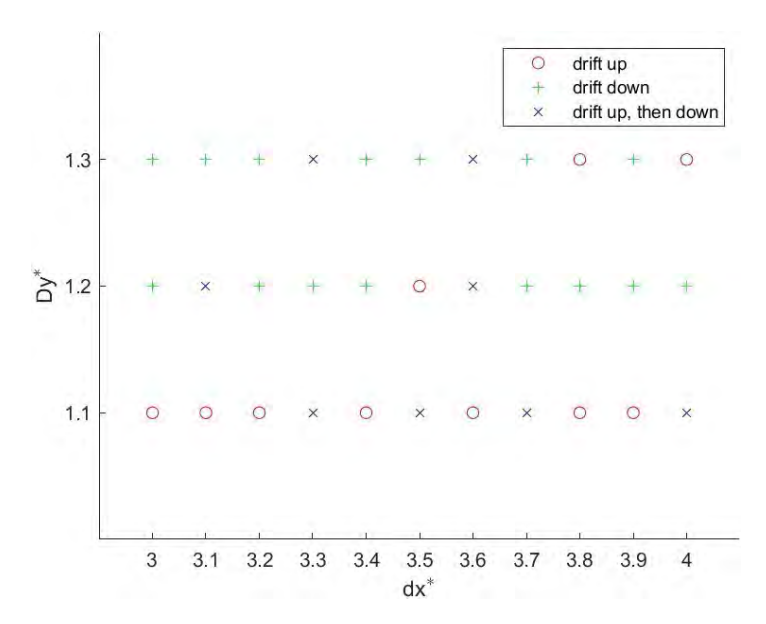


Figure 6-8 Phase diagram for the three motion modes in the  $d_x^* - D_y^*$  plane. Symbols  $\circ$ , + & × represent drifting upstream (DU), drifting downstream (DD) and drifting up then down (DUD) modes respectively.

The mechanism of DD and DU modes are basically understood in the previous section. However, it is necessary to know how  $D_y^*$  could result in the specific motion mode. To reveal the physics behind fish swimming behind two side-by-side cylinders, vorticity contours are applied. Three cases with same  $d_x^*$  but different  $D_y^*$  are chosen for comparison (i.e.  $D_y^* = 1.1, 1.2 \& 1.3$  with  $d_x^* = 3.5$ ).

For DD mode (i.e.  $d_x^* = 3.5$ ,  $D_y^* = 1.3$ ), we could see that the gap existing between two cylinders is sufficiently large for fluid to flow through and vortices shedding to form [see Figure 6-9(c1-c7)]. Though the vortices through the gap are restricted and weaker than those along the shed shear layers (i.e. across upper surface of the upper cylinder and lower surface of the lower cylinder), they are still strong enough to hinder the fish propulsion and push it downstream and aside laterally. When the fish reaches the shed shear layer as shown in Figure 6-9(c3), the strong vortical flow along the shear layer strikes the fish body to drift downstream. Depending on the direction of vortex rotation, the fish may be pushed back to the extended line from the gap, like Figure 6-9(c5). The fish would again be influenced by vortical flow from the gap and drift downstream and aside laterally as shown in Figure 6-9(c7).

For DU mode (i.e.  $d_x^* = 3.5$ ,  $D_y^* = 1.2$ ), the fluid flow through the gap is present though not as strong as that of DD mode [see Figure 6-9(b1-b8)]. Weak shear layer still exists but merely affects the fish swimming. The strong shear layers elongate from either upper or lower side of the cylinder pair and shed downstream of the fish. They induce reverse flow which propel the fish upstream as depicted in Figure 6-9(b2-b4). Although the fish is pushed aside laterally away from the gap, it remains in the suction zone and stays away from the shed shear layers. The alternating vortices shed from the upper and lower shed shear layers continue to create a beneficial environment in which the fish propels towards the cylinders [see Figure 6-9(b5-b8)].

For DUD mode (i.e.  $d_x^* = 3.5$ ,  $D_y^* = 1.1$ ), no obvious fluid flow and thus vortex shedding is observed in the gap between two side-by-side cylinders [see Figure 6-9(a1-a11)]. Shear layers are only shed from the upper and lower sides of the cylinder pair alternatively and the vorticity grows as the fish swim upstream towards the cylinders. The fish is initially pushed upstream and laterally by vortex shed behind as shown in Figure 6-9(a1-a5). Although it is pushed aside laterally, it keeps within the suction zone downstream of the side-by-side cylinders at the beginning, so it is clear from the strong shear layer either side. However, when the fish approaches close enough to either cylinder (i.e. within  $d_x^* = 1$ ) as indicated by Figure 6-9(a6), the vortex shed from the lower side of the cylinder pair expels the fish towards the shear layer shed from the upper side of cylinder pair. The strong shear layer causes the fish to rotate to be perpendicular to the direction of free flow (i.e.  $\theta = 90$ ) [see Figure 6-9(a7)]. As the anterior part of the fish is impacted by the flow along the upper shear layer, it further rotates vigorously about its centroid as shown in Figure 6-9(a8). The aggressive rotation causes the fish to overturn finally as we can see in Figure 6-9(a9). Once the fish is overturned, it is easily drifted downstream by both the shed shear layer and vortical flow with rotation continued [see Figure 6-9(a10) and (a11)].

In summary, three motion modes are discovered in the study of fish swimming behind side-by-side cylinders. For DD mode, the fish is hindered from propelling towards the cylinders by shear layers shedding from the gap between cylinders and either side of the cylinder pair. For DU mode, weak shear layers from the gap do not quite affect the fish while strong vortex shedding along either side of the cylinder pair creates reverse flow to propel the fish towards the cylinders. For DUD mode, the fish initially swims upstream because of vortex shed behind. However, it is

expelled to the shed shear layer when it approaches the cylinders. The strong flow along the shear layer and vortical flow overturn the fish and drift it downstream.

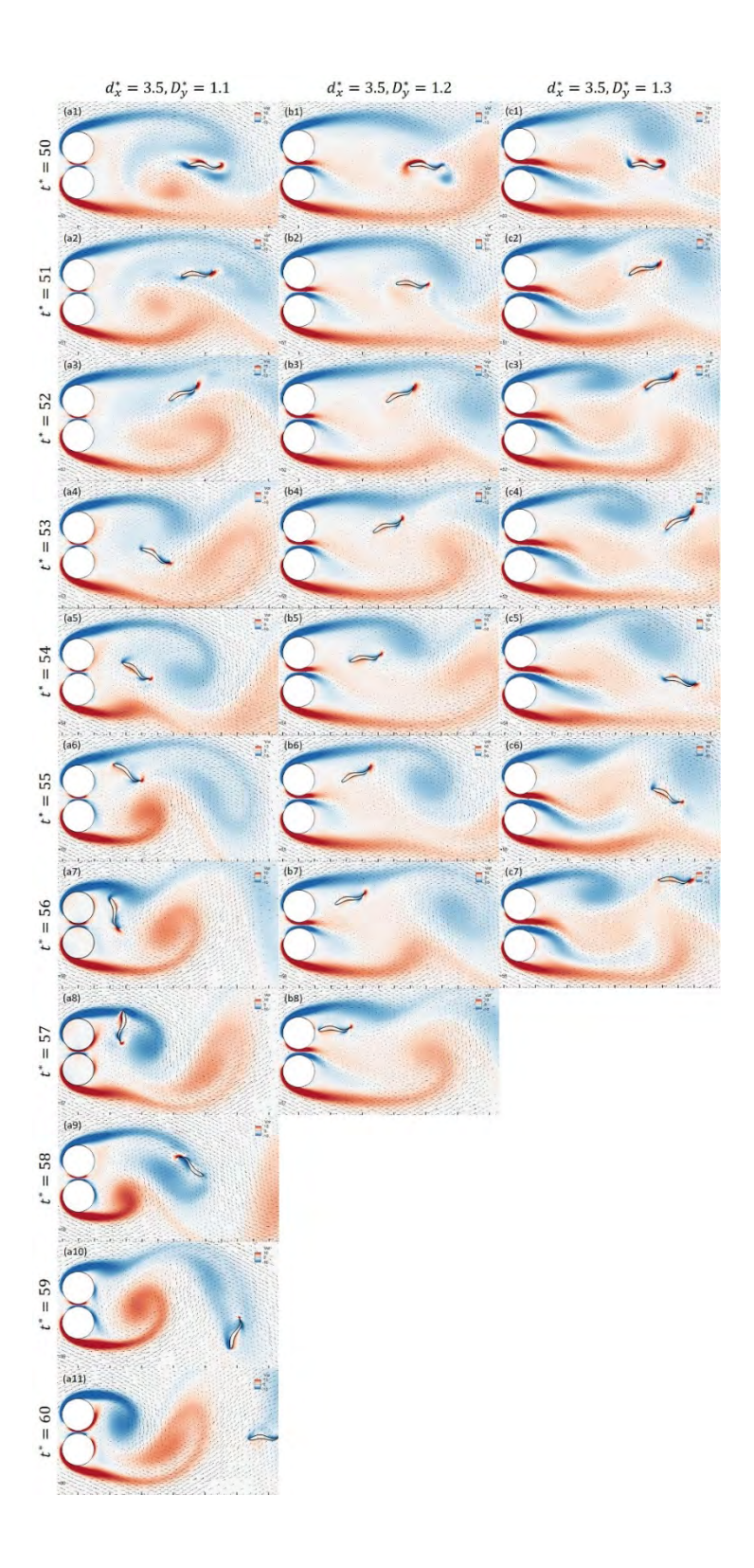


Figure 6-9 Comparison of instantaneous velocity field overlaid on vorticity contours when the fish body swims freely from the initial streamwise position of  $d_x^* = 3.5$  for time step of  $t^* = 50$  to 60 with crossflow distance between two side-by-side cylinders  $D_y^* = 1.1$  (left), for  $t^* = 50$  to 57 with  $D_y^* = 1.2$  (centre) and for  $t^* = 50$  to 56 with  $D_y^* = 1.3$  (right) respectively.

## 6.3. Remarks

In this chapter, free swimming behind two cylinders is studied. Two cylinder arrangements are investigated with the results concluded as follows:

- Two motion modes, DD mode and DU mode, are discovered in the study of free swimming behind two tandem cylinders. A boundary is observed in the distribution of two modes with two transition regions existed. In DD mode, the fish is drifted away from the cylinders by shear layer shed from the cylinders. In DU mode, the fish maintains aligned with the cylinders and therefore swims towards them.
- 2. In the study of free swimming behind two side-by-side cylinders, no significant distribution pattern of motion modes is shown. In addition to two modes mentioned previously, DUD mode is discovered. In DUD mode, the fish initially swims upstream because of vortex shed behind. However, it is expelled to the shear layer when it approaches the cylinders. The strong flow along the shed shear layer and the vortical flow overturn the fish and drift it downstream.

# **Chapter 7 Conclusions and Future Work**

## 7.1. Conclusions

This research examines the performance of fish swimming behind both single and multiple cylinders. The study is carried out in stages by releasing restriction on motion of the fish progressively. The in-house numerical solver based on the LBM coupled with IBM is applied to simulate the swimming of the fish body model. By utilizing the solver, the effects of free-stream velocity, streamwise distance, crossflow distance and cylinder diameter on fish swimming performance under different motion modes of the fish are explored. Moreover, investigation on multiple cylinders under tandem and side-by-side arrangements are analysed. The findings of this research are summarised as follows:

### (1) Constrained Swimming behind a Single Cylinder

For undulation without translational and rotational motion, effects of several key parameters, including free-stream velocity, streamwise and crossflow distances and upstream cylinder diameter are examined. Drag on the fish body decreases while lateral force increases with free-stream velocity. Power of consumption and extraction of the fish generally decreases with free-stream velocity. Furthermore, several common features regarding flow structure are discovered among different free-stream velocities at the moments of the smallest and largest drag and the largest lateral force. A complex spectrum consisted of beating, vortex shedding and undulating frequencies with the relevant harmonics are observed in the spectral analysis of drag and lateral force on the fish.

The study on streamwise distance reveals that thrust is generated on the fish body with insignificant vortex shedding when the fish is close to the cylinder in streamwise direction. In contrast, drag is discovered with significant vortex shedding in between for longer streamwise distance. In comparison with fish swimming without the presence of the cylinder, drag decreases only when the fish is positioned closely to the cylinder in the crossflow direction. When the fish has a longer crossflow distance from the cylinder, it undulates independently without any interaction with the vortex shed from the cylinder. The study on cylinder diameter shows that reverse flow occurs and

pushes the fish towards the cylinder when the size of the cylinder increases. This creates both thrust and large lateral force on the fish.

For undulation with only rotational motion, effects of streamwise and crossflow distances are investigated. Thrust is generated when the fish is close to the cylinder while drag is experienced for a position further downstream from the cylinder. Large drag is experienced by the fish when the rotation angle exceeds the specific range. Moreover, obvious vortex shedding behind the cylinder is shown when drag is experienced by the fish. During the investigation on crossflow distance, overturning of the fish body is observed for several cases because of strong shed shear layer and vortical flow acted on the fish head causing excessive rotation about the fish centroid. On the other hand, a stable rotation is observed when the fish centroid is either aligned with the centre of the cylinder or the shed shear layer.

### (2) Self-Propelled Swimming behind a Single Cylinder

For swimming in streamwise direction only, the fish swims towards the cylinder for with initial streamwise distance less than the specific value (i.e.  $d_x^* = 3.4$ ) and away from the cylinder for any distance longer. It is observed that the fish maintains a stable rotation within a range when it swims towards the cylinder. The fish is drifted away from the cylinder because the strong vortex shedding causes the fish overturned. When the fish is aligned with the cylinder in the crossflow direction, it is less likely affected by shear layer shed from the cylinder and swims towards the cylinder. For the fish positioned further away from the cylinder in the crossflow direction, the angle of rotation increases with time.

For free swimming, diversified results are observed over a range of initial streamwise distances. In some cases, the fish swims towards the cylinder with the small movement maintained in the crossflow direction. In another case, the fish initially swims towards but then away from the cylinder while its crossflow movement increases with time. For remaining cases, the fish is drifted away from the cylinder with the lateral movement increasing with time.

#### (3) Free Swimming behind Two Cylinders

The study on fish swimming behind a single cylinder constitutes a solid fundamental basis for the subsequent study on free swimming behind two cylinders. Two different cylinder arrangements are considered. Two motion modes, DD mode and DU mode, are discovered in the study of free swimming behind two tandem cylinders. A boundary is observed in the distribution of two modes with two transition regions existed. In DD mode, the fish swims away from the centreline of cylinders in the crossflow direction and is pushed downstream by the shear layer shed from the cylinders. In DU mode, the fish maintains aligned with the centres of the cylinders with small rotation observed. The fish therefore swims towards the tandem cylinders.

In the study of free swimming behind two side-by-side cylinders, significant distribution pattern of motion modes is not identified. Besides two modes mentioned, another motion mode, DUD mode, is discovered. In DUD mode, the fish initially swims upstream but then expelled to the shear layer when it approaches the cylinders. Strong flow along the shed shear layer and vortical flow together cause the fish to overturn and drift it downstream.

## 7.2. Future Work

This study sheds light on fish swimming behind obstacles despite of the existence of limitation. It addresses the research gaps identified in Chapter 1 overall. The findings could provide some inspiration for further study in the future. The following aspects could be potential areas in which future work could be conducted.

(1) Effects of free-stream velocity and Reynolds number with other controlling parameters on fish swimming performance

In the present study on controlling parameters, other than Reynolds number (i.e. streamwise and crossflow distances), it is noticed that their effects on the fish swimming performance would also depend on free-stream velocity. As Reynolds number is directly proportional to free-stream velocity, this implies that effects of other controlling parameters also depend on Reynolds number. The combined effects of free-stream velocity, hence Reynolds number, and other controlling parameters should not be neglected. This should be included in the future research work to provide a full picture of effects of different controlling parameters.

(2) Enhancement of computational capability to handle realistic Reynolds numbers

The present study focuses on a relatively low Reynolds number (i.e.  $Re_{\infty} = 127$  for  $U_{\infty}^* = 2.5$ ) due to the complexity involved in free swimming of the fish model. A numerical solver with the ability to handle higher Reynolds number is required to simulate the complex swimming motion in the realistic aquatic environment.

### (3) Involvement of smaller cylinders

The study mainly focuses on larger cylinders (i.e.  $D^* \ge 1$ ) with only one case of smaller cylinder (i.e.  $D^* = 0.5$ ). It is necessary to conduct study on smaller cylinders to further reveal the effect of cylinder diameter.

### (4) Involvement of other fish models and swimming modes

The study utilizes NACA0012 airfoil and BCF mode as the fish model and swimming mode respectively. This could merely resemble the anguilliform swimming. As swimmers differ from each other in terms of body shape and propelling mechanism, the results of this study could not represent the swimming performance for all species. Developing geometrical models and description of propelling motion for other swimmers is therefore paramount to broaden the research spectrum.

#### (5) Effect of free-stream velocity on free swimming behind two cylinders

The present study only covers the effect of initial streamwise distance between cylinders and the fish  $(d_x^*)$ , streamwise distance between two cylinders  $(D_x^*)$  and crossflow distance between two cylinders  $(D_y^*)$  on the distribution of motion modes. Similar to fish swimming behind a single cylinder, it is believed that free-stream velocity also plays an important role on the motion mode. Further study could be carried out on the effect of free-stream velocity.

### (6) Effect of fish undulating frequency

The fish undulating frequency is defined as  $f = U_{ref}/L$ , where  $U_{ref}$  is refere velocity and L is the fish body length. As both  $U_{ref}$  and L are chosen to be the reference quantities, they are assigned to be fixed values. Therefore, the effect of fish undulating frequency has not been investigated. However, it is believed that the fish undulating frequency plays a significant role in

the swimming performance. Further study could be conducted to give more details on the effect of fish undulating frequency.

### (7) Involvement of other cylinder arrangements

In the study of fish swimming behind multiple cylinders, only tandem and side-by-side arrangements are explored. Other arrangements, such as cylinders in array and diamond pattern could be included to investigate their effect on fish swimming.

## (8) Involvement of fish schooling

Fish schooling is an interesting and realistic phenomenon in actual aquatic environment. Its effect on enhancing swimming performance attracts attention of many researchers.

## (9) Application of machine learning to fish propelling motion

In the study, the fish swimming motion is prescribed as per the equation. Therefore, the fish is lack of its intelligence in real life when it experiences an environment detrimental to its swimming performance. Machine learning could contribute by training the fish model to be more intelligent and realistic.

# References

- [1] A. Meek, *The Migrations of Fish*. Edward Arnold, 1916.
- [2] M. C. Lucas and E. Baras, Migration of freshwater fishes. Oxford; Blackwell Science, 2001.
- [3] R. M. McDowall, "The evolution of diadromy in fishes (revisited) and its place in phylogenetic analysis," *Reviews in fish biology and fisheries*, vol. 7, no. 4, pp. 443–462, 1997, doi: 10.1023/A:1018404331601
- [4] R. Feurich, J. Boubée, and N. R. B. Olsen, "Spoiler Baffles in Circular Culverts," *Journal of environmental engineering (New York, N.Y.)*, vol. 137, no. 9, pp. 854–857, 2011, doi: 10.1061/(ASCE)EE.1943-7870.0000384
- [5] K. D. Fausch, "Profitable stream positions for salmonids: Relating specific growth rate to net energy gain," *Canadian Journal of Zoology*, vol. 62, no. 3, pp. 441–451, Mar. 1984. doi:10.1139/z84-067
- [6] W. E. Probst, C. F. Rabeni, W. G. Covington, and R. E. Marteney, "Resource Use by Stream-Dwelling Rock Bass and Smallmouth Bass," *Transactions of the American Fisheries Society* (1900), vol. 113, no. 3, pp. 283–294, 1984, doi: 10.1577/1548-8659(1984)113<283:RUBSRB>2.0.CO;2
- [7] E. T. Rankin, "Habitat Selection by Smallmouth Bass in Response to Physical Characteristics in a Natural Stream," *Transactions of the American Fisheries Society (1900)*, vol. 115, no. 2, pp. 322–334, 1986, doi: 10.1577/1548-8659(1986)115<322:HSBSBI>2.0.CO;2
- [8] D. E. Facey and G. D. Grossman, "The Metabolic Cost of Maintaining Position for Four North American Stream Fishes: Effects of Season and Velocity," *Physiological zoology*, vol. 63, no. 4, pp. 757–776, 1990, doi: 10.1086/physzool.63.4.30158175
- [9] C. L. Gerstner, "Use of substratum ripples for flow refuging by Atlantic cod, Gadus morhua," Environmental biology of fishes, vol. 51, no. 4, pp. 455–460, 1998, doi: 10.1023/A:1007449630601
- [10] J. S. Diana, *Biology and Ecology of Fishes*. Carmel, Ind: Biological Sciences Press, a Division of Cooper Pub. Group, 1995.
- [11] R. L. McLaughlin and D. L. Noakes, "Going against the flow: an examination of the propulsive movements made by young brook trout in streams," *Canadian journal of fisheries and aquatic sciences*, vol. 55, no. 4, pp. 853–860, 1998, doi: 10.1139/f97-308
- [12] J. Heggenes, "Flexible Summer Habitat Selection by Wild, Allopatric Brown Trout in Lotic Environments," *Transactions of the American Fisheries Society* (1900), vol. 131, no. 2, pp. 287–298, 2002, doi: 10.1577/1548-8659(2002)131<0287:FSHSBW>2.0.CO;2

- [13] J. C. Liao, D. N. Beal, G. V. Lauder, and M. S. Triantafyllou, "Fish Exploiting Vortices Decrease Muscle Activity," *Science (American Association for the Advancement of Science)*, vol. 302, no. 5650, pp. 1566–1569, 2003, doi: 10.1126/science.1088295
- [14] J. C. Liao, D. N. Beal, G. V. Lauder, and M. S. Triantafyllou, "The Kármán gait: Novel body kinematics of rainbow trout swimming in a vortex street," *Journal of experimental biology*, vol. 206, no. 6, pp. 1059–1073, 2003, doi: 10.1242/jeb.00209
- [15] M. Daghooghi and I. Borazjani, "The hydrodynamic advantages of synchronized swimming in a rectangular pattern," *Bioinspiration & biomimetics*, vol. 10, no. 5, pp. 056018–056018, 2015, doi: 10.1088/1748-3190/10/5/056018
- [16] W. Wu, R. Gu, Z. Hu, and Y. Sun, "Study on the Karman gait kinematics of an airfoil in an asymmetrical vortex street," *Physics of fluids* (1994), vol. 36, no. 9, 2024, doi: 10.1063/5.0228852
- [17] M. Taguchi and J. C. Liao, "Rainbow trout consume less oxygen in turbulence: The energetics of swimming behaviors at different speeds," *Journal of experimental biology*, vol. 214, no. 9, pp. 1428–1436, 2011, doi: 10.1242/jeb.052027
- [18] W. Wang, H. Huang, and X. Y. Lu, "Self-propelled plate in wakes behind tandem cylinders," *Physical review. E*, vol. 100, no. 3, pp. 033114–033114, 2019, doi: 10.1103/PhysRevE.100.033114
- [19] N. Thekkethil, M. Shrivastava, A. Agrawal, and A. Sharma, "Effect of wavelength of fish-like undulation of a hydrofoil in a free-stream flow," *Sadhana* (*Bangalore*), vol. 42, no. 4, pp. 585–595, 2017, doi: 10.1007/s12046-017-0619-7
- [20] N. Thekkethil, A. Sharma, and A. Agrawal, "Unified hydrodynamics study for various types of fishes-like undulating rigid hydrofoil in a free stream flow," *Physics of fluids* (1994), vol. 30, no. 7, 2018, doi: 10.1063/1.5041358
- [21] C. M. Breder Jr, "The locomotion of fishes," Zool. Sci. Contrib. N. Y. Zool. Soc., vol. 4, no. 5, pp. 159–297, 1926.
- [22] M. J. Lighthill, "Note on the swimming of slender fish," *Journal of fluid mechanics*, vol. 9, no. 2, pp. 305–317, 1960, doi: 10.1017/S0022112060001110
- [23] M. J. Lighthill, "Hydromechanics of Aquatic Animal Propulsion," *Annual review of fluid mechanics*, vol. 1, no. 1, pp. 413–446, 1969, doi: 10.1146/annurev.fl.01.010169.002213
- [24] M. J. Lighthill, "Aquatic animal propulsion of high hydromechanical efficiency," *Journal of fluid mechanics*, vol. 44, no. 2, pp. 265–301, 1970, doi: 10.1017/S0022112070001830
- [25] T. Y.-T. Wu, "Hydromechanics of swimming propulsion. Part 1. Swimming of a two-dimensional flexible plate at variable forward speeds in an inviscid fluid," *Journal of fluid mechanics*, vol. 46, no. 2, pp. 337–355, 1971, doi: 10.1017/S0022112071000570

- [26] T. Y.-T. Wu, "Hydromechanics of swimming propulsion. Part 2. Some optimum shape problems," *Journal of fluid mechanics*, vol. 46, no. 3, pp. 521–544, 1971, doi: 10.1017/S0022112071000685
- [27] T. Y.-T. Wu, "Hydromechanics of swimming propulsion. Part 3. Swimming and optimum movements of slender fish with side fins," *Journal of fluid mechanics*, vol. 46, no. 3, pp. 545–568, 1971, doi: 10.1017/S0022112071000697
- [28] C. C. Lindsey, "Form, function, and locomotory habits in fish," in *Fish Physiology*, Elsevier, 1978, pp. 1–100, doi: 10.1016/S1546-5098(08)60163-6
- [29] P. W. Webb and D. Weihs, Fish Biomechanics. Praeger, 1983.
- [30] P. W. Webb, "Form and Function in Fish Swimming," Scientific American, Inc, vol. 251, no. 1, pp. 58–68, 1984, doi: 10.1038/scientificamerican0784-72
- [31] A. D. McClellan, "Control of Locomotion in a Lower Vertebrate, the Lamprey: Brainstem Command Systems and Spinal Cord Regeneration," *American zoologist*, vol. 29, no. 1, pp. 37–51, 1989, doi: 10.1093/icb/29.1.37
- [32] M. Sfakiotakis, D. M. Lane, and J. B. C. Davies, "Review of fish swimming modes for aquatic locomotion," *IEEE journal of oceanic engineering*, vol. 24, no. 2, pp. 237–252, 1999, doi: 10.1109/48.757275
- [33] H. Liu, R. J. Wassersug, and K. Kawachi, "A computational fluid dynamics study of tadpole swimming," *Journal of experimental biology*, vol. 199, no. 6, pp. 1245–1260, 1996, doi: 10.1242/jeb.199.6.1245
- [34] H. Liu, R. Wassersug, and K. Kawachi, "The three-dimensional hydrodynamics of tadpole locomotion," *Journal of experimental biology*, vol. 200, no. 22, pp. 2807–2819, 1997, doi: 10.1242/jeb.200.22.2807
- [35] J. Carling, T. L. Williams, and G. Bowtell, "Self-propelled anguilliform swimming: Simultaneous solution of the two-dimensional Navier-Stokes equations and Newton's laws of motion," *Journal of experimental biology*, vol. 201, no. 23, pp. 3143–3166, 1998, doi: 10.1242/jeb.201.23.3143
- [36] U. K. Müller, J. Smit, E. J. Stamhuis, and J. J. Videler, "How the body contributes to the wake in undulatory fish swimming: Flow fields of a swimming eel (Anguilla anguilla)," *Journal of experimental biology*, vol. 204, no. 16, pp. 2751–2762, 2001.
- [37] E. D. Tytell and G. V. Lauder, "The hydrodynamics of eel swimming: I. Wake structure," *Journal of experimental biology*, vol. 207, no. 11, pp. 1825–1841, 2004, doi: 10.1242/jeb.00968
- [38] D. Weihs, "Hydromechanics of Fish Schooling," *Nature (London)*, vol. 241, no. 5387, pp. 290–291, 1973, doi: 10.1038/241290a0

- [39] G.-J. Dong and X.-Y. Lu, "Characteristics of flow over traveling wavy foils in a side-by-side arrangement," *Physics of fluids* (1994), vol. 19, no. 5, pp. 057107-057107-11, 2007, doi: 10.1063/1.2736083
- [40] B. M. Boschitsch, P. A. Dewey, and A. J. Smits, "Propulsive performance of unsteady tandem hydrofoils in an in-line configuration," *Physics of fluids* (1994), vol. 26, no. 5, 2014, doi: 10.1063/1.4872308
- [41] M. Daghooghi and I. Borazjani, "The hydrodynamic advantages of synchronized swimming in a rectangular pattern," *Bioinspiration & biomimetics*, vol. 10, no. 5, pp. 056018–056018, 2015, doi: 10.1088/1748-3190/10/5/056018
- J. Heggenes, "Effects of Short-Term Flow Fluctuations on Displacement of, and Habitat Use by, Brown Trout in a Small Stream," *Transactions of the American Fisheries Society (1900)*, vol. 117, no. 4, pp. 336–344, 1988, doi: 10.1577/1548-8659(1988)117<0336:EOSFFO>2.3.CO;2
- [43] K. D. Fausch, "Experimental Analysis of Microhabitat Selection by Juvenile Steelhead (Oncorhynchus mykiss) and Coho Salmon (O. kisutch) in a British Columbia Stream," *Can. J. Fish. Aquat. Sci.*, vol. 50, no. 6, pp. 1198–1207, 1993, doi: 10.1139/f93-136
- [44] P. W. Webb, "The effect of solid and porous channel walls on steady swimming of steelhead trout Oncorhynchus mykiss," *Journal of experimental biology*, vol. 178, no. 1, pp. 97–108, 1993, doi: 10.1242/jeb.178.1.97
- [45] C. L. Gerstner and P. W. Webb, "The station-holding performance of the plaice Pleuronectes platessa on artificial substratum ripples," *Canadian Journal of Zoology*, vol. 76, no. 2, pp. 260–268, 1998, doi: 10.1139/z97-192
- [46] P. Webb, "Entrainment by river chub nocomis micropogon and smallmouth bass micropterus dolomieu on cylinders," *Journal of experimental biology*, vol. 201 (Pt 16), no. 16, pp. 2403–2412, 1998, doi: 10.1242/jeb.201.16.2403
- [47] A. M. Sutterlin and S. Waddy, "Possible role of the posterior lateral line in obstacle entrainment by brook trout (Salvelinus fontinalis)," *J. Fish. Res. Board Can.*, vol. 32, no. 12, pp. 2441–2446, 1975, doi: 10.1139/f75-2
- [48] J. C. Liao, D. N. Beal, G. V. Lauder, and M. S. Triantafyllou, "The Kármán gait: novel body kinematics of rainbow trout swimming in a vortex street," *Journal of experimental biology*, vol. 206, no. Pt 6, pp. 1059–1073, 2003, doi: 10.1242/jeb.00209
- [49] J. C. Liao, D. N. Beal, G. V. Lauder, and M. S. Triantafyllou, "Fish Exploiting Vortices Decrease Muscle Activity," *Science (American Association for the Advancement of Science)*, vol. 302, no. 5650, pp. 1566–1569, 2003, doi: 10.1126/science.1088295 [1]

- [50] D. N. Beal, F. S. Hover, M. S. Triantafyllou, J. C. Liao, and G. V. Lauder, "Passive propulsion in vortex wakes," *Journal of fluid mechanics*, vol. 549, no. 1, pp. 385–402, 2006, doi: 10.1017/S0022112005007925
- [51] O. Akanyeti and J. C. Liao, "The effect of flow speed and body size on Kármán gait kinematics in rainbow trout," *Journal of experimental biology*, vol. 216, no. Pt 18, pp. 3442–3449, 2013, doi: 10.1242/jeb.087502
- [52] H.-T. Yuan and W.-R. Hu, "A numerical study of tadpole swimming in the wake of a D-section cylinder," *J. Hydrodynam. B*, vol. 29, no. 6, pp. 1044–1053, 2017, doi: 10.1016/S1001-6058(16)60818-1
- [53] E. D. Tytell, "Do trout swim better than eels? Challenges for estimating performance based on the wake of self-propelled bodies," *Experiments in fluids*, vol. 43, no. 5, pp. 701–712, 2007, doi: 10.1007/s00348-007-0343-x
- [54] J. O. Dabiri, "On the estimation of swimming and flying forces from wake measurements," *Journal of experimental biology*, vol. 208, no. Pt 18, pp. 3519–3532, 2005, doi: 10.1242/jeb.01813
- [55] S. Kern and P. Koumoutsakos, "Simulations of optimized anguilliform swimming," *Journal of experimental biology*, vol. 209, no. Pt 24, pp. 4841–4857, 2006, doi: 10.1242/jeb.02526
- [56] M. Wolfgang, J. Anderson, M. Grosenbaugh, D. Yue, and M. Triantafyllou, "Near-body flow dynamics in swimming fish," *Journal of experimental biology*, vol. 202 (Pt 17), no. 17, pp. 2303–2327, 1999, doi: 10.1242/jeb.202.17.2303
- [57] I. Borazjani and F. Sotiropoulos, "Numerical investigation of the hydrodynamics of carangiform swimming in the transitional and inertial flow regimes," *Journal of experimental biology*, vol. 211, no. 10, pp. 1541–1558, 2008, doi: 10.1242/jeb.015644
- [58] I. Borazjani and F. Sotiropoulos, "Numerical investigation of the hydrodynamics of anguilliform swimming in the transitional and inertial flow regimes," *Journal of experimental biology*, vol. 212, no. 4, pp. 576–592, 2009, doi: 10.1242/jeb.025007
- [59] C. Wei, Q. Hu, Y. Liu, S. Yin, Z. Chen, and X. Ji, "Performance evaluation and optimization for two-dimensional fish-like propulsion," *Ocean engineering*, vol. 233, pp. 109191-, 2021, doi: 10.1016/j.oceaneng.2021.109191
- [60] Z. Xiong, H. Xia, and T. Han, "Effects of fish body thickness on hydrodynamic performance for self-propulsion carangiform swimmer," *Physics of fluids* (1994), vol. 36, no. 8, 2024, doi: 10.1063/5.0222510
- [61] J. D. Eldredge and D. Pisani, "Passive locomotion of a simple articulated fish-like system in the wake of an obstacle," *Journal of fluid mechanics*, vol. 607, pp. 279–288, 2008, doi: 10.1017/S0022112008002218

- [62] X. Shao, D. Pan, J. Deng, and Z. Yu, "Hydrodynamic performance of a fishlike undulating foil in the wake of a cylinder," *Physics of fluids* (1994), vol. 22, no. 11, 2010, doi: 10.1063/1.3504651
- [63] F.-B. Tian, H. Luo, L. Zhu, and X.-Y. Lu, "Interaction between a flexible filament and a downstream rigid body," *Physical review. E, Statistical, nonlinear, and soft matter physics*, vol. 82, no. 2 Pt 2, pp. 026301–026301, 2010, doi: 10.1103/PhysRevE.82.026301
- [64] S. G. Park, B. Kim, and H. J. Sung, "Self-propelled flexible fin in the wake of a circular cylinder," *Physics of fluids* (1994), vol. 28, no. 11, 2016, doi: 10.1063/1.4966981
- [65] C. Li, W. Yang, X. Xu, J. Wang, M. Wang, and L. Xu, "Numerical investigation of fish exploiting vortices based on the Kármán gaiting model," *Ocean engineering*, vol. 140, pp. 7–18, 2017, doi: 10.1016/j.oceaneng.2017.05.011
- [66] Y. Tong, J. Xia, and L. Chen, "Study on energy extraction of Kármán gait hydrofoils from passing vortices," *Physics of fluids* (1994), vol. 33, no. 12, 2021, doi: 10.1063/5.0070862
- [67] G. Xu and Y. Zhou, "Strouhal numbers in the wake of two inline cylinders," *Experiments in fluids*, vol. 37, no. 2, pp. 248–256, 2004, doi: 10.1007/s00348-004-0808-0
- [68] D. Sumner, "Two circular cylinders in cross-flow: A review," *Journal of fluids and structures*, vol. 26, no. 6, pp. 849–899, 2010, doi: 10.1016/j.jfluidstructs.2010.07.001
- [69] W. J. Stewart, F. B. Tian, O. Akanyeti, C. J. Walker, and J. C. Liao, "Refuging rainbow trout selectively exploit flows behind tandem cylinders," *Journal of experimental biology*, vol. 219, no. 14, pp. 2182–2191, 2016, doi: 10.1242/jeb.140475
- [70] K. Ren, J. Yu, H. Li, and H. Feng, "Numerical investigation on the swimming mode and stable spacing with two self-propelled fish arranged in tandem," *Ocean engineering*, vol. 259, pp. 111861-, 2022, doi: 10.1016/j.oceaneng.2022.111861
- [71] S. Gong, L. Kang, D. Fan, W. Cui, and X. Lu, "Hydrodynamic interactions between two self-propelled flapping plates swimming towards each other," *Acta mechanica Sinica*, vol. 41, no. 3, 2025, doi: 10.1007/s10409-024-23664-x
- [72] R. R. Nourgaliev, T. N. Dinh, T. G. Theofanous, and D. Joseph, "The lattice Boltzmann equation method: theoretical interpretation, numerics and implications," *International journal of multiphase flow*, vol. 29, no. 1, pp. 117–169, 2003, doi: 10.1016/S0301-9322(02)00108-8
- [73] B. Dünweg, A. J. C. Ladd, C. Holm, K. Kremer, C. Holm, and K. Kremer, "Lattice Boltzmann Simulations of Soft Matter Systems," in *Advanced Computer Simulation Approaches for Soft Matter Sciences III*, Germany: Springer Berlin / Heidelberg, 2009, pp. 89–166. doi: 10.1007/978-3-540-87706-6 2
- [74] P. Lallemand and L. Luo, "Theory of the lattice boltzmann method: dispersion, dissipation, isotropy, galilean invariance, and stability," *Physical review. E, Statistical physics, plasmas, fluids, and*

- related interdisciplinary topics, vol. 61, no. 6 Pt A, pp. 6546–6562, 2000, doi: 10.1103/physreve.61.6546
- [75] Q. K. Qinjun Kang, P. C. L. Peter C. Lichtner, and D. R. J. David R. Janecky, "Lattice Boltzmann Method for Reacting Flows in Porous Media," *Advances in applied mathematics and mechanics*, vol. 2, no. 5, pp. 545–563, 2010, doi: 10.4208/aamm.10-m10S02
- [76] C. S. Peskin, "Flow patterns around heart valves: A numerical method," *Journal of computational physics*, vol. 10, no. 2, pp. 252–271, 1972, doi: 10.1016/0021-9991(72)90065-4
- [77] D. Zhang, G. Pan, L. Chao, and Y. Zhang, "Effects of Reynolds number and thickness on an undulatory self-propelled foil," *Physics of fluids* (1994), vol. 30, no. 7, 2018, doi: 10.1063/1.5034439
- [78] H. Yu, X.-Y. Lu, and H. Huang, "Collective locomotion of two uncoordinated undulatory self-propelled foils," *Physics of fluids* (1994), vol. 33, no. 1, 2021, doi: 10.1063/5.0036231
- [79] H. Tang *et al.*, "Inhibited swimming capacity of fish entrained in wake vortices behind a semi-cylinder," *Ocean engineering*, vol. 293, pp. 116617-, 2024, doi: 10.1016/j.oceaneng.2023.116617
- [80] H. Wang, S. Yuan, H. Tang, C. Gualtieri, and Y. Ling, "Hydrodynamic performance of swimming fish in the wake region of a semi-cylinder," *Ocean engineering*, vol. 315, pp. 119730-, 2025, doi: 10.1016/j.oceaneng.2024.119730
- [81] D. Sparks, E. Rajeev, S. S. Koley, A. Canestrelli, and J. C. Liao, "Swimming kinematics of rainbow trout behind a 3×5 cylinder array: a computationally driven experimental approach to understanding fish locomotion," *Journal of experimental biology*, vol. 227, no. 23, 2024, doi: 10.1242/jeb.247873